Cell

Article

Co-development of mesoderm and endoderm enables organotypic vascularization in lung and gut organoids

Graphical abstract

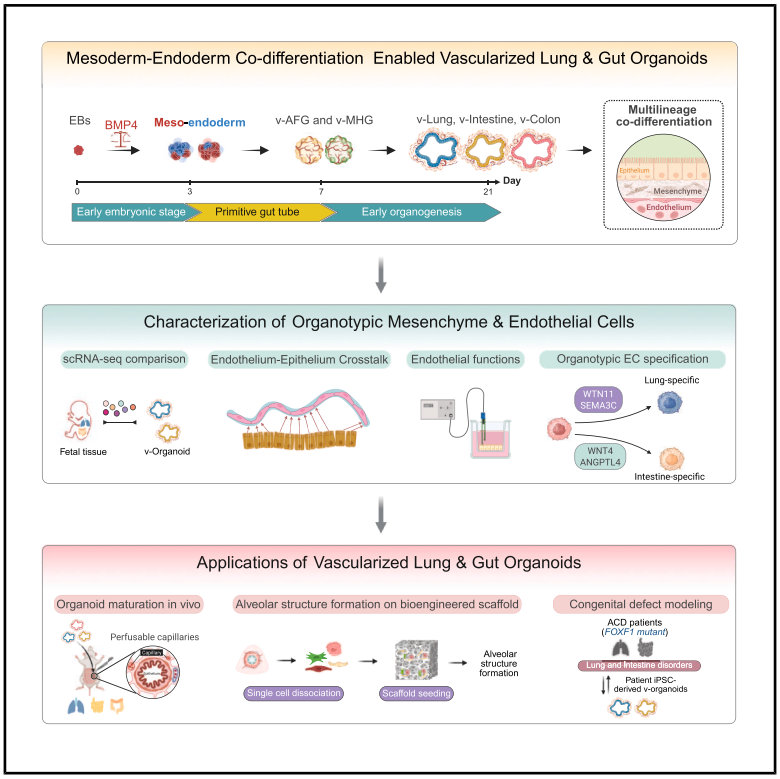

Highlights

- BMP-mediated mesoderm-endoderm co-differentiation is vital for organotypic vasculature
- Organotypic vasculature supports endoderm organoid development and maturation
- Vascularized organoids resemble human fetal lung and intestine features
- Vascularized organoids model abnormal endothelial-epithelial crosstalk in FOXF1 disease

Authors

Yifei Miao, Nicole M. Pek, Cheng Tan, ..., Ya-Wen Chen, Minzhe Guo, Mingxia Gu

Correspondence

yifei.miao@ioz.ac.cn (Y.M.), minzhe.guo@cchmc.org (M.G.), mgu@mednet.ucla.edu (M.G.)

In brief

Recapitulating the concurrent development of germ layers through the co-differentiation of mesoderm and endoderm within a single spheroid enabled the generation of vascularized lung and intestinal organoids, revealing how the microenvironment guides the development of organotypic endothelial and mesenchymal cells.

Miao et al., 2025, Cell *188*, 4295–4313
August 7, 2025
https://doi.org/10.1016/j.cell.2025.05.041

CellPress

Cell

CellPress

Article

Co-development of mesoderm and endoderm enables organotypic vascularization in lung and gut organoids

Yifei Miao,[1,2,3,17,18,19,*] Nicole M. Pek,[1,2,3,17] Cheng Tan,[1,2,3,17] Cheng Jiang,[1] Zhiyun Yu,[1,2,3] Kentaro Iwasawa,[2,3] Min Shi,[2,3,4] Daniel O. Kechele,[3] Nambirajan Sundaram,[5] Victor Pastrana-Gomez,[1,2,3] Debora I. Sinner,[1] Xingchen Liu,[6] Ko Chih Lin,[6] Cheng-Lun Na,[1] Keishi Kishimoto,[2] Min-Chi Yang,[7] Sushila Maharjan,[6] Jason Tchieu,[2,3] Jeffrey A. Whitsett,[1] Yu Shrike Zhang,[6,8,9] Kyle W. McCracken,[2,3,4] Robbert J. Rottier,[10,11] Darrell N. Kotton,[12] Michael A. Helmrath,[5] James M. Wells,[2,3,13] Takanori Takebe,[2,3,14,15] Aaron M. Zorn,[2,3] Ya-Wen Chen,[7] Minzhe Guo,[1,*] and Mingxia Gu[1,2,3,16,20,*]

[1]Division of Pulmonary Biology, Perinatal Institute, Cincinnati Children's Hospital Medical Center (CCHMC), Department of Pediatrics, University of Cincinnati College of Medicine, Cincinnati, OH 45229, USA
[2]Center for Stem Cell and Organoid Medicine (CuSTOM), CCHMC, Department of Pediatrics, University of Cincinnati, College of Medicine, Cincinnati, OH 45229, USA
[3]Division of Developmental Biology, CCHMC, Department of Pediatrics, University of Cincinnati, College of Medicine, Cincinnati, OH 45229, USA
[4]Division of Nephrology and Hypertension, CCHMC, Cincinnati, OH 45229, USA
[5]Division of Pediatric General and Thoracic Surgery, CCHMC, Cincinnati, OH 45229, USA
[6]Division of Engineering in Medicine, Department of Medicine, Brigham and Women's Hospital, Harvard Medical School, Cambridge, MA 02139, USA
[7]Department of Cell, Developmental, and Regenerative Biology, Department of Otolaryngology, Black Family Stem Cell Institute, Icahn School of Medicine at Mount Sinai, New York, NY 10029, USA
[8]Harvard Stem Cell Institute, Harvard University, Cambridge, MA 02138, USA
[9]Broad Institute of MIT and Harvard, Cambridge, MA 02142, USA
[10]Department of Cell Biology, Erasmus MC, Rotterdam, the Netherlands
[11]Department of Pediatric Surgery, Sophia Children's Hospital, Wytemaweg 80, 3015 CN Rotterdam, the Netherlands
[12]Pulmonary Center, Department of Medicine, Center for Regenerative Medicine, Boston University and Boston Medical Center, Boston, MA 02118, USA
[13]Division of Endocrinology, CCHMC, Cincinnati, OH 45229, USA
[14]Division of Gastroenterology, Hepatology & Nutrition, CCHMC, Cincinnati, OH 45229, USA
[15]Department of Genome Biology and WPI Premium Research Institute for Human Metaverse Medicine (WPI-PRIMe), Osaka University, Osaka 565-0871, Japan
[16]Department of Anesthesiology and Perioperative Medicine, David Geffen School of Medicine, Eli and Edythe Broad Center for Regenerative Medicine and Stem Cell Biology, University of California, Los Angeles (UCLA), Los Angeles, CA 90095, USA
[17]These authors contributed equally
[18]Present address: Human Organ Physiopathology Emulation System (HOPE), Institute of Zoology, Chinese Academy of Sciences, Beijing 100101, China
[19]Present address: Beijing Institute for Stem Cell and Regenerative Medicine, Beijing 100101, China
[20]Lead contact
*Correspondence: yifei.miao@ioz.ac.cn (Y.M.), minzhe.guo@cchmc.org (M.G.), mgu@mednet.ucla.edu (M.G.)
https://doi.org/10.1016/j.cell.2025.05.041

SUMMARY

The vasculature and mesenchyme exhibit distinct organ-specific characteristics adapted to local physiological needs, shaped by microenvironmental and cell-cell interactions from early development. To recapitulate this entire process, we co-differentiated mesoderm and endoderm within the same spheroid to vascularize lung and intestinal organoids from induced pluripotent stem cells (iPSCs). Bone morphogenetic protein (BMP) signaling fine-tuned the endoderm-to-mesoderm ratio, a critical step in generating appropriate proportions of endothelial and epithelial progenitors with tissue specificity. Single-cell RNA sequencing (scRNA-seq) revealed organ-specific gene signatures of endothelium and mesenchyme and identified key ligands driving endothelial specification. The endothelium exhibited tissue-specific barrier function, enhanced organoid maturation, cellular diversity, and alveolar formation on the engineered lung scaffold. Upon transplantation into mice, the organoid vasculature integrated with the host circulation while preserving organ specificity, further promoting organoid maturation. Leveraging these vascularized organoids, we

uncovered abnormal endothelial-epithelial crosstalk in patients with *forkhead box F1* (*FOXF1*) mutations. Multilineage organoids provide an advanced platform to study intricate cell-to-cell communications in human organogenesis and disease.

INTRODUCTION

The human vasculature, particularly the capillary beds, exhibits remarkable specialization across different organs to meet local physiological demands. This functional specialization is also evident at the transcriptomic level, as demonstrated by recent human fetal[1] and adult[2] cell atlases, where endothelial cells (ECs) from distinct organ systems form separate clusters, highlighting unique gene signatures. It has been indicated that the unique microenvironment within each organ plays a critical role in driving the organotypic vascular endothelium and mesenchyme.[3–6] However, the spatial and temporal dynamics of this intricate and highly interactive process during organ vascularization in human development remain poorly understood. Addressing this knowledge gap requires *in vitro* platforms that not only include relevant cell lineages but also incorporate organotypic vasculature with proper cellular architecture.

Organoids, three-dimensional (3D) tissue structures that mimic the cellular composition and function of organs, created microenvironment suitable to study human development and disease, especially the development of organotypic vasculature. Various groups have focused on assembly approaches that involve the fusion of multiple cell types following their separate differentiation.[7,8] For instance, previous studies have attempted to vascularize liver[9,10] and brain[11,12] organoids by incorporating primary ECs such as human umbilical vein ECs (HUVECs). However, this approach resulted in ECs lacking well-defined organ specificity and architecture, thereby limiting the patterning and functional maturation of the organoids. The assembly methods fail to accurately represent how vascular cells develop during organogenesis *in vivo*. In contrast, during early development, coordinated interactions between multiple germ layers-guided by morphogenetic patterning cues-are essential for the specification and differentiation of organotypic endothelial and mesenchymal cells. Recreating these complex developmental interactions is therefore critical for establishing physiologically relevant vascularization of organoids. However, vascularization of organoid derived from non-mesodermal lineages, such as the ectoderm and endoderm has been particularly challenging. This is because differentiating human induced pluripotent stem cells (iPSCs) into mesodermal versus non-mesodermal lineages requires distinct, and sometimes even opposing signaling pathways. Thus, efforts to vascularize endodermal organoids such as intestinal and lung organoids have achieved only limited success.

To address this, previous studies have attempted to generate vascularized intestinal organoids by introducing angiogenic factors such as bone morphogenetic protein 4 (BMP4), vascular endothelial growth factor A (VEGFA), fibroblast growth factor (FGF), or epiregulin (EREG) to expand a small population of endogenous endothelial progenitors, which emerge incidentally during endoderm differentiation.[13,14] While these approaches produced ECs that partially mirrored the endothelial gene profile of the human fetal small intestine (SI), the resulting vasculature was still limited in quantity, structurally and functionally immature, and often lacked organ-specific characteristics and full functionality. More importantly, existing methods for generating lung organoids[15–18] have not yet succeeded in recapitulating the human alveolar capillary interface—a structure essential for gas exchange. This limitation is expected, as most protocols for differentiating anterior foregut and lung organoids from iPSCs rely on strong inhibition of BMP and transforming growth factor β (TGF-β) signaling. While effective for endodermal patterning, these conditions are incompatible with vascular and mesenchymal lineage specification. Consequently, the absence of robust vascularization in intestinal and lung organoids substantially limits their physiological relevance for disease modeling and therapeutic applications.

In this study, we leverage developmental principles to establish an *in vitro* vascularized organoid platform that faithfully recapitulated the co-development of mesodermal and endodermal lineages. This approach enables the efficient differentiation and specification of both the endodermal derivatives and organotypic endothelial and mesenchymal populations. The resulting vascularized lung and intestinal organoids featured organotypic endothelium and mesenchyme, demonstrating enhanced cell-type diversity, 3D architecture, cell survival, and maturation.

This multilineage organoid system enables the study of aberrant cell-cell interactions diverse disease contexts. Alveolar capillary dysplasia with misalignment of pulmonary veins (ACDMPV) is a congenital lung disorder caused by mutations in *forkhead box F1* (*FOXF1*). However, conventional lung epithelial organoids lack FOXF1-expressing mesenchyme and ECs, limiting their capacity to model this condition. By differentiating patient-derived iPSCs carrying *FOXF1* mutations into vascularized lung organoids, we were able to recapitulate both the primary endothelial defects and the secondary epithelial abnormalities resulting from disrupted endothelial-epithelial crosstalk.

Collectively, the vascularized lung and intestinal organoids provide a transformative platform for studying the cell fate determination of organ-specific vasculature and the cell-cell interactions involved in both development and disease.

RESULTS

Generation of vascularized early primitive gut tube via fine-tuning mesoderm-endoderm co-differentiation

To initiate the co-development of vasculature within the gut tube organoids, we replicated early human embryonic development by simultaneously differentiating the relevant germ layer progenitors within a single 3D embryoid body (EB) (Figure 1A). We found that persistent activation of Nodal by activin A and temporal activation of Wingless and INT-1 (WNT) signal were sufficient to support definitive endoderm (DE) differentiation in our protocol[19,20] (Figures S1A–S1D). Balancing DE and mesoderm requires precise control of BMP activation; prolonged BMP4 exposure

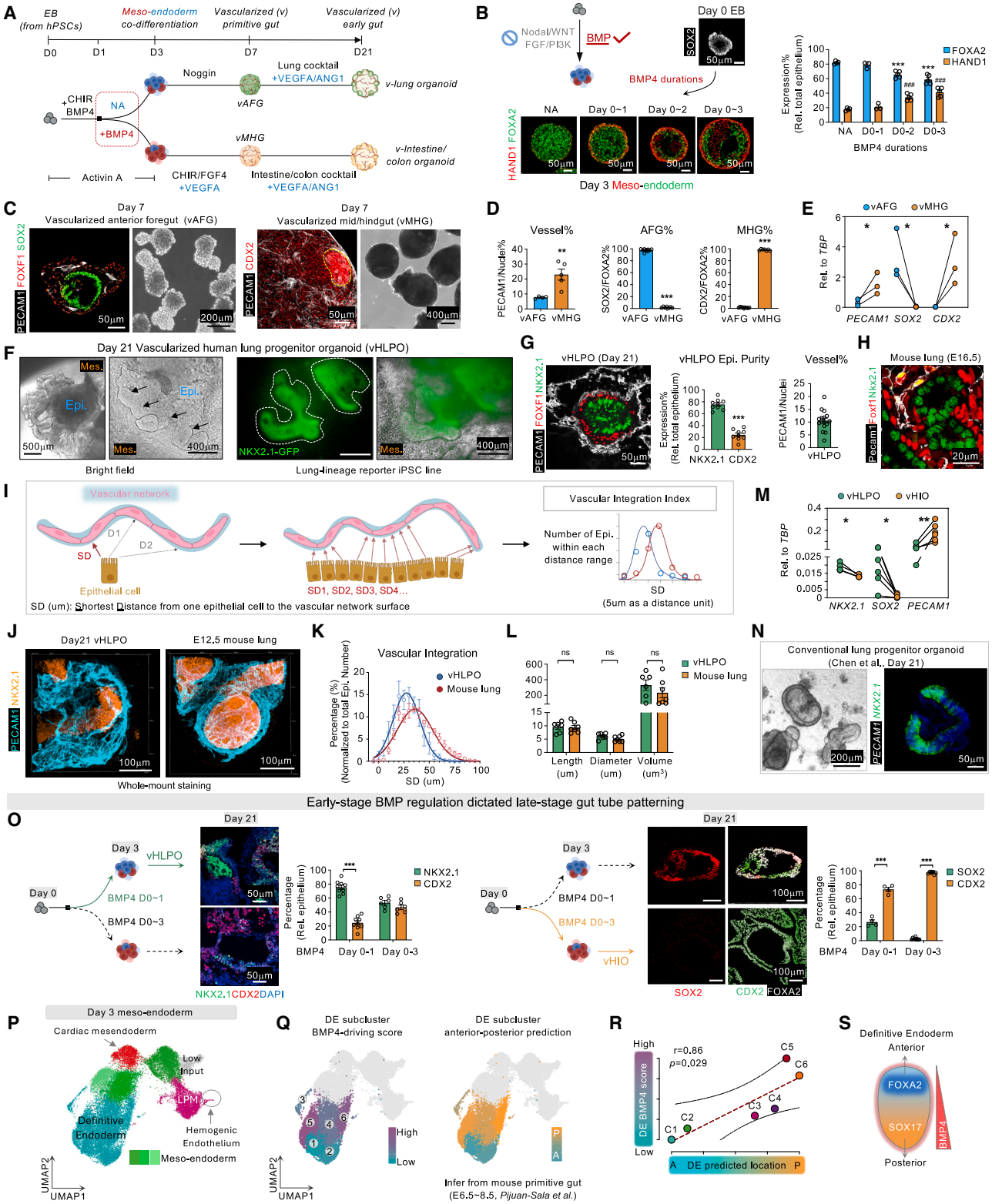

Figure 1. Refining BMP signal for endoderm mesoderm co development and vascularized organoid generation

(A) Schematic illustration of generating vascularized organoids. EB, embryoid body; hPSCs, human pluripotent stem cells; vAFG, vascularized anterior foregut; vMHG, vascularized midgut/hindgut.

(legend continued on next page)

slightly suppresses DE while promoting heart and neural crest derivatives expressed 1 (HAND1)-positive mesoderm[19] (Figures 1B and S1E–S1G). Next, to generate vascularized anterior foregut (vAFG) organoids from meso-endoderm spheroids, we examined previously reported key signaling that specifically targeted epithelial differentiation without mesoderm induction.[20] We found that other than BMP inhibition, endogenous WNT, FGF, TGF-β, and Hedgehog (HH) signaling provided by various cell types within the multilineage organoid were sufficient to drive AFG organoid differentiation from days 3 to 7 (Figures 1A, 1C–1E, and S2A–S2D). Although introducing VEGFA during the primitive gut tube phase (days 3–7) expanded the endogenous pool of ECs without affecting AFG epithelial purity and quantity (Figure S2C), this intervention led to the suppression of lung epithelial generation (NKX2-1$^+$) at a later stage (Figure S2D). Thus, endogenous angiogenic factors are sufficient to maintain vascularization in vAFG.

Collectively, endogenous morphogens in 3D multilineage spheroids significantly simplify the protocol and improve the reproducibility over previous methods.[15,17,18] This approach required only BMP inhibition for the proper patterning of AFG epithelium with vasculature and mesenchyme (Figures 1C–1E, days 3–7). Similarly, to generate vascularized midgut/hindgut (vMHG), CHIR99021 (CHIR), FGF4, and VEGFA were introduced into meso-endodermal spheroids from days 3 to 7.[21,22] This combination also led to increased vascular proportion without dampening small intestinal epithelial identities (CDX2$^+$/GATA4$^+$) (Figures 1C–1E and S2F–S2H).

Creation of vascularized lung and intestine organoids resembling *in vivo* tissues

Building on the established vAFG and vMHG, we further patterned the lung and intestine lineages from days 7 to 21. The combined application of VEGFA and angiopoietin 1 (ANG1)[23] with conventional lung organoid progenitor cocktail[15–18] synergistically augmented endothelial differentiation during the organogenesis phase (days 7–21) (Figure S2E), while maintaining the purity of other lung lineages within vascularized human lung progenitor organoids (vHLPOs) (Figures 1F and 1G). Furthermore, platelet and endothelial cell adhesion molecule-1 (PECAM-1)-positive vascular ECs (10% of total cells) emerged concurrently with FOXF1-positive mesenchyme (Figure 1G). Notably, cell patterning and arrangement in the vHLPO resembled that of the embryonic mouse lung (Figure 1H). To quantify vHLPO architecture, we established a "vascular integration index" by measuring the shortest distance (SD) from each epithelial cell to the vascular bed surface in 3D reconstructed images (Figure 1I). By day 21, vHLPOs exhibited vascular integration and structures comparable to embryonic stage 12.5 day (E12.5) mouse lungs (Figures 1J and 1K; Videos S1 and S2; Figure 1L). This differentiation was reproducible across multiple iPSC lines (Figure 1M), and the integration of epithelium, mesenchyme, and vasculature was not observed in conventional lung organoid systems (Figure 1N).

Similarly, to generate vascularized human intestinal organoids (vHIOs) and colonic organoids (vHCOs), we added angiogenic factors with the conventional SI or colonic cocktail[21,22] to drive vMHG differentiation. Unlike the previous protocol that required BMP4 alongside other angiogenic factors to expand the limited proportion of the EC progenitors in the intestine organoid,[13] our strategy only required VEGFA and ANG1 from days 7 to 21 to effectively promoted the maturation of the endogenous vasculature, without compromising the epithelial lineage identity (Figures S2I–S2L), and demonstrated high reproducibility across various cell lines (Figure S2M). Although the vascular integration within vHIO exhibited a more compact distribution compared with the embryonic mouse intestine (Figures S2N and S2O), the differences in vascular structure were indistinguishable (Figure S2P).

(B) Whole mount staining of day 3 spheroids subjected to different durations of BMP4 treatment. FOXA2: definitive endoderm (DE); HAND1: lateral plate mesoderm (LPM).
(C) Whole mount staining and bright field images of day 7 vAFG and vMHG. PECAM 1: endothelium; FOXF1: mesenchyme; SOX2: AFG epithelium; CDX2: MHG epithelium.
(D) Quantification of vascular and epithelial purity from (C).
(E) Expression of vascular and epithelial markers in vAFG and vMHG across different stem cell lines.
(F) Left: bright field images of day 21 vascularized human lung progenitor organoid (vHLPO). Arrows: lung epithelium. Epi., epithelium; Mes., mesenchyme. Right: images of day 21 vHLPO derived from NKX2.1 GFP reporter iPSC line. NKX2.1: lung epithelium.
(G) Immunostaining and quantification of major cell types within vHLPO.
(H) Immunostaining of E16.5 mouse lung.
(I) Schematic diagram showing the vascular integration index calculation pipeline.
(J) Whole mount staining of day 21 vHLPO and E12.5 mouse lung.
(K) Vascular integration index plot for (J).
(L) Vascular structure parameters for (J).
(M) Expression of vascular and epithelial markers in vHLPO and vascularized human intestine organoid (vHIO) across different stem cell lines.
(N) Bright field and cross section staining of day 21 cLPOs.
(O) Immunostaining of day 21 vHLPO and vHIO epithelium under different durations of BMP4 exposure within the initial 3 days.
(P) Uniform manifold approximation and projection (UMAP) of day 3 meso endoderm spheroids.
(Q) DE subclusters BMP driving score and anterior (A) posterior (P) score. BMP driving score was derived based on the difference in the proportions of the cluster cells. A P score was calculated based on the difference in the fractions of the cluster cells mapped to the P vs. A cell types.
(R) Correlation between the A P projection and BMP driving scores within day 3 DE subclusters.
(S) Schematic illustration for BMP4 controlled DE A P region predisposition. In (E) and (M), *n* = stem cell line. Dots connected by the same line represented the same stem cell line. Otherwise, *n* = biological repeat. t test: (D, E, G, M, and L); two way ANOVA: (B and O). In (B), ***, ### "days 0 2" or "days 0 3" versus "NA"; data are represented as mean ± SEM.
See also Figures S1 S3, Table S1A, and Videos S1 and S2.

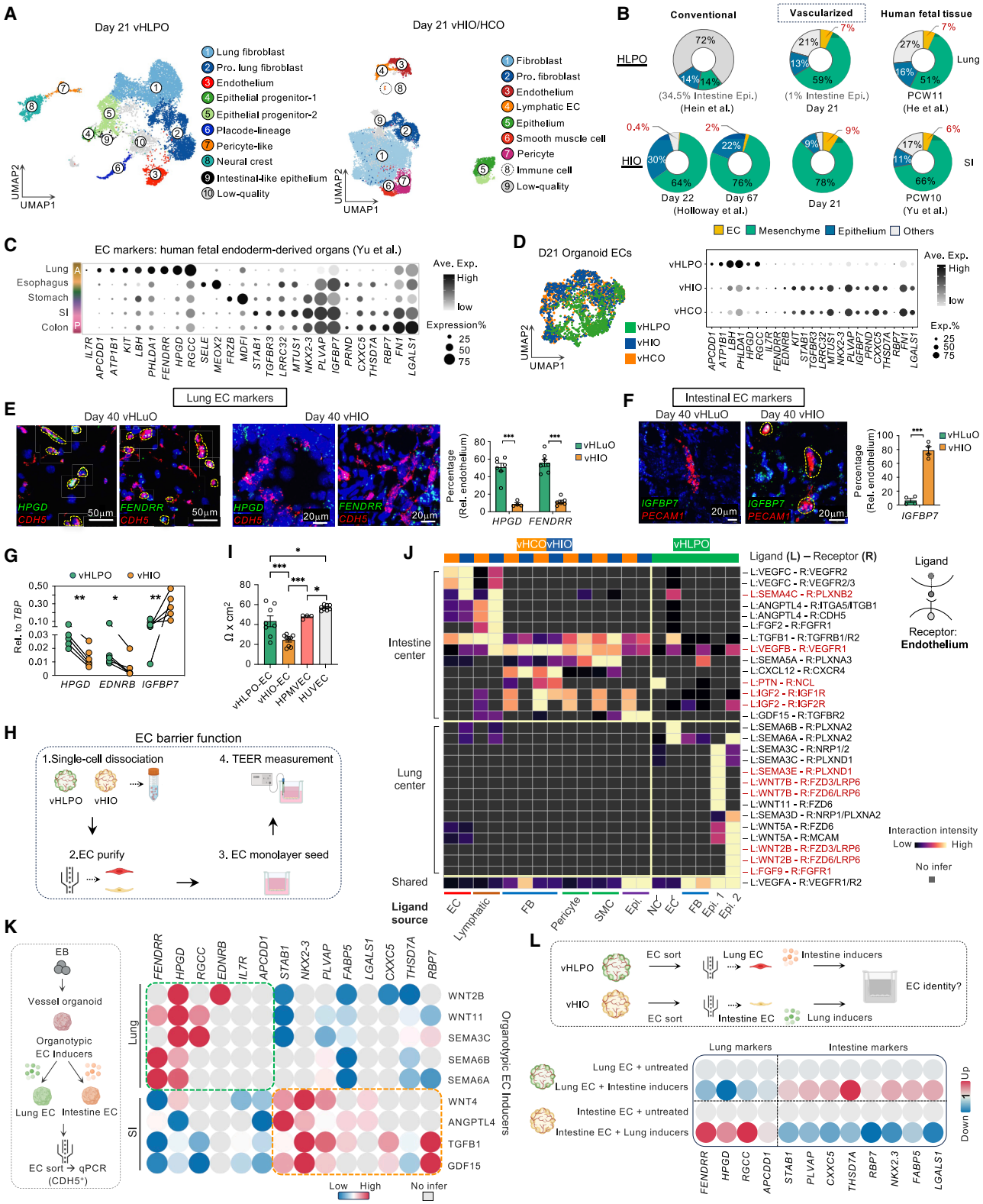

Figure 2. Organotypic endothelium in vascularized lung and intestine organoids

(A) UMAP of day 21 vascularized organoids. ECs, endothelial cells; Pro., proliferation.

(B) Cell type distribution from conventional and vascularized HLPO and HIO and human fetal lung and small intestine (SI) tissues.

(legend continued on next page)

Collectively, unlike previous methods focused on epithelial differentiation, our approach co-developed defined DE and mesodermal lineages within a single spheroid. This strategy resulted in the formation of multicellular organoid structures featuring extensive vasculature and a well-organized cellular architecture, supported by intricate intercellular communications.

Early-stage BMP regulation dictated late-stage gut tube patterning

Gut tube lineage specification in mice was previously thought to occur during primitive gut development, which corresponds to days 3–7 in our differentiation protocol[21,22,24] (Figures 1A, 1C, and S2).[19,20,25] However, we unexpectedly found that this process may initiate earlier than previously recognized, within the first 3 days of differentiation, and is primarily regulated by BMP signaling. During the early embryonic phase, in addition to its role in modulating mesoderm induction, BMP activation from days 0 to 1 favored the subsequent specification of anterior lung lineage at day 21 ($NKX2.1^{+}/CDX2^{-}$), whereas sustained BMP stimulation from days 0 to 3 promoted a posterior intestinal fate ($CDX2^{+}/SOX2^{-}$) (Figure 1O).

To further understand this early predisposition phenotype, we performed single-cell RNA sequencing (scRNA-seq) on day 3 meso-endoderm spheroids subjected to different durations of BMP4 treatment (Figures 1P, S3A, and S3B; Table S1A). Cardiac mesendoderm and endothelial progenitors co-emerged (Figures S3B and S3C) alongside endoderm, indicating early cross-lineage communications between the heart and adjacent endoderm.[26,27] Notably, DE clusters projected onto the human embryonic endoderm (Carnegie stage [CS] 7[28]) exhibited diverse features (Figure S3D). Analysis of their distribution across BMP4 treatment durations (Figure S3E) and BMP-driving scores (Figures 1Q and S3E) revealed that anterior-posterior (A-P) patterning was already detectable at day 3 (Figures 1Q and S3F–S3H), with a positive correlation with BMP-driving score (Figures 1R and 1S). These findings suggest that early BMP signaling may imprint A-P regional identity onto the heterogeneous DE population, which pre-determined the development trajectory of the gut tube at later stages of organogenesis. However, further validation in additional models is needed to confirm this concept.

ECs adopted organotypic features in vHLPOs and vHIOs

To further characterize the organotypic features within vascularized organoids, we performed scRNA-seq on the day 21 vHLPO, vHIO, and vHCO (Figures 2A and S3) and identified abundant endothelial, mesenchymal, and epithelial progenitor populations based on signature gene expression (Figures 2A, S3I, and S3J). Using human fetal lung atlas as a reference,[29] we further characterized heterogeneous lung epithelial, mesenchymal, and endothelial populations within vHLPO (Figures S3K–S3M). Fibroblasts resembled early human fibroblasts, mesenchyme, and myofibroblasts (Figure S3L); cluster 6 aligned with WNT-responsive myofibroblasts surrounding the stalk epithelium, expressing WNT-responsive genes[29] *LEF1* and *NOTUM* (Figure S3M). ECs resembled early fetal lung capillaries (Figure S3L), while cluster 12 epithelial progenitor-1 expressed lung tip-like markers *SOX9* and *TPPP3* (Figure S3I). In vHIO/vCHO,[24] lymphatic ECs (*LYVE1*$^{+}$/*PROX1*$^{+}$, Figure S3J) and a small immune cell cluster (Figure S3N) also emerged, providing a platform to study lymphatic development in the context of lipid transport and immunosurveillance in maintaining intestinal homeostasis.[30]

Cell-type distribution analysis revealed that our current protocol significantly enhanced EC differentiation in day 21 vHLPO (7%, Figure 2B) and day 21 vHIOs/vHCOs (9%, Figure 2B), as compared to conventional day 31 HLPO[31] (0%), day 22 HIO organoids[13] (0.4%), and day 67 HIO organoids[13] (2%, Figure 2B). More importantly, the co-emergence of appropriate vasculature and mesenchyme within vascularized organoids improved anterior epithelial lineage purity: conventional HLPOs showed 34.5% contamination with intestinal epithelium, whereas vHLPOs contained only 1% intestinal epithelium (Figure 2B). Notably, cell compositions in both vHLPO and vHIO organoids closely resembled those observed in human fetal lung[29] and SI[32] at 10–11 post-conceptional weeks (PCWs) (Figure 2B).

To evaluate the organ specificity of ECs in vascularized lung and intestine organoids, we first reanalyzed multiple independent human cell atlases[1,2,32,33] and defined specific markers for ECs in endoderm-derived organs (Figures 2C and S4A). Intriguingly, integration of EC clusters from vHLPO, vHIO, and vHCO showed organ-specific segregation, with lung ECs clustering separately from intestinal ECs (Figure 2D). Additionally, organoid ECs expressed corresponding marker genes of human fetal lung (*HPGD* and *APCDD1*), SI (*STAB1* and *MTUS1*), and

(C) Dot plot of organotypic EC markers generated based on scRNA seq data of human fetal organs.
(D) UMAP and dot plots of organ specific EC markers in day 21 vascularized organoids.
(E) Staining of human lung EC markers in day 40 vascularized organoids. *CDH5*: pan EC marker.
(F) Staining of human intestine EC marker in day 40 vascularized organoids. *PECAM 1*: pan EC marker.
(G) Expression of lung and intestine EC markers in day 40 vascularized organoids across different stem cell lines.
(H and I) Measurement of TEER EC barrier functions on organoid derived and primary ECs. HPMVEC, human pulmonary microvascular EC; HUVEC, human umbilical cord vein EC.
(J) Key L R pairs orchestrating cell cell communication in vascularized organoids. Receptors expressed by ECs were included. The dark gray blocks indicated L R pairs undetected. The red highlighted L R pairs shared between vascularized organoids and human fetal tissues. CellChat was used for the L R analysis. L, ligand; R, receptor; FB, fibroblast; SMC, smooth muscle cell; NC, neural crest cell.
(K) Key ligands revealed in (J) were supplemented to the generic VOs to induce organotypic EC. ECs were isolated for qPCR analysis. Right: heatmap for human fetal lung and intestine specific EC marker expressions in treated VOs.
(L) Organotypic ECs were sorted and treated with the opposing pools of organotypic EC inducers found in (J). The qPCR results were summarized in the heatmap. $n = 3$ biological repeats in each treatment group. In (G), n = stem cell line. Dots connected by the same line represented the same stem cell line. Otherwise, n = biological repeat. t test: (E) (G); two way ANOVA: (I). Data are represented as mean ± SEM.
See also Figures S3 and S4 and Table S2.

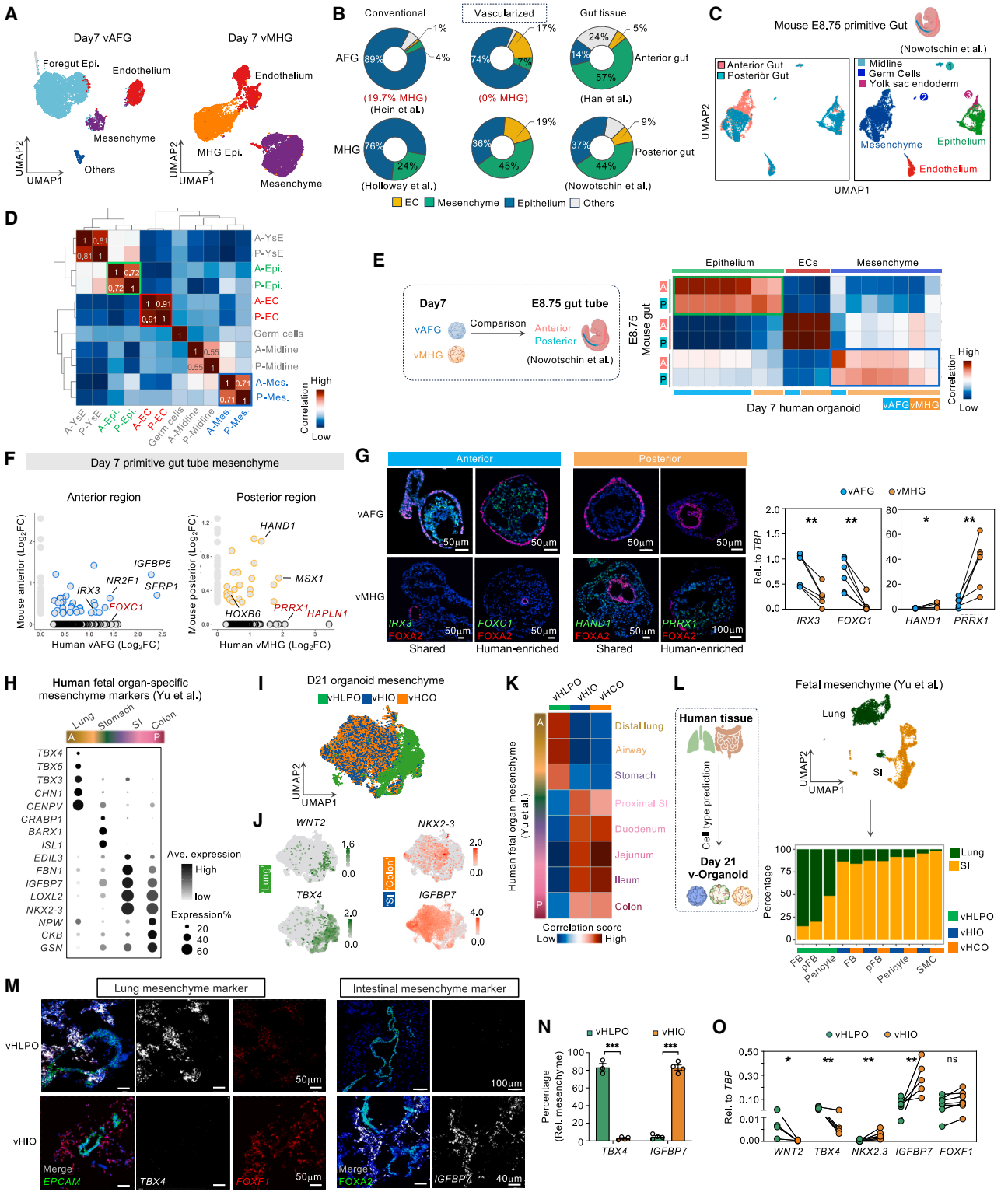

Figure 3. Organotypic mesenchyme within vascularized organoids

(A) UMAP of day 7 vAFG and vMHG.

(B) Cell type distribution of conventional and vascularized AFG and MHG and mouse anterior and posterior primitive gut tube.

(C) UMAP of E8.75 mouse anterior and posterior primitive gut tube.

(legend continued on next page)

colon EC (*THSD7A* and *CXXC5*) (Figures 2D and S4B; Table S2A). By day 40 with further maturation, vHLuO expressed markers of distal lung epithelium (SOX9$^+$/NKX2.1$^+$), AT2 cells (HTII-280), and AT1 cells (HT1-56/*HOPX*/*ANKRD1*)[34] (Figure S4C) and lung EC (*HPGD* and *FENDRR*)[33] (Figure S4D) but not in vHIO (Figure 2E). Conversely, the expression of human SI/colon EC marker *IGFBP7* was enriched in vHIO compared with vHLPO (Figures 2F and 2G).

These organ-specific features were also reflected at a functional level: ECs isolated from vHLPO demonstrated higher barrier function compared with those from vHIO, as measured by transendothelial electrical resistance (TEER) (Figures 2H and 2I). This aligns with the primary role of lung endothelium, which is to maintain a tight barrier to prevent fluid leakage into the alveoli for efficient gas exchange, whereas the intestinal endothelium requires greater permeability to facilitate nutrient absorption.[35–38] Moreover, vHLPO-derived ECs exhibited barrier integrity comparable to primary human pulmonary microvascular ECs (HPMECs),[39] and lower than that of HUVECs.[40]

Microenvironment determinants of organotypic ECs and their plasticity

To identify microenvironmental signals driving organ-specific EC development, CellChat analysis was performed on day 21 vascularized organoids (Figure 2J; Table S2B) and human fetal tissues (Figure S4E; Table S2C). While known ligands such as WNT2B, WNT7B, and VEGFA for lung[41–44] and VEGFB[45] for intestine were detected, most ligands targeting organotypic ECs uncovered here have not been characterized. These newly identified ligands were consistently found in both organoids and human fetal tissues, such as SEMA4C from intestine epithelium, IGF2 from intestine epithelium and mesenchyme, FGF9 from lung mesenchyme, and SEMA3E from lung epithelium (Figures 2J and S4E, highlighted in red). Notably, several WNT and semaphorin family ligands preferentially contributed to lung ECs specification over intestinal ECs (Figures 2J and S4E), suggesting that selective manipulation of these pathways could promote lung EC differentiation.

Next, we evaluated the ability of these ligands to guide organ-specific EC specification in generic 3D vessel organoids (VOs)[46] that lack defined organ identity.[47] After exposing the VOs to candidate morphogens individually, we found that WNT2B, WNT11, SEMA3C, SEMA6A, and SEMA6B were effective in promoting the lung EC signature, whereas WNT4, ANGPTL4, TGFB1, and GDF15 were effective in driving generic ECs toward an intestinal cell fate (Figure 2K).

To further assess the plasticity of ECs in the vascularized organoids, we isolated ECs and sub-cultured them independently in the absence of surrounding tissue-specific cell types, where they rapidly lost their original tissue-specific features (Figure S4F). When exposed to intestinal EC inducers, lung ECs from vHLPO acquired intestinal-like characteristics, and vice versa (Figure 2L), highlighting their high plasticity in response to external signals.

Distinct organotypic features in vascularized gut organoid mesenchyme

Next, we characterized the organ-specific features of the mesenchyme throughout the organoid differentiation. First, we performed scRNA-seq on day 7 vAFG and vMHG (Figure 3A). We focused on the vAFG-"B1" and vMHG-"B3" groups, given their optimal induction of days 7 and 21 multilineage organoids (Figures 3A, S4G, and S4H). Our current protocol significantly enhanced mesenchymal and endothelial differentiation in both vAFG and vMHG as compared with the conventional day 10 AFG[31] and day 8 hindgut[13] (Figure 3B). In vAFG, MHG contamination was negligible (~0%) compared with the contamination (19.7%) observed with the conventional AFG differentiation protocol (Figure 3B). The cell composition distributions within vMHG organoids closely resembled those found in the E8.75 mouse posterior gut atlas,[48] while vAFG organoids contained less mesenchyme and more EC and epithelium as compared with E9.0 mouse anterior gut[49] (Figure 3B).

In E8.75 mouse primitive gut tube,[48] A-P identity was predominantly observed in mesenchyme and epithelium but less pronounced in ECs (Figures 3C, 3D, S4I, and S4J; Table S1B). Similar A-P patterning was found in day 7 vAGF and vMHG, with clear A-P identity in mesenchyme and epithelium but not in ECs (Figure 3E). Additionally, we unveiled both known (*Hoxb6* and *Hand1*)[49] and new markers distinguishing the anterior from posterior gut tube mesenchyme, shared across species or human-specific (highlighted in red) (Figure 3F; Table S1C). These results were subsequently validated in human vAFG and vMHG organoids (Figures 3G, S4K, and S4L).

To further determine the organotypic signatures of the mesenchyme within day 21 vascularized organoids, we first analyzed the mesenchymal populations from human fetal endodermal organs[32] to define their organ specificity (Figure 3H). Intriguingly upon integration of mesenchymal cells from day 21 vascularized

(D) Pseudo bulk similarity analysis of major cell types within anterior versus posterior E8.75 mouse primitive gut tube. YsE, yolk sac endoderm; Mes, mesenchyme; A, anterior; P, posterior.
(E) Pseudo bulk similarity analysis between day 7 vascularized human primitive gut organoids and E8.75 mouse gut.
(F) scRNA seq identified anterior and posterior specific genes for mouse and human primitive gut mesenchyme.
(G) smFISH (left) and qPCR (right) revealed anterior and posterior mesenchymal genes in day 7 vascularized primitive gut organoids.
(H) Dot plot showing marker genes of human fetal organ specific mesenchyme.
(I) UMAP of mesenchymal cells from day 21 vascularized organoids.
(J) Feature plots of lung and SI/colon specific mesenchymal markers.
(K) Pseudo bulk similarity analysis on mesenchyme between vascularized lung and intestine organoids to human fetal organs.
(L) Automated cell annotation of organoid mesenchyme based on human fetal lung and SI mesenchyme reference map.
(M O) smFISH (M and N) and qPCR (O) analyses showing organotypic mesenchymal markers identified in (J) in day 21 vHLPOs and vHIOs. *FOXF1,* generic mesenchyme. In (G) and (O), *n* = stem cell line. Dots connected by the same line represented the same stem cell line. Otherwise, *n* = biological repeat. t test: (G, N, and O). Data are represented as mean ± SEM.
See also Figure S5 and Table S1.

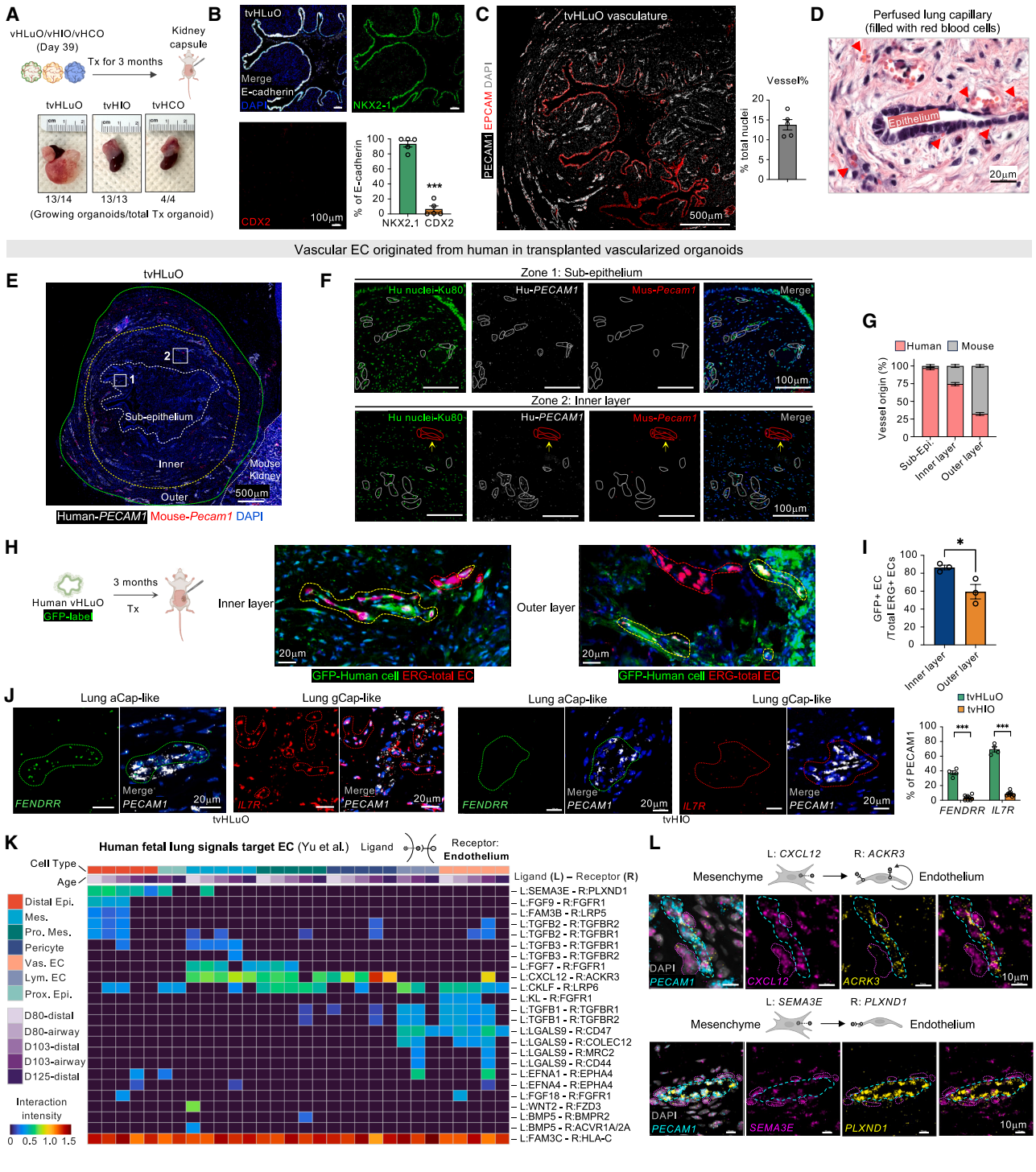

Figure 4. *In vivo* maturation of human vascularized lung and intestine organoid

(A) *In vitro* vascularized organoids were transplanted under the kidney capsule of immuno compromised mice. The numbers indicated the successful versus total transplanted organoid.

(B) Immunostaining of lung (NKX2.1) and intestine (CDX2) epithelium in transplanted vascularized lung organoid (tvHLuO). E cadherin: pan epithelium marker.

(C) Immunostaining of EC (PECAM 1) and epithelial cells (EPCAM) within tvHLuOs.

(D) H&E staining of the explanted tvHLuO. Arrowhead: capillary vessel filled with RBC.

(E) Staining of the origin of vessels within vascularized lung organoids by human and mouse specific *PECAM 1* smFISH probes and Ku80 human nuclei antibody. Dashed lines circled different layer structures based on the distance from the epithelial layer.

(F) Zoom in images of zone 1 (sub epi) and zone 2 (inner layer) from (E).

(legend continued on next page)

organoids, lung and intestinal mesenchymal populations segregated distinctly and expressed corresponding human fetal gut mesenchymal markers[50] (Figures 3I and 3J; Table S1D). Similarity analysis revealed the vascularized organoids closely resembled human fetal gut tissues regarding their mesenchymal properties along the A-P axis (Figures 3K and 3L). The organotypic features of the vHLPO and vHIO mesenchyme were further validated through single molecule fluorescence *in situ* hybridization (smFISH) staining of the lung-specific marker *TBX4* and the intestine-specific marker *IGFBP7* (Figures 3M–3O).

Maturation of vascularized lung and intestinal organoids *in vivo*

To enhance maturation and perfusion, vascularized gut organoids were transplanted under the kidney capsule of immuno-compromised mice for 3 months[51] (Figure 4A). Following transplantation, the transplanted vHLuOs (tvHLuOs) developed well-organized branching morphology with high lung epithelial purity (Figure 4B), extensive vascularization (Figure 4C), and perfusable sub-epithelial capillary beds filled with mouse red blood cells (Figures 4D and S5A). Notably, these structures were rarely presented in the conventional epithelial organoids after transplantation[17] (Figure S5B). The majority of the vasculature adjacent to the organoid epithelium originated from human hPSC rather than the host, as assessed by species-specific antibody and RNA probes (Figures 4E–4G). This conclusion was further supported by tracing host-derived cells in tvHLuOs generated from the GFP-ESC line (Figures 4H and 4I). Notably, the presence of perfused vessels indicated by anastomotic structures served as a hallmark for improved organoid engraftment *in vivo* (Figure S5C). Additionally, increased diversity of proximal and distal lung epithelial cell types was observed in tvHLuO after transplantation (Figure S5D). Similarly, tvHIO and tvHCO also developed a well-organized intestinal structure with a large lumen (Figure S5E), a pure intestine epithelial identity (Figure S5F), a perfusable sub-epithelial vascular bed (Figure S5G), and extensive vascular formation that was absent in conventional tHIO and tHCO (Figure S5H). Host-derived vascular cells contributed to vascular beds adjacent to the intestinal epithelium (Figure S5I), along with diverse intestinal epithelial cell types (Figure S5J).

We also characterized the recently discovered alveolar capillary EC subtypes, known as aerocyte (aCap) and general capillary ECs (gCap)[2,33,44,52] in tvHLuOs. smFISH demonstrated the presence of both aCap-like cells (*FENDRR*$^{+}$) (Figure 4J) and gCap-like cells (*IL-7R*$^{+}$/*KIT*$^{+}$) (Figures 4J and S5K) that were absent in tvHIO. Conversely, intestinal EC marker *IGFBP7* was exclusively expressed in tvHIO over tvHLuO (Figure S5K). Similarly, organotypic mesenchymal markers continued to be expressed within the corresponding transplanted organoids (Figure S5L).

To further investigate the cell-cell interactions contributing to EC maturation and specification, we analyzed ligand-receptor (L-R) pairs targeting lung ECs in human fetal lung tissue (Figures 4K and S6A; Table S3A). Key pairs such as CXCL12-ACKR3 and SEMA3E-PLXND1, secreted by surrounding mesenchyme or ECs, were confirmed in tvHLuO by smFISH (Figure 4L). To focus specifically on L-R pairs expressed by neighboring cells, we utilized a Slide-seq-based spatial transcriptomics platform[53] (Figures S6B and S6C) to unbiasedly map the spatial distribution of L-R pairs in tvHLuOs. Among 116 L-R pairs driving human fetal lung EC development, 41 of them were captured in tvHLuO (Figure S6D), including representative L-R pairs shown in Figure 4L (Figure S6E).

Improvement of epithelial maturity and diversity in vHLPOs

Supported by neighboring vasculature and mesenchyme, the epithelium from the day 21 vHLPO showed a higher similarity score to human fetal lung epithelium at a later developmental stage[29] compared with the conventional lung progenitor organoids (cLPOs) (Figures 5A, S6F, and S6G). Similarly, the SI epithelium from vHIO was more mature than that in conventional small intestine organoid (cHIO) when compared with human fetal intestine[32] (Figures S6H–S6J). Notably, direct comparisons of the epithelium from vascularized versus conventional lung organoids revealed decreased expression of *KRT19* and *CLDN4* (Figure 5B; Table S3B), which are associated with pre-alveolar type-1 transitional cell state (PATS) cells that exhibit DNA damage and senescence during tissue repair and are enriched in fibrotic lung disease.[54–56] Pathway enrichment analysis revealed that cLPO exhibited activation of pathways related to DNA damage, apoptosis, and cell death, whereas pathways associated with lung morphogenesis and development were dominant in the vHLPO epithelium (Figure 5C). Genes enriched in vHLPOs compared with cLPOs, such as *SEMA3E* and *MECOM*, are known to be upregulated during human lung maturation (Figures 5B, 5D, and S6K).

Interestingly, we also identified a recently discovered human respiratory airway secretory (RAS) cell type[57,58] (SCGB3A2+ and SCGB1A1+) within tvHLuOs (Figure 5E). This unique cell type is located in the respiratory bronchioles, a region absent in mice. Proteomic profiling of the secreted fluid confirmed that, other than all major lung secretory products, including surfactant proteins and mucins (Figure 5F), the secretion of

(G) Quantification of vessel origin within tvHLuO from (E). *n* = 10 regions from two different tvHLuO samples.
(H) GFP labeled vascularized lung organoids were transplanted under the kidney capsule to trace the cell origin. ERG: total EC; GFP: cells from human organoids.
(I) Quantification of vessel origin within tvHLuO from (H).
(J) smFISH detection of organotypic EC in tvHLuO and tvHIO.
(K) Heatmap of L R gene expressions in human fetal lung scRNA seq from Yu et al.[32] Receptors are expressed in lung endothelium. CellphoneDB was used for L R interaction analysis. Zero intensity represents an interaction that is not significant or the ligand and/or the receptor was not expressed.
(L) smFISH detection of representative L R pairs revealed in (K) in tvHLuO. PECAM1: pan EC marker. *n* = biological repeat. t test: (B, I, and J). Data are rep resented as mean ± SEM.
See also Figure S6 and Table S3A.

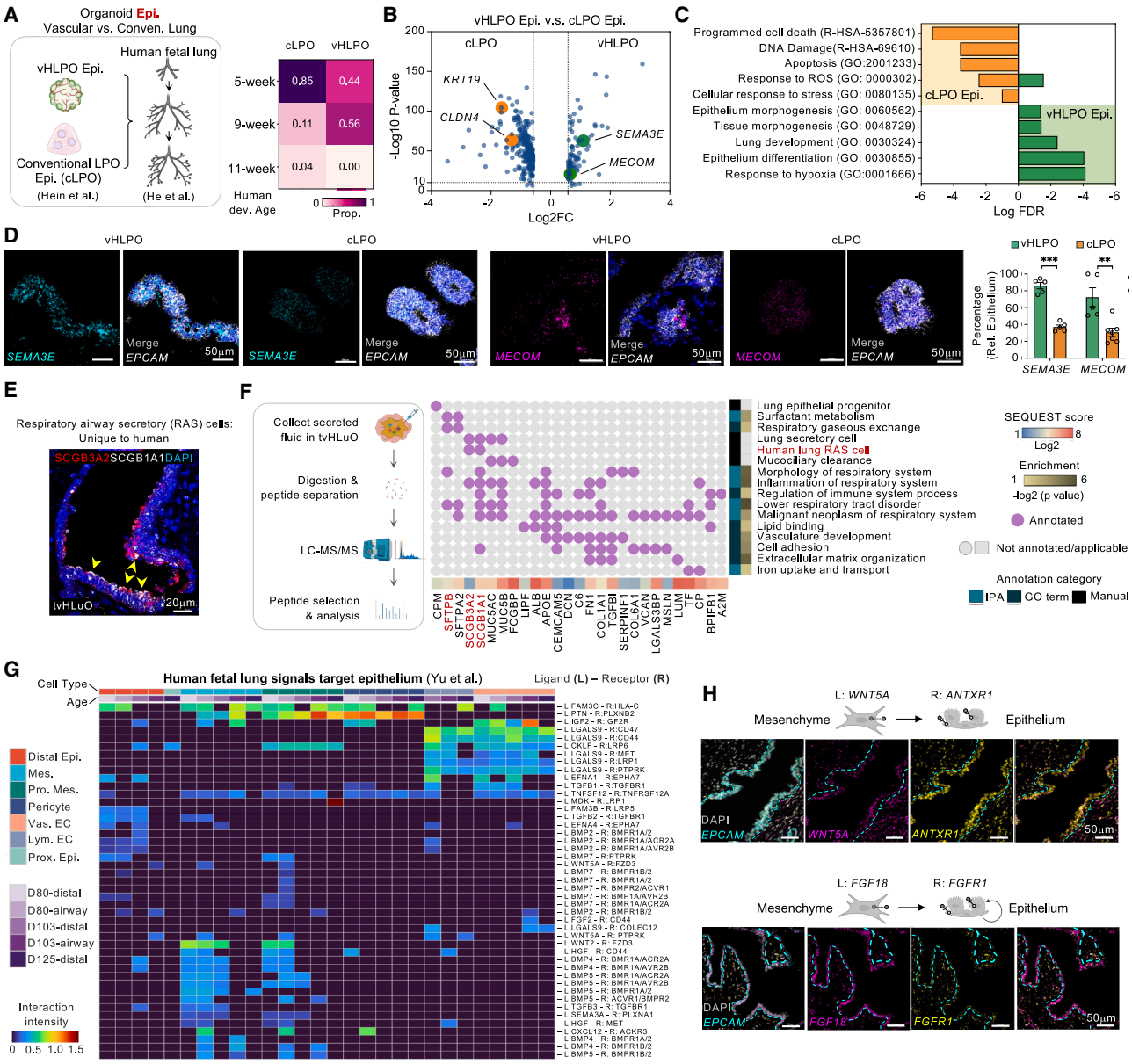

Figure 5. Improvement of epithelial maturity in vascularized lung organoids

(A) Proportions of cells projected to each human fetal lung development stage were shown as heatmap. Prop., proportions; cLPO, conventional lung progenitor organoid.

(B) Volcano plot for DEGs between day 21 vHLPO epithelial progenitor 1 and cLPO bud tip progenitor cells.

(C) Enriched pathways for vHLPO and cLPO epithelium. Enrichment analysis was performed using Metascape (https://metascape.org) based on DEGs shown in (B). GO, Gene Ontology; R HSA, Reactome.

(D) smFISH staining of mature vHLPO epithelium markers in day 21 vHLPO and vLPO.

(E) Staining of human RAS cells in tvHLuO. Yellow arrowheads indicated positive RAS cells.

(F) Proteomic analysis of fluid combined from two tvHLuO after 3 month transplantation. The red: human lung RAS cell markers.

(G) Heatmap of L R gene expressions in human fetal lung scRNA seq from Yu et al.[32] Receptors are expressed in lung epithelium. CellphoneDB was used for L R interaction analysis. Zero intensity represents an interaction that is not significant or the ligand and/or the receptor was not expressed.

(H) smFISH detection of representative L R pairs revealed in (G) in tvHLuO. EPCAM: pan EC marker. *n* = biological repeat. t test: (D) data are represented as mean ± SEM.

See also Figure S6 and Table S3.

SCGB3A2, SCGB1A1, and SFTPB peptides were also observed, which are uniquely produced by active RAS cells.[57,58] Functional proteins critical for lung development and homeostasis were also identified, including BPIFB1, A2M, and C6 involved in immune modulation, and collagen and fibronectin contributing to early lung structure formation and remodeling.

To uncover the cell-cell interactions contributing to lung epithelial development and maturation, spatial information in tvHLuO was mapped (Figures S6B and S6C) and further compared with publicly available human fetal lung atlas[29,32] (Figures 5G and S6L; Table S3C) and spatial atlas.[59] Key L-R pairs, such as WNT5A-ANTXR1 and FGF18-FGFR1, were expressed by surrounding mesenchyme or epithelium and associated with epithelial maturation in tvHLuO. These interactions were validated by smFISH (Figure 5H) and spatial transcriptomics (Figures S6M and S6N).

Collectively, the emergence of organotypic vascular and mesenchymal populations within the vascularized organoids has promoted both the maturation and cell-type diversity of the epithelium, thereby establishing a robust foundation for the development of functional organ units.

Formation of alveolar structure on bioengineered scaffold

To reconstruct alveolar architecture with juxtaposed epithelium, capillary endothelium, mesenchyme, and extracellular matrix *in vitro*, we replated the dissociated vHLPOs onto an air-liquid interface (ALI) culture to induce distal lung structure formation (Figure 6A). Intriguingly, the dissociated vHLPO cells autonomously formed alveolar sac-like structures, whereas cells of cLPO consisting primarily of iPSC-derived AT2 epithelium (iAT2) with minimal mesenchyme and ECs only formed a monolayer structure (Figure 6B). Inspired by these results, we further optimized the previously reported 3D porous gelatin methacryloyl (GelMA) lung scaffold[60] by incorporating hyaluronic acid methacrylate (HAMA)[61,62] to facilitate epithelium, mesenchyme, and vascular EC arrangement (Figure 6C). After seeding the dissociated vHLPOs on the lung scaffold (Figure 6D), the ECs aligned along the hydrogel sac surface (Figure 6E, left, yellow dashed line) and surrounded the lung epithelial bud (Figure 6E, right; Video S3). Notably, lung alveolar cell types emerged with proper alveolar geometric organization when grown on the scaffold, such as AT1- and AT2-like lung epithelium (Figure 6F) and aCap-like and gCap-like lung endothelium (Figure 6G). Additionally, the ultrastructure of lung organoid cells grown on the scaffold exhibited morphologies resembling AT1 and AT2 cells observed in fetal lungs[63–65] (Figure 6H): cuboidal cells with glycogen but no lamellar bodies (bipotent progenitors [BPs]), cuboidal cells with glycogen and lamellar bodies (early AT2 cells), and partially flattened cells (early AT1 cells). Consistently with whole-mount imaging results (Figure 6E), physical juxtaposition between early AT1 cells and ECs were observed (Figure 6I), indicating the initiation of early functional barrier unit formation.

Modeling congenital lung and intestinal defects caused by FOXF1 variants in vHLuOs and vHIOs

Conventional lung organoids lack vascular and mesenchymal components, limiting their use in studying pulmonary vascular diseases such as ACDMPV or ACD—a fatal congenital lung disorder caused by mutations or deletion in *FOXF1*, with no effective therapy.

We generated vHLuOs from iPSCs derived from three ACD patients and three healthy controls (Figures 7A and S7A). One patient (ACD-1, also known as "FOXF1.1" iPSC line) has a 1.7Mb chromosome deletion containing the *FOXF1* locus,[66] while the other two carried different heterozygous *FOXF1* mutations (c.166C>G and c.253T>A, ACD-2 and ACD-3)[67] (Table S4A). Both point mutations are located in the FOXF1 DNA-binding domain and were predicted by AlphaMissense[68,69] to be likely pathogenic (pathogenicity score: 0.9977 and 0.9999, respectively). A recent study also revealed that these mutations significantly reduced the DNA-binding capacity of FOXF1, suggesting that they are likely loss-of-function mutations.[70] In ACD vHLuOs, we observed significantly decreased capillary formation and reduced aCap and gCap populations compared with controls (Figures 7B and 7C). Interestingly, despite the absence of *FOXF1* expression in lung epithelial cells, we observed a decrease of distal lung epithelium ($SOX9^+$, $NKX2\text{-}1^+$) (Figure 7D), impaired AT1 differentiation ($HOPX^+$) (Figures 7E and 7F), and an accumulation of damage-associated AT1/AT2 intermediate cells ($CLDN4^+/NKX2.1^+$) (Figures 7G and 7H) in ACD vHLuOs.[54–56] These cell non-autonomous abnormalities in epithelial cells are likely attributed to the surrounding defective endothelial and mesenchymal populations and disrupted cell-cell crosstalk. Notably, these cellular phenotypes closely resembled those found in human ACD lung tissues[71] (Figure 7L) and could not be fully replicated in the *Foxf1*-mutant mouse model[72] or conventional lung organoids due to its absence of $FOXF1^+$ mesenchymal and endothelial components (Figures 6I–6K and S7B–S7D).

In addition to lung defects, ACD patients often present with extrapulmonary anomalies such as intestinal atresia and malrotation.[73] Our vHLuO and vHIO models offer an advanced platform to study both pulmonary and intestinal manifestations of ACD. In three ACD vHIOs, we observed reduced endothelial ($PECAM1^+$) and mesenchymal ($FOXF1^+$) populations compared with controls (Figures S7E and S7F). The mesothelial population ($WT1^+$) was also found to be suppressed in ACD vHIOs (Figure S7F), which is crucial for the formation of connective tissues that facilitate intestinal movement and suspension,[74] and a major source of smooth muscle cells in the gut vasculature.[75] The reduction of mesothelial cells may offer a partial explanation for the intestinal malrotation observed in ACD patients. Additionally, ACD vHIOs also showed an impaired differentiation of posterior gut tube epithelium ($FOXA2^+$, $CDX2^+$) alongside the appearance of ectopic anterior marker ($SOX2^+$) (Figures S7D and S7G).

DISCUSSION

Our study recapitulated the concurrent development of multiple germ layers, fostering essential cell-cell communication during the initial phase of human development—a critical feature lacking in assembloid models.[76] Therefore, the epithelial maturity and organotypic EC functions within the multilineage organoids more closely resembled those found in human fetal organs as compared with the conventional organoid models. This strategy

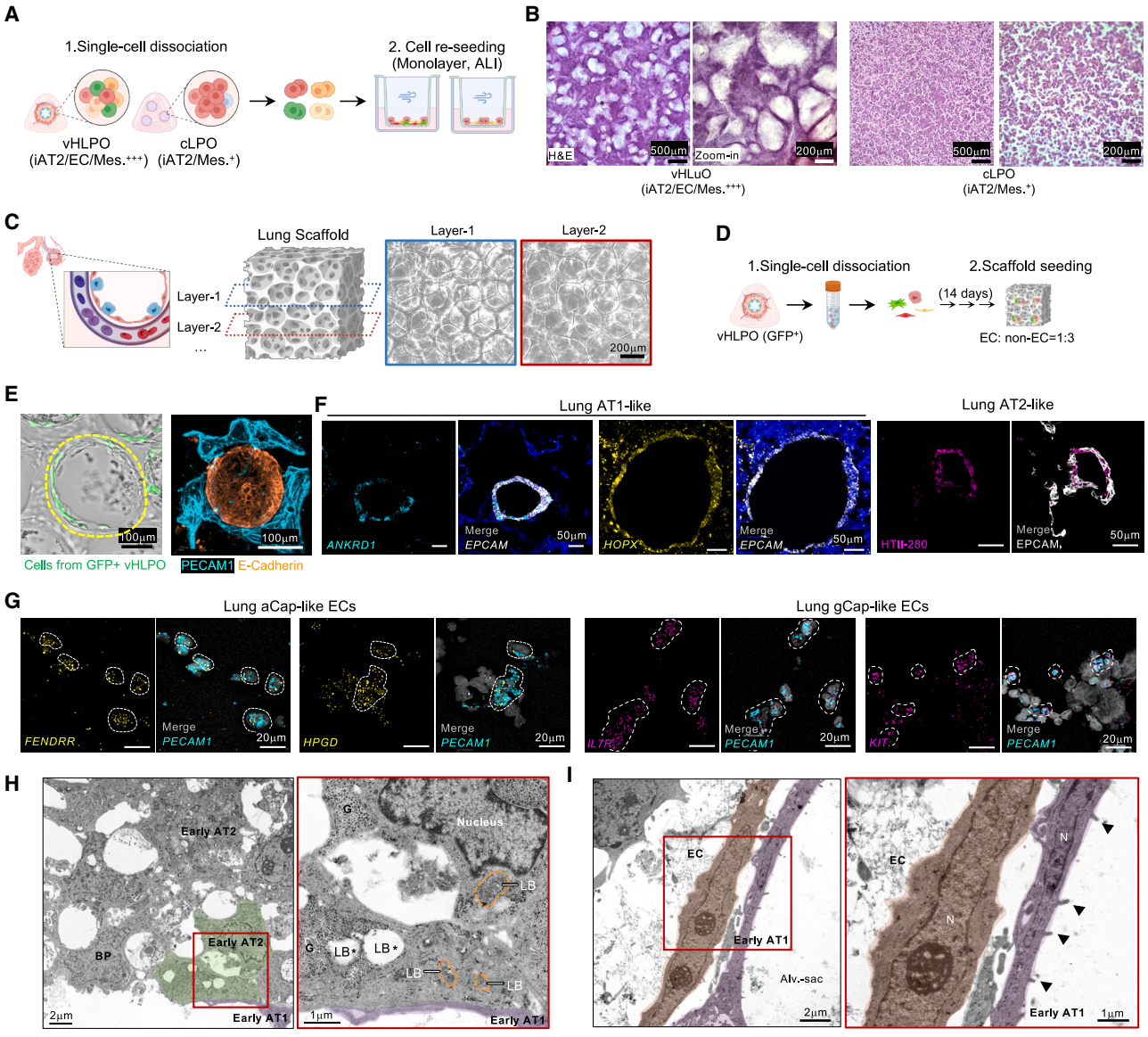

Figure 6. Formation of alveolar structure via vHLPO and bioengineered scaffold

(A) vHLPO and cLPO were reseeded to form air liquid interface (ALI). iAT2, iPSC derived AT2.

(B) H&E staining of re seeded lung organoid cells from (A).

(C) Diagraph and bright field images showing HAMA GelMA lung scaffold.

(D) Day 21 vHLPO was seeded onto the lung scaffold from (C).

(E) Left: bright field image showed GFP positive vHLPO cells growing along the surface of the lung scaffold sac. Right: whole mount staining of stretching vascular ECs (PECAM1^{+}) wrapping the lung epithelium (E cadherin^{+}).

(F) Identification of AT1 like and AT2 like cells from (D).

(G) Identification of lung aCap like and gCap like endothelium from (D).

(H) The ultrastructure of lung organoid cells cultured on engineered scaffold assessed by electron microscopy. Left: early AT1, early AT2, and BP detected in the lung organoids. BPs, bipotent progenitors. Right: zoom in image. G, glycogen; LBs, lamellar bodies. Asterisks indicated the extracted LB in early AT2.

(I) Sub cellular structure of the lung epithelium endothelium boundary assessed by electron microscopy. Left: cell to cell interaction between flattened squa mous early AT1 and ECs. Right: zoom in image. N, nucleus. Arrowhead, sparse microvilli.

See also Video S3.

addressed the limitations of existing models[9,77] by generating a diverse array of cell types originating from both mesoderm and endoderm, such as aerocytes[33] and RAS cells,[57] which have not been described in previous lung organoid models yet crucial for human alveolar development and regeneration. Additionally, it provided a system for defining markers that distinguish anterior

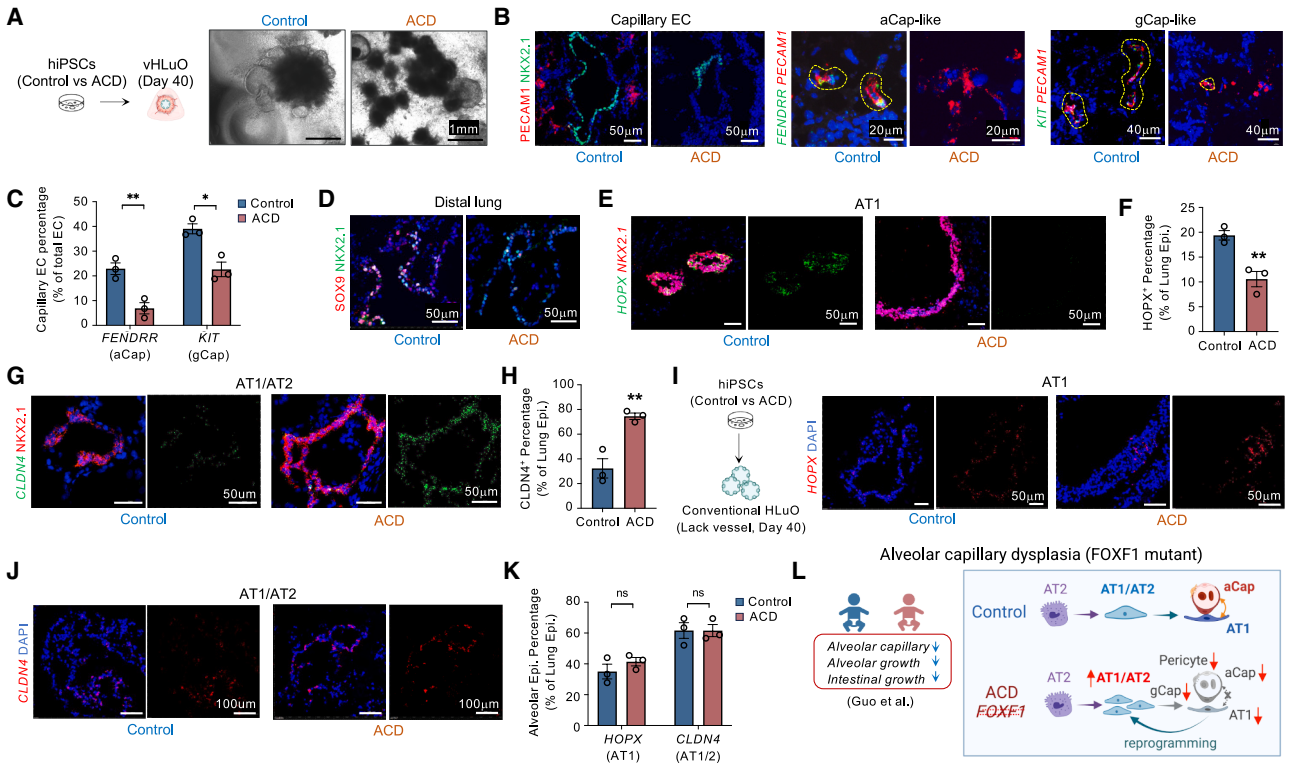

Figure 7. Determining cellular phenotypes caused by *FOXF1* mutations by utilizing patient specific vHLuOs

(A) Bright field images of day 40 vHLuOs differentiated from healthy control or ACD iPSCs.

(B and C) Immunostaining of lung capillary EC markers in both control and ACD vHLuOs. Yellow dashed lines highlighted the *FENDRR*$^+$/*PECAM1*$^+$ aCap or *KIT*$^+$/*PECAM 1*$^+$ gCap.

(D H) Immunostaining for distal lung, AT1, and AT1/AT2 markers in control and ACD vHLuOs, followed by statistical quantification of the percentage of alveolar epithelial subtypes.

(I K) Immunostaining of AT1 and AT1/AT2 markers in both control and ACD conventional HLuOs followed by statistical quantification.

(L) Cellular abnormalities attributed to FOXF1 mutations identified through scRNA seq analysis of lung tissues from control and ACD patients, as reported by Guo et al.[71] All data represent mean ± SEM. t test: (C, F, H, and K). *n* = 3 iPSC lines.

See also Figure S7 and Table S4A.

versus posterior gut tube mesenchyme, which had previously remained unclear due to the restricted availability of early human embryonic tissues.

Our research uncovered the dual impact of BMP signaling during the initial 3 days of differentiation, balancing mesoderm and endoderm while pre-determining A-P gut tube patterning. While prior studies focused on inducing DE or mesoderm via TGF-β, WNT, and BMP pathways,[13,15,19,21,22,28,46] our approach identified BMP as the only factor required to fine-tune both DE and mesoderm in our system. The diverse DE clusters observed aligns with findings reported by Mahaddalkar et al., which identified multiple gut tube progenitors potentially contributing to the production of more mature insulin-producing β-like cells.[78] While consistent with the recognized role of BMP signaling in embryonic posteriorization,[20] this finding unveiled an unexpected BMP-driven predisposition to gut tube lineage fate determination as early as the DE stage.

Vascularization of organoids, particularly for the organs derived from the endoderm, continues to pose a significant technical bottleneck. Previous studies by Holloway et al.[13] and Childs et al.[14] introduced angiogenic factors with BMP4 during the generation of small intestinal organoids to promote the growth and expansion of endogenous vessels that arose sporadically during the differentiation process. While ECs generated through that method partially resembled the endothelial gene profile of the human fetal SI, vessels were still limited in number, structurally underdeveloped, and often lacked organ-specific features and full functionality. In contrast, our protocol is designed to consistently and reliably generate functional and organotypic vessels in tandem with epithelial structures.

More importantly, existing methods for generating lung organoids have yet to successfully generate lung-specific vasculature, likely due to prior protocols that focused on anterior foregut patterning through strong BMP and TGF-β inhibition, conditions that may have impeded vasculogenesis. Through well-controlled mesoderm-endoderm co-differentiation, implementing BMP inhibition at optimal levels, appropriate patterning of gut tube epithelial fate, and precise temporal control of angiogenic factors, we successfully introduced human vasculature with organ specificity into lung organoids.

Another significant challenge in the field is the generation of organotypic ECs that faithfully replicate primary tissue-specific ECs at both molecular and functional levels. Herein, we consolidated a list of unreported morphogens that specifically target lung or intestinal ECs. Among the various WNT family genes, Wnt4 was found in the posterior intestinal epithelium, while Wnt11 was expressed in the anterior esophagus and stomach.[79] In addition to its role in gut epithelium patterning, we found that human WNT4 ligand also enhanced the expression of genes such as *STAB1*, *NKX2-3*, and *PLVAP*, which were representative of intestinal EC features. On the other hand, WNT11 induced the expression of lung EC and aerocyte genes while suppressing the posterior intestinal EC gene signature. Semaphorin signaling, known to play a role in various processes contributing to circulatory system development, has also been implicated in branching morphogenesis in the kidney and lung.[80] Our study demonstrated that certain semaphorins, such as SEMA3C and SEMA6A/B, were more effective in inducing lung EC over intestinal EC gene signatures. Collectively, these newly defined EC morphogens hold great potential for generating specialized organotypic vasculature with high efficiency for organoid engineering and even therapeutic purposes.

Beyond its application in studying human organ development, our multilineage vascularized organoid models serve as a suitable tool for recapitulating complex genetic disorders, particularly in uncovering cell non-autonomous mechanisms. Here, we showcased that severe underdevelopment of pulmonary and intestinal epithelium in ACDMPV is directly attributed to aberrant vascular and mesenchymal populations driven by the *FOXF1* loss-of-function mutation. However, the conventional lung organoid models, limited by their absence of FOXF1-expressing cells mediating multicellular interactions, failed to recapitulate the epithelial abnormalities and establish comprehensive genotype-phenotype connections. Our multilineage organoids provide an advanced platform to investigate both cell autonomous and non-autonomous phenotypes in a variety of congenital lung disorders, such as pulmonary hypoplasia and alveolar dysplasia caused by *TBX4* mutation,[81] a key transcription factor exclusively expressed in the lung mesenchymal compartment.

This study introduces a broadly applicable platform for generating multilineage organoids with organotypic endothelial and mesenchymal compartments. The complex 3D architecture and cellular diversity of these iPSC-derived organoids present a promising avenue for personalized regenerative therapy, especially for organs with vascular defects. These vascular networks can also be integrated with microfluidic chip systems to enable dynamic studies of immune-endothelial interactions. Furthermore, given that ECs are primary targets during transplant rejection, vascularized organoids provide a powerful model for investigating the mechanisms of EC-mediated allograft failure in antibody-mediated rejection.

Limitations of the study

It is important to note that our vascularized organoids exhibit characteristics akin to the human fetal stage, suggesting that additional maturation may be needed to achieve full functional capacity. This could potentially be addressed by introducing relevant biophysical cues such as perfusion, mechanical stretch, and oxygen gradients. Although the system has been extensively tested across nine iPSC lines in multiple laboratories, its reproducibility could be further improved through reagent standardization and simplification of the protocol. Testing a broader range of human iPSC lines from individuals of different ages, genders, and ethnicities will further enhance the generalizability of the approach. Additionally, the vascularized organoids do not include immune or neural components, which are important for organ development, disease modeling, and transplantation research. Future iterations may need to incorporate these elements for more comprehensive studies.

RESOURCE AVAILABILITY

Lead contact

Further information and requests for resources and reagents should be directed to and will be fulfilled by the lead contact, Mingxia Gu (MGu@mednet.ucla.edu).

Materials availability

This study did not generate new unique reagents.

Data and code availability

- The raw and processed data from scRNA seq in this study have been deposited with the Gene Expression Omnibus (https://www.ncbi.nlm.nih.gov/geo/). Accession numbers are listed in the key resources table. This paper analyzes existing, publicly available data. Related information for those datasets is listed in the key resources table. The mass spectrometry proteomics data have been deposited to the ProteomeXchange Consortium via the PRIDE partner repository (https://www.ebi.ac.uk/pride/). Accession numbers are listed in the key resources table.
- All original code has been deposited at https://github.com/MZGuo lab/Vascularized human organoids (DOI: https://doi.org/10.5281/zenodo.15428662) and is publicly available as of the date of publication.
- Any additional information required to reanalyze the data reported in this paper is available from the lead contact upon request.

ACKNOWLEDGMENTS

We thank the Discover Together Biobank for support of this study and the participants and their families, whose help and participation made this work possible, and Dr. Matt Kofron from Cincinnati Children's Bio Imaging and Analysis Facility and Joseph Kitzmiller from Division of Pulmonary Biology, CCHMC, for providing assistance to the confocal image process ing. Mass spectrometry data were collected and analyzed in the University of Cincinnati Proteomics Laboratory under the direction of Ken Greis, PhD, on instrumentation supported by an NIH high end instrumentation grant (S10OD026717 01). We thank Ms. Jessica Webster and the Integrated Pa thology Research Core from CCHMC for their support with EM sample prep aration and processing. This work was supported by CCRF Endowed Scholar Award and R01HL166283 (M. Gu). N.M.P received the American Heart Association Pre Doctoral Fellowship grant 1013861 and the Albert J. Ryan Fellowship. Z.Y. received the American Heart Association Pre Doctoral Fellowship grant 906513. T.T. received the Falk Transformational Awards Program and NIH DP2 grant DK128799 01. R.J.R. received Human Disease Model Award of the Erasmus MC. D.N.K. received NHLBI/NIH grants N01 75N92020C00005 and R01HL095993. Y.S.Z. received funding support from the Brigham Research Institute of the Brigham and Women's Hospital, United States; NHLBI/NIH grants R01HL153857 and R01HL166522; and NCI/NIH grant R01CA282451.

AUTHOR CONTRIBUTIONS

Y.M., N.M.P., and C.T. contributed equally to this work. Y.M., N.M.P., C.T., M. Guo, and M. Gu conceived and designed experiments. Y.M., Z.Y., M.S., D.O.

K., M. C.Y., and Y. W.C. optimized and generated organoids. C.J. performed the bioinformatic analysis supervised by M. Guo. C.T., N.S., and Y. W.C. performed *in vivo* organoid transplantation. K.I., D.O.K., V.P. G., D.I.S., and K.K. performed staining and imaging analysis. X.L., K.C.L., S.M., and Y.S.Z. constructed the lung scaffold. C. L.N. performed EM imaging and analysis. J.T., J.A.W., K.W.M., R.J.R., D.N.K., M.A.H., J.M.W., T.T., and A.M.Z. contributed to all necessary iPSC cell lines, animals, material, and intellectual discussions. Y.M., N.M.P., C.T., Z.Y., D.O.K., N.S., M. C.Y., Y. W.C., M. Guo, and M. Gu wrote the manuscript with the contributions from all other authors. Y.M., M. Guo, and M. Gu oversaw the project. All authors read and approved the manuscript.

DECLARATION OF INTERESTS

Cincinnati Children's Hospital Medical Center has filed patent applications regarding the protocols for generating vascularized gut tube organoids. Y.S.Z. consulted for Allevi by 3D Systems and sits on the scientific advisory board and holds options of Xellar, neither of which participated in or biased the work. The relevant interests are managed by the Brigham and Women's Hospital.

STAR★METHODS

Detailed methods are provided in the online version of this paper and include the following:

- KEY RESOURCES TABLE
- EXPERIMENTAL MODEL AND STUDY PARTICIPANT DETAILS
  - Human ESC/iPSC generation and maintenance
  - Animals
  - Human fetal tissue
- METHOD DETAILS
  - Generation of conventional and vascularized organoids
  - Transplantation of human lung, intestine, and colon organoids
  - Generation of organotypic endothelium in vessel organoid
  - EC isolation from iPSC vessel organoids and vascularized organoids
  - Measurement of transepithelial electrical resistance on iPSC derived lung and intestinal endothelium
  - The EC plasticity test
  - Lung scaffold fabrication and vascularized lung organoid re seeding
  - Flow cytometry analysis
  - Histology examination
  - Immunofluorescence staining
  - Quantitative reverse transcription PCR
  - Proteomics mass spectrometry analysis
  - Processing and analysis of 10x single cell RNA seq of vascularized human organoid
  - Spatial transcriptomic analysis of transplanted vascularized organoids
  - Processing and analysis of published datasets
- QUANTIFICATION AND STATISTICAL ANALYSIS

SUPPLEMENTAL INFORMATION

Supplemental information can be found online at https://doi.org/10.1016/j.cell.2025.05.041.

Received: January 8, 2024
Revised: January 25, 2025
Accepted: May 29, 2025
Published: June 30, 2025

REFERENCES

1. Cao, J., O'Day, D.R., Pliner, H.A., Kingsley, P.D., Deng, M., Daza, R.M., Zager, M.A., Aldinger, K.A., Blecher Gonen, R., Zhang, F., et al. (2020). A human cell atlas of fetal gene expression. Science *370*, eaba7721. https://doi.org/10.1126/science.aba7721.
2. Jones, C.R.C., Karkanias, J., Krasnow, M.A., Pisco, A.O., Quake, S. R., Salzman, J., Yosef, N., Bulthaup, B., Brown, P., et al. (2022). The Tabula Sapiens: A multiple organ, single cell transcriptomic atlas of humans. Science *376*, eabl4896. https://doi.org/10.1126/science.abl4896.
3. Red Horse, K., Crawford, Y., Shojaei, F., and Ferrara, N. (2007). Endothelium microenvironment interactions in the developing embryo and in the adult. Dev. Cell *12*, 181 194. https://doi.org/10.1016/j.devcel.2007.01.013.
4. Augustin, H.G., and Koh, G.Y. (2024). A systems view of the vascular endothelium in health and disease. Cell *187*, 4833 4858. https://doi.org/10.1016/j.cell.2024.07.012.
5. Loe, A.K.H., Rao Bhatia, A., Kim, J.E., and Kim, T.H. (2021). Mesenchymal Niches for Digestive Organ Development, Homeostasis, and Disease. Trends Cell Biol. *31*, 152 165. https://doi.org/10.1016/j.tcb.2020.11.010.
6. Sachs, P.C., Mollica, P.A., and Bruno, R.D. (2017). Tissue specific microenvironments: a key tool for tissue engineering and regenerative medicine. J. Biol. Eng. *11*, 34. https://doi.org/10.1186/s13036 017 0077 0.
7. Paşca, S.P. (2019). Assembling human brain organoids. Science *363*, 126 127. https://doi.org/10.1126/science.aau5729.
8. Eicher, A.K., Kechele, D.O., Sundaram, N., Berns, H.M., Poling, H.M., Haines, L.E., Sanchez, J.G., Kishimoto, K., Krishnamurthy, M., Han, L., et al. (2022). Functional human gastrointestinal organoids can be engineered from three primary germ layers derived separately from pluripotent stem cells. Cell Stem Cell *29*, 36 51.e6. https://doi.org/10.1016/j.stem.2021.10.010.
9. Takebe, T., Sekine, K., Enomura, M., Koike, H., Kimura, M., Ogaeri, T., Zhang, R.R., Ueno, Y., Zheng, Y.W., Koike, N., et al. (2013). Vascularized and functional human liver from an iPSC derived organ bud transplant. Nature *499*, 481 484. https://doi.org/10.1038/nature12271.
10. Kim, H.J., Kim, G., Chi, K.Y., Kim, H., Jang, Y.J., Jo, S., Lee, J., Lee, Y., Woo, D.H., Han, C., et al. (2023). Generation of multilineage liver organoids with luminal vasculature and bile ducts from human pluripotent stem cells via modulation of Notch signaling. Stem Cell Res. Ther. *14*, 19. https://doi.org/10.1186/s13287 023 03235 5.
11. Sun, X.Y., Ju, X.C., Li, Y., Zeng, P.M., Wu, J., Zhou, Y.Y., Shen, L.B., Dong, J., Chen, Y.J., and Luo, Z.G. (2022). Generation of vascularized brain organoids to study neurovascular interactions. eLife *11*, e76707. https://doi.org/10.7554/eLife.76707.
12. Shaji, M., Tamada, A., Fujimoto, K., Muguruma, K., Karsten, S.L., and Yokokawa, R. (2024). Deciphering potential vascularization factors of on chip co cultured hiPSC derived cerebral organoids. Lab Chip *24*, 680 696. https://doi.org/10.1039/d3lc00930k.
13. Holloway, E.M., Wu, J.H., Czerwinski, M., Sweet, C.W., Wu, A., Tsai, Y.H., Huang, S., Stoddard, A.E., Capeling, M.M., Glass, I., et al. (2020). Differentiation of Human Intestinal Organoids with Endogenous Vascular Endothelial Cells. Dev. Cell *54*, 516 528.e7. https://doi.org/10.1016/j.devcel.2020.07.023.
14. Childs, C.J., Poling, H.M., Chen, K., Tsai, Y. H., Wu, A., Sweet, C.W., Vallie, A., Eiken, M.K., Huang, S., Schreiner, R., et al. (2023). Coordinated differentiation of human intestinal organoids with functional enteric neurons and vasculature. Cell Stem Cell *32*, 640 651.e9. https://doi.org/10.1016/j.stem.2025.02.007.
15. Miller, A.J., Dye, B.R., Ferrer Torres, D., Hill, D.R., Overeem, A.W., Shea, L.D., and Spence, J.R. (2019). Generation of lung organoids from human pluripotent stem cells in vitro. Nat. Protoc. *14*, 518 540. https://doi.org/10.1038/s41596 018 0104 8.
16. Dye, B.R., Hill, D.R., Ferguson, M.A.H., Tsai, Y.H., Nagy, M.S., Dyal, R., Wells, J.M., Mayhew, C.N., Nattiv, R., Klein, O.D., et al. (2015). In vitro generation of human pluripotent stem cell derived lung organoids. eLife *4*, e05098. https://doi.org/10.7554/eLife.05098.

17. Chen, Y.W., Huang, S.X., de Carvalho, A.L.R.T., Ho, S.H., Islam, M.N., Volpi, S., Notarangelo, L.D., Ciancanelli, M., Casanova, J.L., Bhatta charya, J., et al. (2017). A three dimensional model of human lung devel opment and disease from pluripotent stem cells. Nat. Cell Biol. *19*, 542 549. https://doi.org/10.1038/ncb3510.

18. Jacob, A., Morley, M., Hawkins, F., McCauley, K.B., Jean, J.C., Heins, H., Na, C.L., Weaver, T.E., Vedaie, M., Hurley, K., et al. (2017). Differentiation of Human Pluripotent Stem Cells into Functional Lung Alveolar Epithelial Cells. Cell Stem Cell *21*, 472 488.e10. https://doi.org/10.1016/j.stem. 2017.08.014.

19. Loh, K.M., Ang, L.T., Zhang, J., Kumar, V., Ang, J., Auyeong, J.Q., Lee, K. L., Choo, S.H., Lim, C.Y.Y., Nichane, M., et al. (2014). Efficient endoderm induction from human pluripotent stem cells by logically directing signals controlling lineage bifurcations. Cell Stem Cell *14*, 237 252. https://doi. org/10.1016/j.stem.2013.12.007.

20. Zorn, A.M., and Wells, J.M. (2009). Vertebrate endoderm development and organ formation. Annu. Rev. Cell Dev. Biol. *25*, 221 251. https://doi. org/10.1146/annurev.cellbio.042308.113344.

21. Múnera, J.O., Sundaram, N., Rankin, S.A., Hill, D., Watson, C., Mahe, M., Vallance, J.E., Shroyer, N.F., Sinagoga, K.L., Zarzoso Lacoste, A., et al. (2017). Differentiation of Human Pluripotent Stem Cells into Colonic Orga noids via Transient Activation of BMP Signaling. Cell Stem Cell *21*, 51 64. e6. https://doi.org/10.1016/j.stem.2017.05.020.

22. McCracken, K.W., Howell, J.C., Wells, J.M., and Spence, J.R. (2011). Generating human intestinal tissue from pluripotent stem cells in vitro. Nat. Protoc. *6*, 1920 1928. https://doi.org/10.1038/nprot.2011.410.

23. Brindle, N.P.J., Saharinen, P., and Alitalo, K. (2006). Signaling and func tions of angiopoietin 1 in vascular protection. Circ. Res. *98*, 1014 1023. https://doi.org/10.1161/01.RES.0000218275.54089.12.

24. Múnera, J.O., Kechele, D.O., Bouffi, C., Qu, N., Jing, R., Maity, P., Enri quez, J.R., Han, L., Campbell, I., Mahe, M.M., et al. (2023). Development of functional resident macrophages in human pluripotent stem cell derived colonic organoids and human fetal colon. Cell Stem Cell *30*, 1434 1451.e9. https://doi.org/10.1016/j.stem.2023.10.002.

25. Loh, K.M., Chen, A., Koh, P.W., Deng, T.Z., Sinha, R., Tsai, J.M., Barkal, A.A., Shen, K.Y., Jain, R., Morganti, R.M., et al. (2016). Mapping the Pair wise Choices Leading from Pluripotency to Human Bone, Heart, and Other Mesoderm Cell Types. Cell *166*, 451 467. https://doi.org/10.1016/j.cell. 2016.06.011.

26. Ng, W.H., Johnston, E.K., Tan, J.J., Bliley, J.M., Feinberg, A.W., Stolz, D.B., Sun, M., Wijesekara, P., Hawkins, F., Kotton, D.N., et al. (2022). Recapitulating human cardio pulmonary co development using simulta neous multilineage differentiation of pluripotent stem cells. eLife *11*, e67872. https://doi.org/10.7554/eLife.67872.

27. Silva, A.C., Matthys, O.B., Joy, D.A., Kauss, M.A., Natarajan, V., Lai, M.H., Turaga, D., Blair, A.P., Alexanian, M., Bruneau, B.G., et al. (2021). Co emergence of cardiac and gut tissues promotes cardiomyocyte matura tion within human iPSC derived organoids. Cell Stem Cell *28*, 2137 2152.e6. https://doi.org/10.1016/j.stem.2021.11.007.

28. Tyser, R.C.V., Mahammadov, E., Nakanoh, S., Vallier, L., Scialdone, A., and Srinivas, S. (2021). Single cell transcriptomic characterization of a gastrulating human embryo. Nature *600*, 285 289. https://doi.org/10. 1038/s41586 021 04158 y.

29. He, P., Lim, K., Sun, D., Pett, J.P., Jeng, Q., Polanski, K., Dong, Z., Bolt, L., Richardson, L., Mamanova, L., et al. (2022). A human fetal lung cell atlas uncovers proximal distal gradients of differentiation and key regulators of epithelial fates. Cell *185*, 4841 4860.e25. https://doi.org/10.1016/j. cell.2022.11.005.

30. Cifarelli, V., and Eichmann, A. (2019). The Intestinal Lymphatic System: Functions and Metabolic Implications. Cell. Mol. Gastroenterol. Hepatol. *7*, 503 513. https://doi.org/10.1016/j.jcmgh.2018.12.002.

31. Hein, R.F.C., Conchola, A.S., Fine, A.S., Xiao, Z., Frum, T., Brastrom, L.K., Akinwale, M.A., Childs, C.J., Tsai, Y.H., Holloway, E.M., et al. (2022). Sta ble iPSC derived NKX2 1+ lung bud tip progenitor organoids give rise to airway and alveolar cell types. Development *149*, dev200693. https:// doi.org/10.1242/dev.200693.

32. Yu, Q., Kilik, U., Holloway, E.M., Tsai, Y.H., Harmel, C., Wu, A., Wu, J.H., Czerwinski, M., Childs, C.J., He, Z., et al. (2021). Charting human develop ment using a multi endodermal organ atlas and organoid models. Cell *184*, 3281 3298.e22. https://doi.org/10.1016/j.cell.2021.04.028.

33. Gillich, A., Zhang, F., Farmer, C.G., Travaglini, K.J., Tan, S.Y., Gu, M., Zhou, B., Feinstein, J.A., Krasnow, M.A., and Metzger, R.J. (2020). Capil lary cell type specialization in the alveolus. Nature *586*, 785 789. https:// doi.org/10.1038/s41586 020 2822 7.

34. Burgess, C.L., Huang, J., Bawa, P., Alysandratos, K.D., Minakin, K., Mor ley, M.P., Babu, A., Villacorta Martin, C., Hinds, A., Thapa, B.R., et al. (2023). Generation of human alveolar epithelial type I cells from pluripotent stem cells. Preprint at bioRxiv. https://doi.org/10.1101/2023.01.19. 524655.

35. Srinivasan, B., Kolli, A.R., Esch, M.B., Abaci, H.E., Shuler, M.L., and Hick man, J.J. (2015). TEER measurement techniques for in vitro barrier model systems. J. Lab. Autom. *20*, 107 126. https://doi.org/10.1177/ 2211068214561025.

36. Neuhaus, W., Samwer, F., Kunzmann, S., Muellenbach, R.M., Wirth, M., Speer, C.P., Roewer, N., and Förster, C.Y. (2012). Lung endothelial cells strengthen, but brain endothelial cells weaken barrier properties of a hu man alveolar epithelium cell culture model. Differentiation *84*, 294 304. https://doi.org/10.1016/j.diff.2012.08.006.

37. Müller Redetzky, H.C., Suttorp, N., and Witzenrath, M. (2014). Dynamics of pulmonary endothelial barrier function in acute inflammation: mecha nisms and therapeutic perspectives. Cell Tissue Res. *355*, 657 673. https://doi.org/10.1007/s00441 014 1821 0.

38. Vancamelbeke, M., and Vermeire, S. (2017). The intestinal barrier: a funda mental role in health and disease. Expert Rev. Gastroenterol. Hepatol. *11*, 821 834. https://doi.org/10.1080/17474124.2017.1343143.

39. Sedgwick, J.B., Menon, I., Gern, J.E., and Busse, W.W. (2002). Effects of inflammatory cytokines on the permeability of human lung microvascular endothelial cell monolayers and differential eosinophil transmigration. J. Allergy Clin. Immunol. *110*, 752 756. https://doi.org/10.1067/mai. 2002.128581.

40. Man, S., Ubogu, E.E., Williams, K.A., Tucky, B., Callahan, M.K., and Ran sohoff, R.M. (2008). Human brain microvascular endothelial cells and um bilical vein endothelial cells differentially facilitate leukocyte recruitment and utilize chemokines for T cell migration. Clin. Dev. Immunol. *2008*, 384982. https://doi.org/10.1155/2008/384982.

41. Shu, W., Jiang, Y.Q., Lu, M.M., and Morrisey, E.E. (2002). Wnt7b regulates mesenchymal proliferation and vascular development in the lung. Devel opment *129*, 4831 4842. https://doi.org/10.1242/dev.129.20.4831.

42. Goss, A.M., Tian, Y., Tsukiyama, T., Cohen, E.D., Zhou, D., Lu, M.M., Ya maguchi, T.P., and Morrisey, E.E. (2009). Wnt2/2b and beta catenin signaling are necessary and sufficient to specify lung progenitors in the foregut. Dev. Cell *17*, 290 298. https://doi.org/10.1016/j.devcel.2009. 06.005.

43. Akeson, A.L., Greenberg, J.M., Cameron, J.E., Thompson, F.Y., Brooks, S.K., Wiginton, D., and Whitsett, J.A. (2003). Temporal and spatial regula tion of VEGF A controls vascular patterning in the embryonic lung. Dev. Biol. *264*, 443 455. https://doi.org/10.1016/j.ydbio.2003.09.004.

44. Vila Ellis, L., Cain, M.P., Hutchison, V., Flodby, P., Crandall, E.D., Borok, Z., Zhou, B., Ostrin, E.J., Wythe, J.D., and Chen, J. (2020). Epithelial Vegfa Specifies a Distinct Endothelial Population in the Mouse Lung. Dev. Cell *52*, 617 630.e6. https://doi.org/10.1016/j.devcel.2020.01.009.

45. Hagberg, C., Mehlem, A., Falkevall, A., Muhl, L., and Eriksson, U. (2013). Endothelial fatty acid transport: role of vascular endothelial growth factor B. Physiology (Bethesda) *28*, 125 134. https://doi.org/10.1152/physiol. 00042.2012.

46. Wimmer, R.A., Leopoldi, A., Aichinger, M., Wick, N., Hantusch, B., No vatchkova, M., Taubenschmid, J., Hämmerle, M., Esk, C., Bagley, J.A.,

et al. (2019). Human blood vessel organoids as a model of diabetic vascul opathy. Nature *565*, 505 510. https://doi.org/10.1038/s41586 018 0858 8.

47. Nikolova, M.T., He, Z., Wimmer, R.A., Seimiya, M., Nikoloff, J.M., Pen ninger, J.M., Camp, J.G., and Treutlein, B. (2025). Fate and state transi tions during human blood vessel organoid development. Published online April 16, 2025. Cell. https://doi.org/10.1101/2022.03.23.485329.
48. Nowotschin, S., Setty, M., Kuo, Y.Y., Liu, V., Garg, V., Sharma, R., Simon, C.S., Saiz, N., Gardner, R., Boutet, S.C., et al. (2019). The emergent land scape of the mouse gut endoderm at single cell resolution. Nature *569*, 361 367. https://doi.org/10.1038/s41586 019 1127 1.
49. Han, L., Chaturvedi, P., Kishimoto, K., Koike, H., Nasr, T., Iwasawa, K., Giesbrecht, K., Witcher, P.C., Eicher, A., Haines, L., et al. (2020). Single cell transcriptomics identifies a signaling network coordinating endoderm and mesoderm diversification during foregut organogenesis. Nat. Com mun. *11*, 4158. https://doi.org/10.1038/s41467 020 17968 x.
50. Zhang, W., Menke, D.B., Jiang, M., Chen, H., Warburton, D., Turcatel, G., Lu, C.H., Xu, W., Luo, Y., and Shi, W. (2013). Spatial temporal targeting of lung specific mesenchyme by a Tbx4 enhancer. BMC Biol. *11*, 111. https://doi.org/10.1186/1741 7007 11 111.
51. Watson, C.L., Mahe, M.M., Múnera, J., Howell, J.C., Sundaram, N., Poling, H.M., Schweitzer, J.I., Vallance, J.E., Mayhew, C.N., Sun, Y., et al. (2014). An in vivo model of human small intestine using pluripotent stem cells. Nat. Med. *20*, 1310 1314. https://doi.org/10.1038/nm.3737.
52. Niethamer, T.K., Stabler, C.T., Leach, J.P., Zepp, J.A., Morley, M.P., Babu, A., Zhou, S., and Morrisey, E.E. (2020). Defining the role of pulmonary endothelial cell heterogeneity in the response to acute lung injury. eLife *9*, e53072. https://doi.org/10.7554/eLife.53072.
53. Stickels, R.R., Murray, E., Kumar, P., Li, J., Marshall, J.L., Di Bella, D.J., Arlotta, P., Macosko, E.Z., and Chen, F. (2021). Highly sensitive spatial transcriptomics at near cellular resolution with Slide seqV2. Nat. Bio technol. *39*, 313 319. https://doi.org/10.1038/s41587 020 0739 1.
54. Choi, J., Park, J.E., Tsagkogeorga, G., Yanagita, M., Koo, B.K., Han, N., and Lee, J.H. (2020). Inflammatory Signals Induce AT2 Cell Derived Dam age Associated Transient Progenitors that Mediate Alveolar Regenera tion. Cell Stem Cell *27*, 366 382.e7. https://doi.org/10.1016/j.stem.2020. 06.020.
55. Kobayashi, Y., Tata, A., Konkimalla, A., Katsura, H., Lee, R.F., Ou, J., Ba novich, N.E., Kropski, J.A., and Tata, P.R. (2020). Persistence of a regen eration associated, transitional alveolar epithelial cell state in pulmonary fibrosis. Nat. Cell Biol. *22*, 934 946. https://doi.org/10.1038/s41556 020 0542 8.
56. Strunz, M., Simon, L.M., Ansari, M., Kathiriya, J.J., Angelidis, I., Mayr, C.H., Tsidiridis, G., Lange, M., Mattner, L.F., Yee, M., et al. (2020). Alveolar regeneration through a Krt8+ transitional stem cell state that persists in hu man lung fibrosis. Nat. Commun. *11*, 3559. https://doi.org/10.1038/ s41467 020 17358 3.
57. Basil, M.C., Cardenas Diaz, F.L., Kathiriya, J.J., Morley, M.P., Carl, J., Brumwell, A.N., Katzen, J., Slovik, K.J., Babu, A., Zhou, S., et al. (2022). Human distal airways contain a multipotent secretory cell that can regen erate alveoli. Nature *604*, 120 126. https://doi.org/10.1038/s41586 022 04552 0.
58. Kadur Lakshminarasimha Murthy, P., Sontake, V., Tata, A., Kobayashi, Y., Macadlo, L., Okuda, K., Conchola, A.S., Nakano, S., Gregory, S., Miller, L.A., et al. (2022). Human distal lung maps and lineage hierarchies reveal a bipotent progenitor. Nature *604*, 111 119. https://doi.org/10.1038/ s41586 022 04541 3.
59. Sountoulidis, A., Marco Salas, S., Braun, E., Avenel, C., Bergenstråhle, J., Theelke, J., Vicari, M., Czarnewski, P., Liontos, A., Abalo, X., et al. (2023). A topographic atlas defines developmental origins of cell heterogeneity in the human embryonic lung. Nat. Cell Biol. *25*, 351 365. https://doi.org/ 10.1038/s41556 022 01064 x.
60. Huang, D., Liu, T., Liao, J., Maharjan, S., Xie, X., Pérez, M., Anaya, I., Wang, S., Tirado Mayer, A., Kang, Z., et al. (2021). Reversed engineered human alveolar lung on a chip model. Proc. Natl. Acad. Sci. USA *118*, e2016146118. https://doi.org/10.1073/pnas.2016146118.
61. Gong, J., Schuurmans, C.C.L., Genderen, A.M.V., Cao, X., Li, W., Cheng, F., He, J.J., López, A., Huerta, V., Manríquez, J., et al. (2020). Complexa tion induced resolution enhancement of 3D printed hydrogel constructs. Nat. Commun. *11*, 1267. https://doi.org/10.1038/s41467 020 14997 4.
62. Becker, B.F., Chappell, D., Bruegger, D., Annecke, T., and Jacob, M. (2010). Therapeutic strategies targeting the endothelial glycocalyx: acute deficits, but great potential. Cardiovasc. Res. *87*, 300 310. https://doi. org/10.1093/cvr/cvq137.
63. Desai, T.J., Brownfield, D.G., and Krasnow, M.A. (2014). Alveolar progen itor and stem cells in lung development, renewal and cancer. Nature *507*, 190 194. https://doi.org/10.1038/nature12930.
64. Treutlein, B., Brownfield, D.G., Wu, A.R., Neff, N.F., Mantalas, G.L., Espi noza, F.H., Desai, T.J., Krasnow, M.A., and Quake, S.R. (2014). Recon structing lineage hierarchies of the distal lung epithelium using single cell RNA seq. Nature *509*, 371 375. https://doi.org/10.1038/nature13173.
65. Brownfield, D.G., de Arce, A.D., Ghelfi, E., Gillich, A., Desai, T.J., and Kras now, M.A. (2022). Alveolar cell fate selection and lifelong maintenance of AT2 cells by FGF signaling. Nat. Commun. *13*, 7137. https://doi.org/10. 1038/s41467 022 34059 1.
66. Pradhan, A., Che, L., Ustiyan, V., Reza, A.A., Pek, N.M., Zhang, Y., Alber, A.B., Kalin, T.R., Wambach, J.A., Gu, M., et al. (2023). Novel FOXF1 Stabilizing Compound TanFe Stimulates Lung Angiogenesis in Alveolar Capillary Dysplasia. Am. J. Respir. Crit. Care Med. *207*, 1042 1054. https://doi.org/10.1164/rccm.202207 1332OC.
67. Slot, E., de Klein, A., and Rottier, R.J. (2020). Generation of three iPSC lines from two patients with heterozygous FOXF1 mutations associated to Alveolar Capillary Dysplasia with Misalignment of the Pulmonary Veins. Stem Cell Res. *44*, 101745. https://doi.org/10.1016/j.scr.2020.101745.
68. Jumper, J., Evans, R., Pritzel, A., Green, T., Figurnov, M., Ronneberger, O., Tunyasuvunakool, K., Bates, R., Zídek, A., Potapenko, A., et al. (2021). Highly accurate protein structure prediction with AlphaFold. Nature *596*, 583 589. https://doi.org/10.1038/s41586 021 03819 2.
69. Varadi, M., Anyango, S., Deshpande, M., Nair, S., Natassia, C., Yorda nova, G., Yuan, D., Stroe, O., Wood, G., Laydon, A., et al. (2022). Alpha Fold Protein Structure Database: massively expanding the structural coverage of protein sequence space with high accuracy models. Nucleic Acids Res. *50*, D439 D444. https://doi.org/10.1093/nar/gkab1061.
70. Edel, G.G., van Kempen, M., Munck, A.B., Huisman, C.N., Naalden, C.A. P., Brouwer, R.W.W., Koornneef, S., van IJcken, W.F.J., Wijnen, R.M.H., and Rottier, R.J. (2024). The molecular consequences of FOXF1 missense mutations associated with alveolar capillary dysplasia with misalignment of pulmonary veins. J. Biomed. Sci. *31*, 100. https://doi.org/10.1186/ s12929 024 01088 5.
71. Guo, M., Wikenheiser Brokamp, K.A., Kitzmiller, J.A., Jiang, C., Wang, G., Wang, A., Preissl, S., Hou, X., Buchanan, J., Karolak, J.A., et al. (2023). Single Cell Multiomics Identifies Cells and Genetic Networks Underlying Alveolar Capillary Dysplasia. Am. J. Respir. Crit. Care Med. *208*, 709 725. https://doi.org/10.1164/rccm.202210 2015OC.
72. Wang, G., Wen, B., Deng, Z., Zhang, Y., Kolesnichenko, O.A., Ustiyan, V., Pradhan, A., Kalin, T.V., and Kalinichenko, V.V. (2022). Endothelial progen itor cells stimulate neonatal lung angiogenesis through FOXF1 mediated activation of BMP9/ACVRL1 signaling. Nat. Commun. *13*, 2080. https:// doi.org/10.1038/s41467 022 29746 y.
73. Szafranski, P., Gambin, T., Dharmadhikari, A.V., Akdemir, K.C., Jhangiani, S.N., Schuette, J., Godiwala, N., Yatsenko, S.A., Sebastian, J., Madan Khetarpal, S., et al. (2016). Pathogenetics of alveolar capillary dysplasia with misalignment of pulmonary veins. Hum. Genet. *135*, 569 586. https://doi.org/10.1007/s00439 016 1655 9.
74. Isaza Restrepo, A., Martin Saavedra, J.S., Velez Leal, J.L., Vargas Bar ato, F., and Riveros Dueñas, R. (2018). The Peritoneum: Beyond the Tis sue A Review. Front. Physiol. *9*, 738. https://doi.org/10.3389/fphys. 2018.00738.

75. Wilm, B., Ipenberg, A., Hastie, N.D., Burch, J.B.E., and Bader, D.M. (2005). The serosal mesothelium is a major source of smooth muscle cells of the gut vasculature. Development *132*, 5317 5328. https://doi.org/10.1242/dev.02141.

76. Fedorchak, N.J., Iyer, N., and Ashton, R.S. (2021). Bioengineering tissue morphogenesis and function in human neural organoids. Semin. Cell Dev. Biol. *111*, 52 59. https://doi.org/10.1016/j.semcdb.2020.05.025.

77. Homan, K.A., Gupta, N., Kroll, K.T., Kolesky, D.B., Skylar Scott, M., Miyoshi, T., Mau, D., Valerius, M.T., Ferrante, T., Bonventre, J.V., et al. (2019). Flow enhanced vascularization and maturation of kidney organo ids in vitro. Nat. Methods *16*, 255 262. https://doi.org/10.1038/s41592 019 0325 y.

78. Mahaddalkar, P.U., Scheibner, K., Pfluger, S., Ansarullah, Sterr, M., Beck enbauer, J., Irmler, M., Beckers, J., Knobel, S., and Lickert, H. (2020). Gen eration of pancreatic beta cells from CD177+ anterior definitive endoderm. Nat. Biotechnol. *38*, 1061 1072. https://doi.org/10.1038/s41587 020 0492 5.

79. Lickert, H., Kispert, A., Kutsch, S., and Kemler, R. (2001). Expression pat terns of Wnt genes in mouse gut development. Mech. Dev. *105*, 181 184. https://doi.org/10.1016/s0925 4773(01)00390 2.

80. Alto, L.T., and Terman, J.R. (2017). Semaphorins and their Signaling Mechanisms. Methods Mol. Biol. *1493*, 1 25. https://doi.org/10.1007/978 1 4939 6448 2 1.

81. Suhrie, K., Pajor, N.M., Ahlfeld, S.K., Dawson, D.B., Dufendach, K.R., Kitz miller, J.A., Leino, D., Lombardo, R.C., Smolarek, T.A., Rathbun, P.A., et al. (2019). Neonatal Lung Disease Associated with TBX4 Mutations. J. Pediatr. *206*, 286 292.e1. https://doi.org/10.1016/j.jpeds.2018.10.018.

82. Pijuan Sala, B., Griffiths, J.A., Guibentif, C., Hiscock, T.W., Jawaid, W., Calero Nieto, F.J., Mulas, C., Ibarra Soria, X., Tyser, R.C.V., Ho, D.L.L., et al. (2019). A single cell molecular map of mouse gastrulation and early organogenesis. Nature *566*, 490 495. https://doi.org/10.1038/s41586 019 0933 9.

83. Tchieu, J., Zimmer, B., Fattahi, F., Amin, S., Zeltner, N., Chen, S., and Studer, L. (2017). A Modular Platform for Differentiation of Human PSCs into All Major Ectodermal Lineages. Cell Stem Cell *21*, 399 410.e7. https://doi.org/10.1016/j.stem.2017.08.015.

84. Efremova, M., Vento Tormo, M., Teichmann, S.A., and Vento Tormo, R. (2020). CellPhoneDB: inferring cell cell communication from combined expression of multi subunit ligand receptor complexes. Nat. Protoc. *15*, 1484 1506. https://doi.org/10.1038/s41596 020 0292 x.

85. Hao, Y., Hao, S., Andersen Nissen, E., Mauck, W.M., 3rd, Zheng, S., But ler, A., Lee, M.J., Wilk, A.J., Darby, C., Zager, M., et al. (2021). Integrated analysis of multimodal single cell data. Cell *184*, 3573 3587.e29. https://doi.org/10.1016/j.cell.2021.04.048.

86. Traag, V.A., Waltman, L., and van Eck, N.J. (2019). From Louvain to Leiden: guaranteeing well connected communities. Sci. Rep. *9*, 5233. https://doi.org/10.1038/s41598 019 41695 z.

87. Korsunsky, I., Millard, N., Fan, J., Slowikowski, K., Zhang, F., Wei, K., Ba glaenko, Y., Brenner, M., Loh, P.R., and Raychaudhuri, S. (2019). Fast, sensitive and accurate integration of single cell data with Harmony. Nat. Methods *16*, 1289 1296. https://doi.org/10.1038/s41592 019 0619 0.

88. La Manno, G., Soldatov, R., Zeisel, A., Braun, E., Hochgerner, H., Petu khov, V., Lidschreiber, K., Kastriti, M.E., Lönnerberg, P., Furlan, A., et al. (2018). RNA velocity of single cells. Nature *560*, 494 498. https://doi.org/10.1038/s41586 018 0414 6.

89. Bergen, V., Lange, M., Peidli, S., Wolf, F.A., and Theis, F.J. (2020). Gener alizing RNA velocity to transient cell states through dynamical modeling. Nat. Biotechnol. *38*, 1408 1414. https://doi.org/10.1038/s41587 020 0591 3.

90. Jin, S., Guerrero Juarez, C.F., Zhang, L., Chang, I., Ramos, R., Kuan, C.H., Myung, P., Plikus, M.V., and Nie, Q. (2021). Inference and analysis of cell cell communication using CellChat. Nat. Commun. *12*, 1088. https://doi.org/10.1038/s41467 021 21246 9.

91. Aran, D., Looney, A.P., Liu, L., Wu, E., Fong, V., Hsu, A., Chak, S., Naikawadi, R.P., Wolters, P.J., Abate, A.R., et al. (2019). Reference based analysis of lung single cell sequencing reveals a transitional profibrotic macrophage. Nat. Immunol. *20*, 163 172. https://doi.org/10.1038/s41590 018 0276 y.

92. Rodrigues Toste de Carvalho, A.L., Liu, H.Y., Chen, Y.W., Porotto, M., Moscona, A., and Snoeck, H.W. (2021). The in vitro multilineage differen tiation and maturation of lung and airway cells from human pluripotent stem cell derived lung progenitors in 3D. Nat. Protoc. *16*, 1802 1829. https://doi.org/10.1038/s41596 020 00476 z.

93. Mahe, M.M., Brown, N.E., Poling, H.M., and Helmrath, M.A. (2017). In Vivo Model of Small Intestine. Methods Mol. Biol. *1597*, 229 245. https://doi.org/10.1007/978 1 4939 6949 4 17.

94. Poling, H.M., Wu, D., Brown, N., Baker, M., Hausfeld, T.A., Huynh, N., Chaffron, S., Dunn, J.C.Y., Hogan, S.P., Wells, J.M., et al. (2018). Mechan ically induced development and maturation of human intestinal organoids in vivo. Nat. Biomed. Eng. *2*, 429 442. https://doi.org/10.1038/s41551 018 0243 9.

95. Gillich, A., St.Julien, K.R., Brownfield, D.G., Travaglini, K.J., Metzger, R.J., and Krasnow, M. (2021). Alveoli form directly by budding led by a single epithelial cell. Preprint at bioRxiv. https://doi.org/10.1101/2021.12.25.474174.

96. He, H., Bell, S.M., Davis, A.K., Zhao, S., Sridharan, A., Na, C.L., Guo, M., Xu, Y., Snowball, J., Swarr, D.T., et al. (2024). PRDM3/16 regulate chro matin accessibility required for NKX2 1 mediated alveolar epithelial differ entiation and function. Nat. Commun. *15*, 8112. https://doi.org/10.1038/s41467 024 52154 3.

97. Gu, M., Shao, N.Y., Sa, S., Li, D., Termglinchan, V., Ameen, M., Karakikes, I., Sosa, G., Grubert, F., Lee, J., et al. (2017). Patient Specific iPSC Derived Endothelial Cells Uncover Pathways that Protect against Pulmo nary Hypertension in BMPR2 Mutation Carriers. Cell Stem Cell *20*, 490 504.e5. https://doi.org/10.1016/j.stem.2016.08.019.

98. Bennett, J., Ishikawa, C., Agarwal, P., Yeung, J., Sampson, A., Uible, E., Vick, E., Bolanos, L.C., Hueneman, K., Wunderlich, M., et al. (2023). Pa ralog specific signaling by IRAK1/4 maintains MyD88 independent func tions in MDS/AML. Blood *142*, 989 1007. https://doi.org/10.1182/blood.2022018718.

99. Liu, J., Manabe, H., Qian, W., Wang, Y., Gu, Y., Chu, A.K.Y., Gadhvi, G., Song, Y., Ono, N., and Welch, J.D. (2024). CytoSignal detects locations and dynamics of Ligand Receptor signaling at cellular resolution from spatial transcriptomic data. Preprint at bioRxiv. https://doi.org/10.1101/2024.03.08.584153.

STAR★METHODS

KEY RESOURCES TABLE

REAGENT or RESOURCE	SOURCE	IDENTIFIER
Antibodies		
Rabbit monoclonal anti FOXA2	Abcam	Cat# AB108422; RRID: AB 11157157
Goat polyclonal anti FOXA2	R&D	Cat# AF2400; RRID: AB 2294104
Goat polyclonal anti HAND1	R&D	Cat# AF3168; RRID: AB 2115853
Mouse monoclonal anti SOX2	Santa Cruz	Cat# SC 365823; RRID: AB 10842165
Rabbit monoclonal anti FOXF1	Abcam	Cat# ab168383; RRID: AB 3676395
Goat polyclonal anti FOXF1	R&D	Cat# AF4798;RRID: AB 2105588
Rabbit monoclonal anti CDX2	Cell Marque	Cat# 235R 15; RRID: AB 1516799
Rabbit monoclonal anti GATA4	Cell Signaling Technology	Cat# 36966; RRID: AB 2799108
Mouse monoclonal anti NKX2.1	Abcam	Cat# ab72876; RRID: AB 1271363
Rabbit monoclonal anti NKX2.1	Abcam	Cat# ab76013; RRID: AB 1310784
Sheep polyclonal anti PECAM1	R&D	Cat# AF806; RRID: AB 355617
Rat monoclonal anti CD31	BD Biosciences	Cat#: 553370; RRID: AB 394816
Rabbit monoclonal anti SATB2	Cell Marque	Cat# 384R 15; RRID: AB 2917998
Mouse monoclonal anti HTI 56	Terrace Biotech	Cat# TB 29AHT1 56; RRID: AB 2847898
Mouse monoclonal anti HTII 280	Terrace Biotech	Cat# TB 27AHT2 280; RRID: AB 2832931
Goat polyclonal anti SOX9	Millipore	Cat# AB5535; RRID: AB 2239761
Mouse monoclonal anti CDH17	R&D	Cat# MAB1032;RRID: AB 2077388
Mouse monoclonal anti KRT14	Abcam	Cat# ab7800;RRID: AB 306091
Rabbit monoclonal anti E Cadherin	Cell Signaling Technology	Cat# 3195;RRID: AB 2291471
Goat polyclonal anti E Cadherin	R&D	Cat# AF648;RRID: AB 355504
Mouse monoclonal anti TP63	Biocare Medical	Cat# cm163C;RRID: AB 10588476
Mouse monoclonal anti MUC5AC	Abcam	Cat# ab3649; RRID: AB 2146844
Rabbit polyclonal anti MUC5B	Sigma	Cat# HPA008246; RRID: AB 1854203
Rabbit polyclonal anti SCGB1A1	LifeSpan Biosciences	Cat# LS B6822;RRID: AB 11139649
Mouse monoclonal anti SCGB3A2	Enzo Life Sciences	Cat# H00117156 M01; RRID:AB 1507242
Mouse monoclonal anti TUBA4A	Sigma	Cat# T7451; RRID: AB 609894
Mouse monoclonal anti ACTA2	Sigma	Cat# A2547; RRID: AB 476701
Goat polyclonal anti DPPIV	R&D	Cat# AF954; RRID: AB 355739
Rabbit polyclonal anti TUBB3	Abcam	Cat# 18207; RRID: AB 444319
Rabbit monoclonal anti MUC2	Abcam	Cat# ab134119; RRID: AB 2889298
Mouse monoclonal anti CHGA	DSHB	Cat# CPTC CHGA 1; RRID: AB 1553436
Rabbit polyclonal anti LYZ	DAKO	Cat# A0099; RRID: AB 2341230
Guinea pig polyclonal anti SPC	Seven Hills Bioreagents	Cat# GP992
Rabbit polyclonal anti HOPX	Abclonal	Cat# A15537; RRID: AB 2762938
Rabbit monoclonal anti Ku 80	Cell Signaling Technology	Cat# 2180; RRID: AB 2218736
Goat polyclonal anti PROX1	R&D	Cat# AF2727; RRID: AB 2170716
Rabbit monoclonal anti WT1	Abcam	Cat# ab89901; RRID: AB 2043201
Rabbit monoclonal anti PDGFRb	Cell Signaling Technology	Cat# 3169; RRID: AB 2162497
Rabbit monoclonal anti ERG	Abcam	Cat# ab92513, RRID:AB 2630401
Rabbit polyclonal anti GFP	Thermo Fisher Scientific	Cat# A 11122, RRID:AB 221569
Mouse monoclonal anti CD117 PE (c KIT)	BioLegend	Cat# 983304; RRID: AB 2650654
Mouse monoclonal anti CD187 APC (CXCR4)	BioLegend	Cat# 306510; RRID: AB 314616
Mouse monoclonal anti CD326 APC (EpCAM)	BioLegend	Cat# 324208; RRID: AB 756081

(*Continued on next page*)

Continued

REAGENT or RESOURCE	SOURCE	IDENTIFIER
Human CD144 (VE Cadherin) MicroBeads	Miltenyi Biotec	Cat# 130 097 857
Donkey anti Mouse IgG (H+L) Alexa Fluor 647	Jackson ImmunoResearch Labs	Cat# 715 606 150; RRID: AB 2340865
Donkey anti Rabbit IgG (H+L) Alexa Fluor 647	Jackson ImmunoResearch Labs	Cat# 711 606 152; RRID: AB 2340625
Donkey anti Goat IgG (H+L) Alexa Fluor 647	Jackson ImmunoResearch Labs	Cat# 705 606 147; RRID: AB 2340438
Donkey anti Sheep IgG (H+L) Alexa Fluor 647	Jackson ImmunoResearch Labs	Cat# 713 606 147; RRID: AB 2340752
Donkey anti Guinea pig IgG (H+L) Alexa Fluor 647	Jackson ImmunoResearch Labs	Cat# 706 605 148; RRID: AB 2340476
Donkey anti Goat IgG (H+L) Alexa Fluor 488	Jackson ImmunoResearch Labs	Cat# 705 545 147; RRID: AB 2336933
Donkey anti Sheep IgG (H+L) Alexa Fluor 488	Jackson ImmunoResearch Labs	Cat# 713 545 147; RRID: AB 2340745
Donkey anti Mouse IgG (H+L) Alexa Fluor 488	Thermo Fisher Scientific	Cat# A21202; RRID: AB 141607
Donkey anti Goat IgG (H+L) Alexa Fluor 488	Thermo Fisher Scientific	Cat# A 11055; RRID: AB 2534102
Donkey anti Rabbit IgG (H+L) Alexa Fluor 488	Thermo Fisher Scientific	Cat# A 21206; RRID: AB 2535792
Donkey anti Sheep IgG (H+L) Alexa Fluor 594	Jackson ImmunoResearch Labs	Cat# 713 585 147; RRID: AB 2340748
Donkey anti Mouse IgG (H+L) Alexa Fluor 594	Molecular Probes	Cat# A 21203; RRID: AB 141633
Donkey anti Sheep IgG (H+L) Alexa Fluor 594	Thermo Fisher Scientific	Cat# A11016; RRID: AB 10562537
Donkey anti Goat IgG (H+L) Alexa Fluor 594	Thermo Fisher Scientific	Cat# A 11058; RRID: AB 2534105
Donkey anti Rabbit IgG (H+L) Alexa Fluor 594	Thermo Fisher Scientific	Cat# R37119; RRID: AB 2556547
Donkey anti Mouse IgG (H+L) Alexa Fluor 546	Thermo Fisher Scientific	Cat# A10037; RRID: AB 2534012
Donkey anti Goat IgG (H+L) Alexa Fluor 568	Thermo Fisher Scientific	Cat# A11057; RRID: AB 2534104
Peroxidase conjugated Goat ant Rat secondary antibody	Jackson ImmunoResearch Labs	Cat# 112 035 167; RRID: AB 2338139
Biological samples		
Fetal human tissues	Discover Together Biobank at Cincinnati Children's Research Foundation	https://www.cincinnatichildrens.org/service/c/clinical trials/biobank/investigators
Chemicals, peptides, and recombinant proteins		
KnockOut DMEM/F12	Gibco	12660012
KnockOut serum replacement	Gibco	10828028
GlutaMAX Supplement	Gibco	35050061
Antibiotic Antimycotic	Gibco	15240062
DMEM/F12	Gibco	11320033
RPMI 1640	Gibco	11875093
Neurobasal Medium	Gibco	21103049
B 27 Supplement	Gibco	17504044
N 2 Supplement	Gibco	17502048
1M HEPEs	Gibco	15630080
7.5% NaHCO3	Gibco	25080094
Ham's F 12	Gibco	11765054
IMDM medium	Gibco	12440053
Advanced DMEM/F12	Gibco	12634010
StemPro™ 34 SFM	Gibco	10639011
Fetal bovine serum (FBS)	Gibco	26 140 079
0.05% Trypsin EDTA	Gibco	25300054
TrypLE Express Enzyme	Gibco	12605010
Accutase	STEMCELL Technologies	07920
Collagen Type I Solution	Millipore Sigma	C8919 20ML
0.5mM UltraPure EDTA	Invitrogen	15575020
Defined fetal bovine serum (FBS)	Hyclone	SH30070.02
Cultrex SCQ	R&D	3434 010 02
StemMACS iPSC brew XF culture medium	Miltenyi Biotec	130 104 368

(*Continued on next page*)

Continued

REAGENT or RESOURCE	SOURCE	IDENTIFIER
BSA Stock Solution	Miltenyi Biotec	130 091 376
MEM Non Essential Amino Acid Solution (NEAA)	STEMCELL Technologies	07600
β Mercaptoethanol	Millipore Sigma	M3148
Monothioglycerol	Millipore Sigma	M6145
1N NaOH	Millipore Sigma	S2770
Dulbecco's Modified Eagle's Medium/DMEM	Millipore Sigma	D5648 10L
PureCol Collagen I	Advanced Biomatrix	5005
Matrigel	Corning	356255
Y 27632	Tocris	1254
PIK90	Tocris	7902
SB 431542	Tocris	S1067
SAG	Tocris	4366
All trans Retinoic acid (ATRA)	Tocris	0695
Human BMP4	R&D	314 BP
Human Noggin	R&D	6057 NG
Human FGF7	R&D	251 KG CF
Human ANG1	R&D	923 AN CF
Human WNT11	R&D	6179 WN CF
Human SEMA3C	R&D	5570 S3 050
Human SEMA6B	R&D	2094 S6 050
Human SEMA6A	R&D	1146 S6 025
Human BMP2	R&D	355 BM CF
L ascorbic acid	R&D	4055
IWP2	R&D	3533
Human ANGPTL4	R&D	4487 AN 050
Human GDF15	R&D	957 GD CF
Human FGF4	Shenandoah	100 31
Activin A	Shenandoah	800 01
Human EGF	Shenandoah	100 26
CHIR99021	Selleck Chem	S2924
Human FGF10	Peprotech	AF 100 26
Human FGF 154 basic (FGF2)	GeimiBio	300 113P
Human VEGF A	GeminiBio	300 827P
LATS IN 1	Cayman	36623
R spondin 1 (5%)	CCHMC PSCF Core	N/A
Forskolin	Millipore Sigma	F3917
Dexamethasone	Millipore Sigma	D4902
8 Bromoadenosine 3',5' cyclic monophosphate sodium salt (cAMP)	Millipore Sigma	B7880
3 Isobutyl 1 methylxanthine (IBMX)	Millipore Sigma	I5879
Human WNT2B	Origene	TP762265
Human WNT4	Origene	TP761294
Human TGFB1	InvivoGen	rcyc htgfb1
Anti Adherence solution	STEMCELL Technologies	07010
Cell Recovery Solution	Corning	354253
Liberase™ TH	Roche	5401151001
Dispase	Gibco	17105041
DNase I	GoldBio	D 301 500
Paraformaldehyde Solution, 4% in PBS (PFA)	Thermo Scientific	AAJ61899AP

(*Continued on next page*)

Continued

REAGENT or RESOURCE	SOURCE	IDENTIFIER
ProLong™ Gold Antifade Mountant with DNA Stain DAPI	Thermo Scientific	P36931
Sucrose	Millipore Sigma	S0389
10% Neutral buffered formalin	Millipore Sigma	1004965000
Triton X 100 solution	Millipore Sigma	93443 100ML
Tween 20	Millipore Sigma	P7949 500ML
Benzyl Alcohol	Millipore Sigma	402834
Benzyl Benzoate	Millipore Sigma	B6630
4',6 Diamidino 2 phenylindole dihydrochloride (DAPI)	Millipore Sigma	D9542
Opal 520	Akoya Biosciences	FP1487001KT
Opal 570	Akoya Biosciences	FP1488001KT
Opal 690	Akoya Biosciences	FP1497001KT
Tyramide reagents: TSA PLUS CYANINE 5	Akoya Biosciences	NEL745001KT
Donkey serum	Jackson ImmunoResearch Labs	017 000 121
Sodium deoxycholate solution (10%)	Bioworld	40430018 1
4 12% B T gel	Invitrogen	NP0321BOX
Isoflurane	Butler Schein Animal Health	029405
Buprenex	Midwest Veterinary Supply	RXBUPRENOR5 V
Gluture Topical Tissue Adhesive	Abbott Laboratories	503763
SYBR green master mix	Applied Biosystems	A25742
Tissue Tek O.C.T. Compound	SAKURA	4583
Alginate	Millipore Sigma	W201502
Porcine skin gelatin	Millipore Sigma	G2500
Methacrylate anhydride	Millipore Sigma	276685
Hyaluronic Acid	HAworks	HA 1500k
Dimethylformamide	Millipore Sigma	D4551
PDMS	Dow Corning	1317318
Photoinitiator LAP	Millipore Sigma	900889
mTG	Millipore Sigma	SAE0159
Embed 812 resin	Electron Microscopy Sciences	14900
Critical commercial assays		
EnVision®+ Dual Link System HRP (DAB+)	DAKO	K4065
RNAscope™ Multiplex Fluorescent V2 Assay for smFISH	ACD	323110
RNA extraction kit	Zymo Research	R1055
High Capacity cDNA Reverse Transcription Kit	Applied Biosystems	43 688 14
Chromium Next GEM Single Cell 3' RNA seq (v3.1)	10x Genomics	1000268
10X10 Curio Seeker Bundle Kit	Curio	SK003
Deposited data		
Raw and analyzed scRNA seq dataset on organoids	This paper	GEO: GSE250399
Raw dataset for proteomics	This paper	PRIDE: https://doi.org/10.6019/PXD048316
tvHLuO Spatial Transcriptomic Curio data	This paper	GEO: GSE296429
scRNA seq dataset of CS7 human embryo	Tyser et al.[28]	http://www.human gastrula.net/
scRNA seq dataset of E6.5 8.5 mouse embryo	Pijuan Sala et al.[82]	https://github.com/MarioniLab/EmbryoTimecourse2018
scRNA seq dataset of E8.75 mouse anterior and posterior gut data	Nowotschin et al.[48]	https://endoderm explorer.com/
scRNA seq dataset of E8.75 mouse anterior gut data	Han et al.[49]	GEO: GSE136689; GSE136687

(*Continued on next page*)

Continued

REAGENT or RESOURCE	SOURCE	IDENTIFIER
scRNA seq of conventional human lung organoids	Hein et al.[31]	ArrayExpress: E MTAB 11953
scRNA seq of human intestinal organoids	Holloway et al.[13]	ArrayExpress: E MTAB 9228
scRNA seq dataset of fetal human lung tissues	He et al.[29]	https://fetal lung.cellgeni.sanger.ac.uk/
scRNA seq dataset of developing human endodermal organs	Yu et al.[32]	https://doi.org/10.17632/x53tts3zfr.1
scRNA seq dataset of Tabula Sapiens atlas	Tabula Sapiens et al.[2]	https://figshare.com/projects/Tabula Sapiens/100973
Original code for scRNA seq analysis	This paper	GitHub: https://github.com/MZGuo lab/Vascularized human organoids
Experimental models: Cell lines		
Control 1 human iPSC line NKX2.1 GFP and SFTPC tdTomato knock in reporter	Boston University CReM iPSC Bank[18]	BU3 NGST line; https://stemcellbank.bu.edu/Catalog/Item/Details/509
Control 2 human iPSC line	California Institute of Regenerative Medicine (CIRM) iPSC Repository	CW60359E clone line;
Control 3 human iPSC line	This paper.	N/A
Control 4 Human hESC H9 GFP line	MSKCC stem cell core facility and Tchieu et al.[83]	N/A
Control 5 Human iPSC72 3 GFP line	CCHMC Pluripotent Stem Cell Facility[8]	RRID: CVCL C7HE
Control 6 Human iPSC line (clone 7B2) NKX2.1 EGFP and TP63 mCherry reporter line	Cystic Fibrosis Foundation[31]	N/A
ACD 1 human iPSC line	Boston University CReM iPSC Bank[66]	FOXF1.1 iPSC line; https://stemcellbank.bu.edu/Catalog/Item/Details/751
ACD 2 and ACD3 human iPSC line	Erasmus University Medical Center Rotterdam[67]	https://hpscreg.eu/cell line/EMCi127 A;https://hpscreg.eu/cell line/EMCi128 A;
Experimental models: Organisms/strains		
Mouse: NOD SCID IL 2Rγnull (NSG)	The Jackson Laboratory	RRID: IMSR JAX:005557
Mouse: C57BL/6J	The Jackson Laboratory	RRIS: IMSR JAX:000664
Oligonucleotides		
Probes for smFISH	This paper	See Table S4B
Primers for qPCR	This paper	See Table S4C
Software and algorithms		
10x Genomics Cell Ranger, v6.1.2	10x Genomics Inc.	https://www.10xgenomics.com/support/software/cell ranger/downloads#download links
Cytosignal v0.2.0	Liu et al.; doi: https://doi.org/10.1101/2024.03.08.584153	https://github.com/welch lab/cytosignal
CellphoneDB v2	Efremova et al.[84]	https://github.com/Teichlab/cellphonedb
R studio, v4.1.0	N/A	https://cran.r project.org/bin/windows/base/old/4.1.0/
Python 3	N/A	https://www.python.org/download/releases/3.0/
Seurat, v4.2.0, v5	Hao et al.[85]	https://github.com/satijalab/seurat/releases/tag/v4.2.0
Leiden algorithm	Traag et al.[86]	https://doi.org/10.1038/s41598 019 41695 z
Harmony, v0.1.0	Korsunsky et al.[87]	https://github.com/immunogenomics/harmony

(*Continued on next page*)

Continued

REAGENT or RESOURCE	SOURCE	IDENTIFIER
velocyto, v0.17.16	La Manno et al.[88]	https://velocyto.org/
scVelo, v0.2.4	Bergen et al.[89]	https://scvelo.readthedocs.io/en/stable/
CellChat, v1.4.0	Jin et al.[90]	https://github.com/sqjin/CellChat
SingleR, v1.6.1	Aran et al.[91]	https://github.com/dviraran/SingleR
R package pheatmap, v1.0.12	Raivo Kolde	https://cran.r project.org/web/packages/pheatmap/index.html
Xcalibur 4.3 software	Thermo Scientific	Cat# OPTON 30965
Proteome discoverer version 3.0	Thermo Scientific	Cat# B51001472
Morpheus	Broad Institute	https://software.broadinstitute.org/morpheus
ImageJ (2.3.0/1.53f)	NIH	https://imagej.net/ij/index.html
Imaris version 9.8/9.9	Oxford Instrument	https://imaris.oxinst.com/
GraphPad Prism, v8.0	GraphPad Software, LLC	https://www.graphpad.com/features
FlowJo, v10.8.0	FlowJo, LLC	https://www.flowjo.com/solutions/flowjo/downloads
Other		
Flowmi	Bel Art SP Scienceware	H13680 0040
AggreWell 400	STEMCELL Technologies	34415
Ultralow attachment 6 well plate	Corning	3471
Extreme environment orbital shaker	OHAUS	SHEX1619DG
Trans well insert, 0.4um	Millipore Sigma	CLS3470 48EA
LS Columns	Miltenyi Biotec	130 042 401
ClinoStar stress free 3D culture system	CelVivo	10004 12
EVOM™ Epithelial Volt/Ohm (TEER) Meter 3	World Precision Instruments	EVOM3
Bio Imaging and Analysis Facility	Cincinnati Children's Hospital Medical Center	RRID: SCR 022628
Stainless steel needle nozzle, 30G	CELLINK	NZ5300505001
Syring pump	SKE Research Equipment	S EF SP
Dialysis membrane	Thermo Scientific	08 667E
3D printer	ELEGOO	Mars 4 Ultra
UV crosslink irradiator	OmniCure	S1500 Pro
Leica UC7 ultramicrotome	Leica Microsystems Inc	NA
Hitachi H 7800 transmission electron microscope	Hitachi High Tech USA	NA

EXPERIMENTAL MODEL AND STUDY PARTICIPANT DETAILS

Human ESC/iPSC generation and maintenance

All experiments involving the generation and differentiation of human PSC lines were performed with the approval of the Institutional Review Board (IRB) of Cincinnati Children's Hospital Medical Center (CCHMC), Boston University, and the Daily Board of the Medical Ethics Committee (METC) Erasmus University Medical Center Rotterdam, The Netherlands. Control-1 iPSC line (BU3 NGST iPSC line, male, 32-year-old), carrying NKX2.1-GFP and SFTPC-tdTomato reporters, was obtained from prior studies as described.[18] The control-2 iPSC line, purchased from the California Institute of Regenerative Medicine (CIRM) iPSC Repository, is derived from fibroblasts from a female donor of one-year-old. Control-3 iPSC line was derived in-house by using 20-month female donor's fibroblasts obtained from Biorepository for Investigation of Neonatal Diseases of the Lung (BRINDL). Control-4 H9-hESC line[83] and Control-5 iPSC line[8] were engineered with GFP knock-in.[83] Control-6 iPSC line carried NKX2.1-EGFP and TP63-mCherry reporters.[31] ACD-1 iPSC line, also known as 'FOXF1.1' iPSC line, was reprogrammed from fibroblasts from a newborn female donor at the Center for Regenerative Medicine, Boston University.[66] ACD-2 ('EMC127i-A:ACD871C4') and ACD-3 ('EMC128i-A:ACD874C9') iPSC lines were derived from fibroblasts from two newborn male donors at the Erasmus University Medical Center.[67] Fibroblast samples from healthy control and ACD patients were procured with documented informed consent (See Table S4A).[83] Human iPSCs and ESCs fed with StemMACS iPSC-brew XF culture medium were routinely cultured on the Cultrex-coated 6-well plate at 37°C and passaged with 0.5mM EDTA solution in PBS every 3-5 days. All human stem cells were routinely authenticated by testing the karyotype abnormality, short tandem repeat analysis, pluripotency marker expression, and mycoplasma contamination.

Animals

Immune-deficient NOD-SCID IL-2Rγnull (NSG) mice at the age of 8–16 weeks old were obtained from the Comprehensive Mouse and Cancer Core Facility at CCHMC or the Icahn School of Medicine at Mount Sinai and used in vascularized organoids and conventional HLuO, HIO, and HCO transplantation experiments. C57BL/6J wild-type mice were purchased from The Jackson Laboratory for mating the embryonic pups. Both male and female mice were used in the study and we did not observe any gender effect on the results. Littermates were randomly assigned to experimental groups. All experiments were performed with the approval of the Institutional Animal Care and Use Committee (IACUC) of CCHMC and the Icahn School of Medicine at Mount Sinai. NSG mice were kept on antibiotic chow (275 p.p.m. Sulfamethoxazole and 1,365 p.p.m. Trimethoprim, Test Diet). Wile-type animals were provided with normal chow. All mice were housed under 12 h/12 h day and night cycle with water and food *ad libitum*.

Human fetal tissue

De-identified human fetal tissues from gestational age 21-38 weeks were collected and requested through Discover Together Biobank at Cincinnati Children's Research Foundation (CCRF) under the approved IRB. No significant gender differences were observed in the current study. Healthy human subjects were not involved in the previous procedures and tested naïve for drug use.

METHOD DETAILS

Generation of conventional and vascularized organoids

Human pluripotent stem cells were first dissociated into single cells with 0.5mM EDTA and filtered by 40nm Flowmi to generate 3D Embryonic bodies (EBs) following the manufacturer's instruction: 1) EBs containing 500∼1000 cells per EB were made with AggreWell 400 in the Aggregation media including 50uM Y-27632. 2) After 24 hours of incubation (Day 0), EBs were formed, collected, and washed once with N2B27 basal media. 3) 1200 EBs can be evenly distributed into 3 wells of ultralow attachment 6-well plate containing 2-3ml medium and be gently shaken on the orbital shaker at 90rpm speed for subsequent differentiation.

Aggregation media consisted of: 50ml media included 40ml knockOut DMEM/F12, 10ml knockOut serum replacement, 0.5ml GlutaMAX, 0.5ml NEAA, 35μl 1:100 b-Mercaptoethanol in PBS, and 0.5ml Antibiotic-Antimycotic.

N2B27 basal media consisted of: 500ml media included 250ml DMEM/F12, 250ml Neurobasal medium, 10ml B27 supplement, 5ml N2 supplement, 2.5ml GlutaMAX, 350ul 1:100 b-Mercaptoethanol in PBS, and 5ml Antibiotic-Antimycotic.

Generation of vascularized lung organoid

Several lung organoid and vessel organoid differentiation protocols were scrutinized to establish the vascularized lung organoid platform.[13,15,17,18,46,92] 1) EBs were differentiated into meso-endodermal spheroid using 72 hours (Day 0-3) of Activin A (100ng/ml) in N2B27 basal medium. 2) 0%, 0.2%, and 2% of defined FBS were included on Day 0-1, Day1-2, and Day 2-3, respectively. 3) During Day 0-1, CHIR99021 and BMP4 (30ng/ml) were included. CHIR at 3uM, 6uM, 9uM, and 12 uM concentrations were tested to optimize the full differentiation. Prolonged treatment with CHIR99021 over 24 hours suppressed endoderm differentiation. In some cases, FGF2 (20ng/ml) or PI3K inhibitor (PIK90, 1uM) were tested for the first 24 hours.[25] 4) vAFG was subsequently generated by adding Noggin (100ng/ml) into N2B27 medium with 2% defined FBS for 96 hours (Day 3-7). 5) Media was changed daily from day 0 to day 7. CHIR (2uM), FGF4 (500ng/ml), SB-431542 (10uM), or SAG (1uM) were tested for vAGF induction efficiency from day 3-7. 6) On day 7, vAFG was collected and resuspended in 150ul Collagen-Matrigel mixture and transferred to 12-well transwell insert (0.4um) to solidify at 37°C incubator for 30 mins. 7) vAFG was incubated with lung specification media 1 from day 7-10 and then switched to lung specification media 2 from day 10-21 to generate vHLPO. 1ml culture media was added to the bottom chamber of the transwell to create an air-liquid interface (ALI) and changed every other day. 8) To generate distal vHLuO containing AT2 cells, vHLPO was exposed to the distal lung specification medium from day 21-28 under ALI. Medium was changed every other day. 9) Distal vHLuO can be further patterned into AT1 cell-enriched lung organoids using AT1-specification media for another 10 days[34] under ALI for medium change every other day.

Collagen solution consisted of: 0.1N NaOH, 750ul; 100x DMEM, 313ul; 1M HEPEs, 63ul; 7.5% $NaHCO_3$, 49ul; 100X GlutaMAX, 31ul; Ham's F-12, 460ul; 3mg/ml PureCol Collagen I, 3.33ml.

Collagen-matrigel mixture solution consisted of: Three portions of collagen solution with one portion of Matrigel.

Lung specification media 1 consisted of: 100nM ATRA, 10ng/ml BMP4, 3uM CHIR, 10ng/ml FGF7; 10ng/ml FGF10; 100ng/ml VEGFA; 100ng/ml ANG1 in N2B27 basal media.

Lung specification media 2 consisted of: 100nM ATRA, 3uM CHIR, 10ng/ml FGF7, 10ng/ml FGF10, 100ng/ml VEGFA, 100ng/ml ANG1 in N2B27 media.

Distal lung specification media consisted of: 3uM CHIR, 10ng/ml FGF7, 10ng/ml FGF10, 50nM Dexamethasone, 0.1mM cAMP, 0.1mM IBMX, 100ng/ml VEGFA, 100ng/ml ANG1 in N2B27 media.

AT1-specification media consisted of: 10ng/ml FGF10, 10uM LATS-IN-1, 50nM Dexamethasone, 0.1mM cAMP, 0.1mM IBMX, 100ng/ml VEGFA, 100ng/ml ANG1 in N2B27 media)[34]

Generation of vascularized small intestine and colon organoid

Similar to generating vascularized lung organoids, 1) EBs were exposed to 100ng/ml Activin A (Day 0-3) and 12uM CHIR (Day 0-1), while BMP4 (30ng/ml) was added for 72 hours (Day 0-3) in N2B27 media. 2) 0%, 0.2%, and 2% of defined FBS were included on Day

0-1, Day1-2, and Day 2-3, respectively. 3) vMHG organoids were generated after 96 hours of CHIR (2uM), FGF4 (500ng/ml), and VEGFA (100ng/ml). Media was changed daily. 4) On day 7, vMHG was embedded in the same matrix as vHLPO on the transwell insert to create ALI. Spheroids were patterned in EGF (100 ng/mL), Noggin (100ng/ml), R-spondin-1 (5%), VEGFA (100ng/ml), and ANG1 (100ng/ml) for vHIOs or EGF (100ng/ml), BMP2 (100 ng/mL), VEGFA (100ng/ml), and ANG1 (100ng/ml) for vHCOs for 72 hours (Day 7-10). Media was changed every other day. 5) Both vHIOs and vHCOs were maintained in EGF (100ng/ml), VEGFA (100ng/ml), and ANG1 (100ng/ml) from day 10 to day 35. Media was changed every other day.

Generation of conventional human lung, intestine, and colon organoids

The generation of conventional lung organoids was performed based on previous studies.[17,92] 1) hPSC differentiation into endoderm was performed in serum-free differentiation (SFD) medium. 2) hPSCs were treated with 0.05% Trypsin and plated onto low-attachment 6-well plates, and then resuspended in embryoid bodies formation medium. 3) After 12-16 h, embryoid bodies formation medium was changed into endoderm induction medium for 74.5–79.5 hour. 4) On day 4.1 or 4.3, check endoderm yield by flow cytometric analysis of CXCR4 and c-kit expression. If the endoderm yield is >90%, continue the anteriorization step. 5) The endoderm bodies were dissociated into single cells using 0.05% trypsin and plated onto fibronectin-coated, 6-well tissue culture plates ($\sim$7.5x10^5 cells per well). 6) For induction of anterior foregut endoderm, the endoderm cells were cultured in SFD medium supplemented with 100 ng/mL Noggin and 10 uM SB431542 for 24 hour, then switched for 24 hours to 10 uM SB431542 and 1 uM IWP2 treatment in normoxic incubator. 7) At the end of anterior foregut endoderm induction, cells were treated with ventralization media (branching media) for 48 hour and three-dimensional clump formation was observed. 8) The clumps were then suspended by gently pipetting around the wells and plated onto low-attachment plates. The suspended clumps are called lung bud organoids (LBOs) hereafter. 9) LBOs were fed every other day until day 20–day 25 in branching media. 10) The day 20–day 25 LBOs were embedded in 100% Matrigel in 24-well Transwell inserts and incubated in branching media in a normoxic incubator.

SFD media consisted of: IMDM supplemented with 25% Ham's F12, 1xN2 supplement, 1xB27 supplement, 50 ug/ml ascorbic acid, 2 mM GlutaMAX, 0.4 uM monothioglycerol and 0.056% BSA at 37 °C in a 5% CO2/5% O2.

Embryoid bodies formation media consisted of: SFD medium containing 10 uM Y-27632, and 3 ng/ml human BMP4.

Endoderm induction media consisted of: SFD medium containing 10 uM Y-27632, 0.5 ng/ml human BMP4, 2.5 ng/ml human FGF2, and 100 ng/ml human activin A.

Ventralization/branching media consisted of: SFD media containing 3 uM CHIR99021, 10 ng/ml human FGF10, 10 ng/ml human KGF, 10 ng/ml human BMP4 and 50 nM ATRA.

The directed differentiation of HIOs and HCOs were previously published.[21,22] Briefly, pluripotent stem cells were differentiated into definitive endoderm using 72 hours of Activin A (100 ng/mL) in RPMI 1640 supplemented with NEAA and increasing concentrations of defined FBS (0%, 0.2%, 2%). Spontaneous 3D mid/hindgut spheroids were generated after 96 hours of CHIR (3 uM) and FGF4 (500 ng/mL). Media was changed daily. After embedding in basement membrane Matrigel, spheroids were patterned in EGF (100 ng/mL) for HIOs or EGF and BMP2 (100 ng/mL) for HCOs for 72 hours. Both HIOs and HCOs were then maintained in Advanced DMEM/F12 supplemented with 1xN2 supplement, 1xB27 supplement, HEPES, 1X Antibiotic-Antimycotic, 1X GlutaMAX and EGF (100ng/ml) from day 10 to day 35.

Transplantation of human lung, intestine, and colon organoids

NSG mice were kept on antibiotic chow (275 p.p.m. Sulfamethoxazole and 1,365 p.p.m. Trimethoprim, Test Diet). Food and water were provided *ad libitum* before and after surgeries. A single conventional HIO, HCO, vHLuO, vHIO, or vHCO matured *in vitro* for 35 days, was removed from Matrigel and transplanted under the kidney capsule as previously described.[51,93,94] For the conventional HLuO transplantation, one million day 20-day 25 LBO cells were combined with 5ul of Matrigel prior to surgical implantation under the kidney capsule. Briefly, the mice were anesthetized with 2% inhaled isoflurane, and the left side of the mouse was then prepped in sterile fashion with isopropyl alcohol and povidine-iodine. A small left-posterior subcostal incision was made to expose the kidney. A subcapsular pocket was created and the organoid was then placed into the pocket. The kidney was then returned to the peritoneal cavity and the mice were given an intraperitoneal (IP) flush of Zosyn (100 mg/kg.). The skin was closed in a double layer and the mice were given a subcutaneous injection with Buprenex (0.05 mg/kg). At 8-15 weeks following engraftment, the mice were then humanely euthanized and the resulting grafts were analyzed.

Generation of organotypic endothelium in vessel organoid

iPSC-vessel organoids (VOs) were generated based on a protocol described by Wimmer et al.[46] with some modifications. iPSCs were first dissociated into single cells and resuspended in Aggregation media. 1.2x10^6 cells were added to each well of the Aggrewell™400 that were prepped with Anti-Adherence solution per manufacturer's instructions. The Aggrewell™400 consisting of cells was then spun down at 100g for 3 mins to evenly distribute cells into each microwell (1000 cells per microwell). Cells were then left to form EBs overnight at 37°C. The next day, EBs were transferred to N2B27 media supplemented with 12μM CHIR99021 and 30ng/ml BMP4 and cultured on an orbital shaker for three days. Subsequently, the media was changed to N2B27 supplemented with 2μM Forskolin and 100ng/ml VEGFA-165 for two days. Then from days 5-15, the aggregates were further differentiated and cultured in Blood Vessel Induction (BVI) media consisting of StemPro™-34 SFM media supplemented with StemPro™-34 nutrient mix, 1X GlutaMAX, 1X Antibiotic-Antimycotic, 15% Fetal Bovine Serum (FBS), 100ng/ml VEGFA-165, and FGF2. For ligand-treated conditions, the appropriate concentrations of ligands were added to fresh BVI media and fresh BVI media was replaced every two

days until the end of 15 days of differentiation. WNT2B: 50ng/ml; WNT11: 200ng/ml; SEMA3C: 200ng/ml; SEMA6B: 100ng/ml; SEMA6A: 200ng/ml; WNT4: 50ng/ml; ANGPTL4: 1ug/ml; TGFB1: 5-10ng/ml; GDF15: 10-20ng/ml.

EC isolation from iPSC-vessel organoids and vascularized organoids

Day 15 iPSC-VOs were pooled together and dissociated into single cells via enzymatic digestion. A cocktail of 0.5mg/ml Liberase™ TH, 5mg/ml Dispase in DPBS were utilized. The reaction was then incubated at 37°C for 20-30 mins. After the first 5 mins, 60U/ml DNase I was added to the reaction and organoids were broken down by pipetting using a wide bore tip every 5 mins thereafter. After single cells were obtained, the digestion reaction was quenched using cold KnockOut DMEM/F12 supplemented with 10% FBS. Cells were spun down at 300g for 5 mins and resuspended into MACS® buffer consisting of 0.5% MACS® BSA Stock Solution and 2mM EDTA in DPBS. The cells were passed through a 40μm filter to ensure single cells were obtained. CD144-expressing ECs were then isolated using the human CD144 (VE-Cadherin) MicroBeads and LS Columns according to manufacturer's instructions. RNA was extracted from treated and untreated ECs per manufacturer's recommendations (Zymo Research) and analyzed by qPCR.

iPSC-vascularized organoids were differentiated and populated in Clinostar stress-free 3D organoid culture incubator. Around 2000 Day-7 vascularized foregut or mid/hindgut organoids were pooled and differentiated in one ClinoReactor till day 21 without embedding in the extracellular matrix. The medium was changed every two days. At day 21, the vascularized organoids were dissociated at 37°C with 1X Accutase Enzyme supplemented with 60U/ml DNase I for 20∼30 mins. The reaction was quenched with DMEM/F12 supplemented with 10% FBS and filtered through 70um cell strainer to generate the single-cell suspension. ECs were then purified using the human CD144 (VE-Cadherin) and human CD31 Microbeads and LS Columns according to the manufacturer's instructions.

Measurement of transepithelial electrical resistance on iPSC-derived lung and intestinal endothelium

3∼5x10^5 purified ECs from Day-21 vascularized organoids were seeded on the collagen I (0.01%)-coated 24-well transwell insert. To maintain the endothelial organotypic identity until they reach confluent, the BVI medium (StemPro™-34 SFM media supplemented with StemPro™-34 nutrient mix, 1X GlutaMAX, 1X Antibiotic-Antimycotic, 15% FBS, 100ng/ml VEGFA-165, and 100ng/ml FGF2) was supplemented with either SEMA3C (200ng/ml), WNT2B (50ng/ml), SEMA6A (100ng/ml), SEMA6B (200ng/ml), and WNT11 (100ng/ml) for lung EC or WNT4 (100ng/ml), GDF15 (10ng/ml), ANGPTL4 (1ug/ml), and TGFB1 (5ng/ml) for intestinal EC. After the EC grew into confluent, the probes of the volt ohmmeter were sterilized with ethanol and then dipped in the medium. Readings from 3 different locations in each well were taken, including the blank well. To calculate the transepithelial electrical resistance (TEER), we take the difference between the mean sample reading and the mean blank reading and then multiply the number by the area of the transwell (0.33 cm^2 for 6.5mm 24-well inserts).

The EC plasticity test

3∼5x10^5 purified ECs from Day-21 vascularized organoids were seeded on the collagen I (0.01%)-coated 24-well transwell insert and then cultured in BVI for 48h. ECs isolated from vHLPOs were subsequently treated with a combination of small intestine/colon-EC-specifying ligands including 100ng/ml WNT4, 10ng/ml GDF15, 1ug/ml ANGPTL4, and 5ng/ml TGFB1. ECs isolated from vHIOs were treated with a combination of lung-EC-specifying ligands including 200ng/ml SEMA3C, 50ng/ml WNT2B, 100ng/ml SEMA6A, 200ng/ml SEMA6B, and 100ng/ml WNT11. Ligand treatment lasted for five days with fresh media (containing the respective ligands) changed every two days.

Lung scaffold fabrication and vascularized lung organoid re-seeding

The hydrogel-based lung scaffold with 5% GelMA and 0.1% HAMA was prepared following protocol.[60] A 2%(w/v) alginate solution and a 1.1% (w/v) calcium chloride solution were used for crosslinking. Alginate was dispensed through a 30G stainless-steel needle nozzle at 0.6 mL/h, positioned 20 cm above a calcium chloride bath. A voltage of 15 kV was applied between the nozzle and a grounded ring electrode (80 mm inner diameter), producing alginate droplets that formed crosslinked microbeads in the bath.

GelMA was synthesized by reacting porcine skin gelatin (Type A, ∼300 g bloom, Mw ∼90,000 Da) with methacrylic anhydride at 50°C for 2 hours in DPBS (pH7.4). Methacrylic anhydride was added dropwise at a 0.2:1 weight ratio to gelatin under vigorous stirring. The solution was diluted with preheated DPBS, dialyzed against deionized water at 40 °C for 6 days with dialysis membrane (12,000–14,000 Da cut-off), filtered through a 0.22μm syringe filter, and freeze-dried into a white solid for storage.

The synthesis of HAMA followed the procedure as previously described.[61] HAMA was synthesized by dissolving 4.0 g of HA (1,500 kDa, HA-1500k) in 200 mL of DI water at 4°C, followed by adding 133.3 mL of dimethylformamide and 7.88 mL of methacrylic anhydride under stirring. The pH was adjusted to 8–9, and the reaction proceeded at 4°C for 18 hours. After adding 0.5M NaCl, the mixture was precipitated in ethanol, producing HAMA as white pellets. The pellets were washed with ethanol, dissolved in DI water, and dialyzed for 5 days.

The polydimethylsiloxane (PDMS) chip was fabricated by casting a PDMS precursor (11:1 base-to-curing agent ratio) onto a 3D-printed mold and curing at 80°C overnight. The chip, featuring a central chamber (8×4×5 mm^3), was plasma-treated and bonded to a cover glass, sterilized in 75% ethanol for 12 hours, and rinsed with sterile water multiple times before use.

Alginate microbeads were packed into the PDMS chip's central chamber, and 50 μL of 5% GelMA/ 0.1% HAMA solution with 0.5% lithium phenyl-2,4,6,-trimethylbenzoylphosphinate (LAP) and 0.05% microbial transglutaminas (mTG) was applied, allowing diffusion between the microbeads without fully submerging the top layer. The structure was photocrosslinked under UV (~10 mW/cm^2, 360-480 nm) for 60s and incubated at 37°C for 2 h for mTG crosslinking. Alginate microbeads were removed with 0.01M EDTA at 37°C for 1 h, forming the 3D inverse opal structure. The structure was washed with DPBS and stored at 4°C until use.[60,61]

Day 21 vLPOs were dissociated into single cells and separated into lung ECs and non-ECs by PECAM1-based MACS sorting. Based on the reported alveolar cell composition,[95] EC and non-ECs were mixed at the ratio of 1:3 and seeded on the lung scaffold pre-coated with 0.01% collagen solution. After two hours of attachment, the distal lung specification medium was added to submerge the cell-containing lung scaffold for 14 days. The fresh medium was changed every two days before fixation for downstream imaging analysis.

Flow cytometry analysis

Day 3 and Day 7 spheroids/organoids were dissociated with 1X TrypLE Express Enzyme for 7~10 mins at 37°C. The reaction was vortexed every other minute and stopped by adding N2B27 media. Single-cell suspension was made by filtering the cells through 40um Flowmi. The following antibodies were used for staining: anti-CD117 (c-KIT)-PE (1:100 dilution), anti-CD184 (CXCR4)-APC (1:100 dilution), anti-CD326 (EpCAM)-APC (1:100 dilution). For cell-surface marker staining and analyses, cells were stained for 20 min at 4°C in FACS buffer consisting of 1X PBS with 0.5% bovine serum albumin and 2mM EDTA. Stained cells were analyzed using an LSR II Flow cytometer. Data were analyzed using FlowJo software (V10.8.0).

Histology examination

Transplanted organoids were freshly collected, fixed in 4% PFA in 1X PBS overnight, and processed for paraffin embedding (FFPE), sectioning, H&E staining, and histological analysis. For in vitro cultured organoids, the embedded organoids were fixed in 4% PFA for 2 hours, then washed three times with 1X PBS and immersed in 30% sucrose in PBS overnight at 4°C. Afterward, the organoids were immersed in 50/50 30% sucrose/OCT for 2h at room temperature and embedded in OCT.

Immunofluorescence staining

For FFPE embedded sample, the sections (5um) from organoids were deparaffinized and rehydrated with a series of alcohol solutions of decreasing concentrations (5 min in each solution, 100%, 95%, 70%, and 50%) and kept in PBS for 30 min and moved to antigen retrieval process. For OCT embedded sample, the section (7um) from organoids were washed in PBS for 5 min and then fixed in 10% Neutral buffered formalin (NBF) for 10 min. Slides were washed thrice for 5 min in PBS and then moved to antigen retrieval. Antigen retrieval was performed on sections immersed in citrate 10 mM in PBS, pH 6 and microwave heated (7 min once at 650 W and 5 min twice at 350 W). Sections were washed for 10 min in PBS and then incubated for 60 min at room temperature (RT) with blocking buffer (PBS containing 4% donkey serum and 0.1% Triton X-100). Then the sections were incubated with the primary antibodies diluted in blocking buffer at 4°C overnight. After three washes (5 min) in PBS, slides were incubated for 60 min at RT with secondary antibody diluted in blocking buffer. Slides were then washed three times for 5 min in PBS and mounted in aqueous mounting medium with DAPI. The first antibodies used are listed in key resources table.

Whole-mount immunofluorescence staining

The whole-mount staining procedure was modified following the previously published protocol.[46] Day 3 and Day 7 spheroids or organoids were collected in 15ml tube and fixed in 4% PFA at RT for one hour. The fixed samples were washed with 1X PBS and blocked with blocking buffer for 2 hours at RT (To make 50ml buffer, add 1.5ml FBS, 0.5g BSA, 250ul Triton X-100, 250ul Tween 20, and 500ul of 1% (weight/volume) sodium deoxycholate solution in 47.5ml 1X PBS). After removing the blocking buffer, 50ul of diluted first antibody solution was added overnight at 4°C. On the next day, the samples were washed three times for 15 mins with PBS-T (Tween-20, 0.05%) and incubated with fluorescent dye-conjugated secondary antibodies and DAPI at RT for two hours. After the secondary antibody reaction, the samples were washed three times with PBS-T and cleared with Benzyl Alcohol/ Benzyl Benzoate solution (BABB) for immediate imaging.

The whole-mount immunostaining of vasculature on Day 21 vascularized organoids, mouse embryonic lung, and small intestinal tissues was performed using the published protocol[33] with minor modifications. Tissues or organoids were fixed with 4% PFA at RT for two hours. Before staining, the tissues were dehydrated in 100% Methanol for 10 mins and incubated in 5% H_2O_2/Methanol for 5 hours at RT. Afterward, the tissues were washed with 100% Methanol and rehydrated through a methanol and PBS series into PBS-T. Tissues were blocked with the blocking buffer overnight at 4 °C and incubated with primary antibodies for two days at 4°C and secondary antibodies for one day. Mouse tissues were stained using a peroxidase-conjugated secondary antibody, and the signals were amplified in tyramide reagents for 45 mins. The stained tissues or organoids were cleared with EZ View solution (80% Nycodenz and 7 M urea) for immediate imaging. Rat Anti-mouse PECAM1 antibody (BD Bioscience, 1:2500) was used for vascular visualization purposes.

Immunohistochemistry staining

Sections were deparaffinized, rehydrated, and washed in PBS. Endogenous peroxidase activity was quenched with 0.3% hydrogen peroxide in methanol. Sections were preincubated with the appropriate donkey serum and then incubated with primary antibody overnight at 4 °C. The antibody used in this investigation was HOPX Rabbit pAb (1:100). The slides were treated with

streptavidin-biotin complex for 60 minutes at a dilution of 1:100. Immunoreactions were visualized using a 3,3′-diaminobenzidine (DAB) substrate-chromogen solution and counterstained with eosin. Sections were immersed in an ethanol and xylene bath and mounted for examination.

Single molecule fluorescence* in situ *hybridization (smFISH)

smFISH was performed using a proprietary high-sensitivity RNA amplification and detection technology, according to the manufacturer's instructions using the indicated proprietary probes, the RNAscope Multiplex Fluorescent Reagent Kit (v.2), and Opal dyes (1:500 dilution for Opal 570 and 690 dyes, 1:250 dilution for Opal 520). After smFISH, sections were mounted in aqueous mounting medium with DAPI. Proprietary (Advanced Cell Diagnostics) probes used were listed in Table S4B.

Transmission electron microscopy

Cultured lung organoids growing on the HAMA-substrate were fixed in situ with 3% glutaraldehyde in 0.15M sodium cacodylate buffer (SCB), pH 7.4, at 4°C overnight, followed by processing for transmission electron microscopy.[96] All the processing steps were conducted at room temperature unless specified otherwise. After fixation, they were incubated with 1% osmium tetroxide in 0.15M SCB, pH 7.4, for 1 hour at 4°C, followed by dehydration with a graded series of alcohols, infiltration, and polymerization with Embed 812 resin at 60°C. EM sections were cut using a Leica UC7ultramicrotome and stained with 2% aqueous uranyl acetate and Reynold's lead citrate. EM images were acquired using a Hitachi H-7800 transmission electron microscope and an AMT Biosprint 16 TEM CCD camera at 80 kV.

Quantitative reverse-transcription PCR

Our detailed protocol was previously described.[97] Briefly, total RNA was extracted, purified, and quantified for reverse transcription using High-Capacity RNA to cDNA Kit according to the manufacturer's instructions. qPCR was carried out using 5 ng cDNA and 6 mL SYBR green master mix. Primers were listed in Table S4C. Each measurement was performed in triplicate. Heatmaps for qPCR results were generated by Morpheus visualization tool. A relative color scheme uses the minimum and maximum values in each treatment to convert values to colors. N=3 in each treatment group.

Proteomics mass spectrometry analysis

The fluid from two 3-month tvHLuO was collected with a 5ml syringe, combined, and immediately snap-frozen before analysis. A 1-D silver stained (SS) gel was run on the samples to check the protein levels. For protein identification, a preparative gel using 20 ug of each sample was run into a 4-12% B-T gel using MOPS buffer with molecular weight marker lanes in between each sample just until all the protein entered the gel (about 2 cm total). The full section represented the 2 cm run in the wells, were excised, reduced with DTT, alkylated with IAA, and digested with trypsin overnight. The resulting peptides were extracted and dried in a SpeedVac concentrator, then resuspended in 0.1% Formic acid (FA). 0.5ug of each sample was analyzed by nano LC-MS/MS (Orbitrap Eclipse) with data recorded using Xcalibur 4.3 software. Full details of the LC-MS methodology were reported previously.[98] The resulting spectra were searched against a combined database of common proteomics contaminant proteins (e.g., trypsin, BSA, cytokeratins), and the UniProt mouse (UP000000589) and Human (UP000005640) database using Proteome discoverer version 3.0 with the Sequest HT search algorithm.

Processing and analysis of 10x single-cell RNA-seq of vascularized human organoid

Day-3 meso-endoderm spheroids (B0, B1, B2, and B3) and day-7 vascularized anterior foregut (vAFG-'B0' and vAFG-'B1') and mid/hindgut organoids (vMHG-'B1', vMHG-'B2', and vMHG-'B3') were dissociated with 1 X TrypLE Express Enzyme at 37°C for 7–12 mins. The reactions were stopped by adding N2B27 basal medium and centrifuged and filtered with 40um strainer. Day-21 vascularized gut tube organoids (vHLPO, vHIO, and vHCO) were embedded in a Collagen-Matrigel mixture, so were dissociated with a different digestion cocktail. Briefly, the organoids from one trans-well insert were immersed in 1ml Cell Recovery Solution at 4°C for 5 mins and triturated with P1000 wide-bore tip to break the matrix. The solution was centrifuged and resuspended in 1ml pre-warmed Dispase (5mg/ml)/Liberase solution (0.5mg/ml), and the organoids were minced with scissors. The mixture was incubated at 37°C for 20 mins with gentle triturate every 5 – 7 mins. After the first 5 mins, 10ul Dnase I (60U/ml) was added to the reaction. To stop the reaction, 9ml of Knock-out DMEM/F12 containing 10% FBS was added and centrifuged and filtered with 40um strainer. Cell pellets were resuspended in N2B27 basal medium and loaded to 10X Chromium controller for 3' single-cell RNA-seq (v3.1).

Sequencing reads from 10x Chromium scRNA-seq of individual samples were preprocessed, aligned, and quantified using 10x Genomics Cell Ranger (v6.1.2) and human reference hg38 (10x Genomics refdata-gex-GRCh38-2020-A). 10x Cell Ranger filtered data were used for downstream QC assessment and filters were then applied to keep cells with at least 500 genes, less than 100,000 unique molecular identifiers (UMIs), and less than 25% UMIs mapped to mitochondrial genes. Downstream analyses were performed in R v4.1.0 and python 3.

Analysis of individual human organoid scRNA-seq samples was performed using Seurat v4.2.0.[85] Data normalization and highly variable gene (HVG) identification were performed using SCTransform function with the effect of cell cycle scores and mitochondrial percentage regressed out. Zscore-scaled expression of HVGs was used for principal component analysis (PCA). The top 50 PCA dimensions with the largest variances were used for clustering analysis using Seurat FindClusters function and generation of UMAP visualizations using Seurat RunUMAP function. Cell clusters in each sample were identified using the Leiden algorithm.[86]

Genes selectively expressed in each cluster were identified using Seurat FindAllMarkers function with two-tailed Wilcoxon rank sum test and the following criteria: fold change >=1.5, Bonferroni adjusted p value<0.1, and expression percentage >=20%.

Integrations of human organoid scRNA-seq data from different samples were performed using Harmony v0.1.0,[87] including the integration of Day 3 B0-B3 samples, the integration of Day 21 vHIO and vHCO data, and the integration of the predicted mesenchymal cells or endothelial cells (ECs) from Day 21 vHLPO, vHIO, and vHCO samples. In each of the above integrations, raw gene expression count in cells of the selected samples and cell populations were extracted and merged, normalization and HVG identification were performed using Seurat SCTransform function with the effect of cell cycle scores and mitochondrial percentage regressed out, and PCA analysis was performed using the zscore-scaled expression of HVGs. Harmony based data integration was performed on the PCA dimensions. The top 200 PCA dimensions were used in all the integrations except the integration of Day 21 ECs that used the top 50 PCA dimensions. Harmony-corrected dimensions were used for generation of UMAP visualizations using Seurat RunUMAP function and cell clustering analysis using Seurat FindClusters function using the Leiden algorithm. Genes selectively expressed in each cluster were identified using Seurat FindAllMarkers function with two-tailed Wilcoxon rank sum test and the following criteria: fold change >=1.5, Bonferroni adjusted p value <0.1, and expression percentage >=20%. For the integrated Day 21 vHIO/HCO data, a small group of cells (n=17) were separated from all other cells in the UMAP projection and selectively expressed multiple immune marker genes (e.g., *CD14*, *CD163*, *CD84*, *SPI1*), we refined the cell identity of this group of cells as immune cells.

RNA velocity analysis of the integrated Day 3 samples was performed using velocyto v0.17.16[88] in python 3.6.3 for generation of the spliced and unspliced count matrices and using scVelo v0.2.4[89] with steady mode in python 3.9.16 for RNA velocity estimation and visualization.

Ligand-receptor based cell-cell communication analysis of Day 21 samples was performed using CellChat v1.4.0.[90] Cells annotated with "Low-quality" were not included in the analysis. Significant interactions were inferred using data from individual samples. Interactions for a sample involving cell types with less than 5 cells in the sample were excluded. Interactions from individual samples were merged for comparison and heatmap visualization based on the inferred interaction probabilities.

Epithelium maturation analysis

Maturation of epithelial cells in day 21 vHIO and cHIO was assessed based on their transcriptomic similarity with fetal SI cells in scRNA-seq from Yu et al. using the reference mapping algorithm in Seurat v4. Briefly, we first constructed a Seurat object of fetal SI using scRNA-seq of gastrointestinal and intestinal epithelial cells from Yu et al. and then used it as the reference to predict the fetal developmental time of vHIO and cHIO epithelial cells using the Seurat v4 reference mapping algorithm with the post-conception time as the annotation to predict. Predictions with score>=0.6 were considered confident. The majority of the organoid cells (>85%) were predicted as cells from two time points: 47 and 59 days post conception. Therefore, we re-built the fetal SI reference using the cells from these two time points and re-predicted the development time of day 21 vHIO and cHIO epithelial cells.

To assess the maturation of bud tip epithelial cells in day 21 vHLPO (cells with "epithelial progenitor-1" annotation) and cLPO (cells with "BTP" annotation), we first also performed the same prediction as described above using scRNA-seq of fetal lung epithelial cells from Yu et al. The majority of lung organoid distal epithelial cells (>97%) were predicted as post-conception day 80, which is the earliest time point of lung samples in the scRNA-seq of Yu et al. Therefore, we switched to use the scRNA-seq of cells annotated as distal epithelium from whole lung dissection (5 to 11 post-conception weeks) from He et al. as the reference and re-performed the prediction. Differential expression analysis comparing gene expression in day 21 vHLPO epithelial progenitor-1 vs. cLPO BTP cells was performed using Seurat FindMarkers function using two-tailed Wilcoxon rank sum test. Differential expression satisfying fold change >=1.5, expression percentage >=0.2, and Bonferroni adjusted p value <0.1 was considered significant.

Spatial transcriptomic analysis of transplanted vascularized organoids

Transplanted organoids were freshly collected, immersed in the O.C.T. compound, and immediately frozen on the dry ice. 10X10 Curio Seeker Spatial transcriptomic was performed following the manufacturer's instruction. This technique was developed based on the Slide-seq technology for high-resolution genome-wide expression analysis at a resolution of 10um diameter in each spot that was densely packed and randomly deposited. Briefly, 5 scrolls of tissue sections of 10um thickness were collected to derive an RNA integrity number (RIN) to test the tissue's RNA quality. All organoids' RIN numbers were higher than 8 to pass the quality test. One 10um thickness tissue section was placed on the Curio Seeker tile and mounted with 30um section of CryoCube. Then, the section was processed for hybridization, reverse transcription, and tissue clearance to yield Curio Seeker Bead resuspension. On the second day, 11 cycles of PCR was utilized for second-string synthesis and cDNA amplification. The purified cDNA was applied for Tagmentation with Dual Indexing Primer V2 and consequent library cleanup and QC. The final library was applied for NGS sequencing with NovaSeq6000 following the recommended sequencing depth.

Sequencing reads of Curio Seeker spatial transcriptomics profiling of vHLuO (n=1) was processed using Curio Seeker bioinformatics pipeline (v3.0.0) with the pre-built human and mouse mixed genome reference (Reference ID: GRCh38_mm10) downloaded from Curio Bioscience. Background noise was removed using the background-removal script from by Curio Bioscience (https://knowledgebase.curiobioscience.com/bioinformatics/background-removal-2). Then, beads with more than 20 UMIs mapped to mouse genes were excluded from downstream analysis. Seurat v5 was used for data visualization. Cytosignal[99] was used for identifying significant ligand-receptor interactions (n=260) using the built-in database with the following parameters: p.value =0.05, reads.thresh = 10, sig.thresh = 10.

The built-in interaction database in Cytosignal was based on the CellphoneDB v2 database. To facilitate the comparison, we also used CellphoneDB v2 with the same set of interactions to perform cell-cell communication analysis on fetal lung scRNA-seq from both Yu et al. and He et al. CellphoneDB v2 was run on individual time points of the scRNA-seq data, independently, with the following parameters: method=statistical analysis, threads=20, threshold=0.1, result-precision=4, counts-data= gene name, and iterations=10000. For scRNA-seq from Yu et al., cells with the following cell annotations from "lung-airway" and "lung-distal" tissues were used, including proximal epithelial (including Basal like, Ciliated, MUC2+ goblet), distal epithelial, mesenchyme, proliferative mesenchyme, pericyte, lymphatic and vascular endothelial cells. For the fetal lung scRNA-seq from He et al.,[29] cells with the following annotations were used, including proximal epithelial, distal epithelial, fibroblast, Myofibro & SMC, lymphatic and vascular endothelial.

Processing and analysis of published datasets

scRNA-seq of CS7 human embryo

Raw gene expression count matrix, cell cluster annotation, and UMAP coordinates of CS7 human embryo data[28] were downloaded from http://www.human-gastrula.net/. UMAP visualization of the data used the downloaded original UMAP coordinates. Prediction of CS7 cell types in the Day 3 human organoid scRNA-seq cells was performed using SingleR v1.6.1.[91]

scRNA-seq of E6.5-8.5 mouse embryo

Raw gene expression counts, cell metadata, and PCA dimensions were downloaded as a compressed file "atlas data.tar.gz" from https://github.com/MarioniLab/EmbryoTimecourse2018.[82] We converted mouse symbols to human symbols based on the human and mouse homology mapping (HOM MouseHumanSequence.rpt) downloaded from Mouse Genome Informatics (www.informatics.jax.org), used the count matrix with the converted human symbols for Seurat v4 object construction, normalized data using Seurat SCTransform function, performed supervised PCA analysis (SPCA) on the original PCA dimensions, and used the SPCA dimensions to generated a UMAP model using Seurat RunUMAP function with "return.model=T". The constructed Seurat object with the UMAP model were used for reference mapping of Day 3 human organoid scRNA-seq using Seurat FindTransferAnchors and MapQuery functions, including transferring mouse embryo cell type labels to human organoid cells and projecting human organoid cells to the UMAP coordinates of the mouse data.

Data of mouse E6.5∼E8.5 'Gut' subtypes were extracted from the above whole dataset by selecting cells with the following "endo gutCluster" annotations, including Foregut 1, Foregut 2, Hindgut 1, Hindgut 2, Midgut, Midgut/Hindgut, Pharyngeal endoderm. Data were used to construct a Seurat v4 object with SCTransform based normalization followed by PCA analysis and UMAP model generation. The constructed Seurat object with the UMAP model were used for reference mapping of Day 3 human organoid scRNA-seq using Seurat FindTransferAnchors and MapQuery functions, including transferring mouse gut cell type labels to human organoid cells and projecting human organoid cells to the UMAP coordinates of the mouse data.

scRNA-seq of E9.0 mouse anterior gut data

Mouse embryos from E8.5, E9.0 and anterior and posterior E9.5 foreguts were collected, sequenced, processed, and annotated as previously described.[49] Counts matrices for all cells and all the time points, as well as the annotated Metadata for all cells, were downloaded from NCBI GEO. Data was converted into Seurat object, and cell proportions of "LineageAnnotations" by "Stages" as defined in the Metadata were determined using Seurat's count table function.

scRNA-seq of E8.75 mouse anterior and posterior gut data

Raw gene expression count matrix of all cells and cell metadata (cell index, cluster, time point, and cell type annotation) were downloaded from https://endoderm-explorer.com/.[48] We subset the data to E8.75 anterior and posterior cells based on the original cell cluster annotation (E8.75 ap clusters) and determined anterior (n=3,579) and posterior (n=3,667) cells based on the original cell index labeling. Data normalization and dimension reduction were performed using Seurat SCTransform function followed by RunPCA function. Anterior and posterior data were integrated using Harmony v0.1.0[87] using the top 200 PCA dimensions. UMAP visualization was generated using Seurat RunUMAP function using the harmony-corrected dimensions.

To assess the correlation of anterior and posterior cell types, we created a pseudo-bulk gene expression profile for each of the anterior and posterior cell types by averaging the expression of each gene in all cells in the given cell type, found highly variable genes (HVGs) among pseudo-bulk profiles using Seurat FindVariableFeatures function, performed PCA analysis using zscore-scaled pseudo-bulk expression of HVGs, and assessed Pearson's correlation among cell types based on the top 10 PCA dimensions. Hierarchical clustering analysis and heatmap visualization were performed using R package pheatmap (v1.0.12) using the correlation matrix as input.

Differential gene expression between mouse anterior vs. posterior cells or between Day 7 human organoid vAFG-'B1' vs. vMHG-'B3' cells were identified using Seurat FindMarkers function using log normalization data and two-tailed Wilcoxon rank sum test with the following criteria: fold change >=1.2, p value <0.05, and expression percentage >=10%.

For pseudo-bulk correlation analysis with human organoid data, we converted mouse symbols to human symbols based on the human and mouse homology mapping (HOM MouseHumanSequence.rpt) downloaded from Mouse Genome Informatics (www.informatics.jax.org). Pseudo-bulk correlation analysis of Day 7 human organoid scRNA-seq cell clusters with mouse anterior and posterior gut tube cell types were performed as follows. First, we created a pseudo-bulk gene expression profile for each of the mouse and human cell clusters by averaging the expression of each gene in all cells in the given cell cluster. Then Seurat's FindVariableFeatures was used to find the top 2000 highly variable genes (HVGs) among the mouse pseudo-bulk profiles, denote HVG1, and the HVGs among the human organoid pseudo-bulk profiles, denote HVG2. We took the union of HVG1 and HVG2 and

kept the genes that are present in both human and mouse data. We performed zscore scaling of the expression of HVGs among the human and mouse pseudo-bulk profiles, separately. Pearson's correlations among all the pseudo-bulk profiles were calculated using the scaled expression of HVGs. Hierarchical clustering analysis and heatmap visualization were performed using R package pheatmap (v1.0.12) using the correlation matrix as input.

scRNA-seq of conventional human lung organoids

Raw sequencing reads from 10x scRNA-seq of day 10 spheroids and 3-week lung progenitor organoids (LPOs) were downloaded from ArrayExpress using accession number E-MTAB-11953 (sample number ERS12457826 for day 10 spheroids; ERS12457827 and ERS12457828 for two biological replicates of 3-week LPOs).[31] Sequencing reads of individual samples were preprocessed, aligned, and quantified using 10x Genomics Cell Ranger (v6.1.2) and human reference hg38 (10x Genomics refdata-gex-GRCh38-2020-A). 10x Cell Ranger filtered data were used for downstream QC assessment. The QC criteria reported in Hein et al. were used to perform cell pre-filtering: for day 10 spheroids, cells with 500-8,000 expressed genes, 500-50,000 unique molecular identifiers (UMIs), and <10% UMIs mapped to mitochondrial genes were included in the downstream analysis; for 3-week LPOs, cells with 500-7,000 expressed genes, 500-50,000 UMI counts, and <10% UMIs mapped to mitochondrial genes were included. Downstream analyses were performed using Seurat v4.2.0 in R v4.1.0. Data normalization and HVG identification were performed using SCTransform function with the effect of cell cycle scores and mitochondrial percentage regressed out. Two biological replicates of 3-week LPOs were integrated using Harmony v0.1.0. Cell clusters were identified using the Seurat FindClusters function with Leiden algorithm: resolution=0.8 for the LPO cell clusters and resolution=0.3 for the spheroid cell clusters. Cell clusters were assigned to cell types based on the expression of marker genes used in Hein et al.[31] For the day 10 spheroid data, a small group of cells (n=15) were separated from all other cells in the UMAP projection and selectively expressed multiple endothelial marker genes (e.g., *KDR, CDH5, PECAM1, ESAM*). We refined the cell identity of this group of cells as endothelium progenitors.

scRNA-seq of human intestinal organoids

Raw sequencing reads from 10x scRNA-seq of hindgut ('day 0' sample) and human intestinal organoids (HIOs) were downloaded from ArrayExpress using accession number E-MTAB-9228 (sample number ERS4758594 and ERS4758595 for the 'day 0' and 'day 14' HIO data, respectively; and ERS4758598 and ERS4758599 for 2-month HIO and vHIO data, respectively). Sequencing reads of individual samples were preprocessed, aligned, and quantified using 10x Genomics Cell Ranger (v6.1.2) and human reference hg38 (10x Genomics refdata-gex-GRCh38-2020-A). 10x Cell Ranger filtered data were used for downstream QC assessment. The following QC criteria used in the GitHub code of Holloway et al.[13] were applied to select cells for downstream analysis, including 1,000-9,000 expressed genes, <60,000 unique molecular identifiers (UMIs), and <10% UMIs mapped to mitochondrial genes. Downstream analyses were performed using Seurat v4.2.0 in R v4.1.0. Data normalization and HVG identification were performed using SCTransform function with the effect of cell cycle scores and mitochondrial percentage regressed out. For the 2-month HIO and vHIO data, batch correction was performed using Harmony prior to clustering and cell type annotation analysis. Cell clusters were identified in day 0, day 14, and 2 month data, separately, using the Seurat FindClusters function using Leiden algorithm with resolution=0.8. Cell clusters were assigned to cell types based on the expression of marker genes used in Holloway et al.[13]

scRNA-seq of fetal human lung

Raw gene expression counts, cell metadata, PCA dimensions, and UMAP coordinates of all scRNA-seq of fetal human lung cells were downloaded as an h5ad file "Assembled10DomainsFiltered.h5ad" from https://fetal-lung.cellgeni.sanger.ac.uk/.[29] We created a Seurat v4 object using the raw count matrix and cell metadata and normalized data using log normalization. Prediction of fetal human lung cell types in Day 21 vHLPO cells was performed using SingleR v1.6.1.[91] We first performed the prediction using the "broad celltype" annotation of fetal lung cells. Predictions were grouped into four cell lineages as follows for comparison with the cluster based Day 21 vHLPO cell types: endothelial (Lymph endothelial and Vas endothelial), epithelial (Distal/Proximal epithelial), immune (T & ILC, B, NK, Other myeloid, Meg-ery), Mesen&PNS (Fibroblast, Mesothelial, Myofibro & SMC, Chondrocyte, PNS). We then iterated into the prediction of fetal lung cell types within each lineage for the Day 21 vHLPO cell clusters.

scRNA-seq of developing human endodermal organs

scRNA-seq count matrix and metadata of fetal atlas cells[32] (n=155,232) were downloaded from Mendeley data using DOI listed in the key resources table. The original "cell type" annotation was used in the downstream analysis except that the endothelial cells (ECs) were further classified into lymphatic ECs and vascular ECs as described in the following. We extracted gene count matrix of the predicted ECs (n=5,375) based on the "Major cell type" annotation, constructed a Seurat v4 object, normalized gene expression using the Seurat SCTransform function followed by a PCA analysis, integrated data from different samples using Harmony, and identified cell clusters using the Leiden algorithm. Cells (n=1,167) in the clusters with co-expression of pan-EC (*CDH5*, *CLDN5*) and immune, epithelial or fibroblast cell markers were annotated as "Contaminated" cells. Lymphatic ECs (n=279 cells) were identified based on the cell cluster with selective co-expression of marker genes: *CDH5*, *CLDN5, PROX1*, *LYVE1*, and *PDPN*. Vascular ECs (n=3,929 cells) were identified based clusters with selective co-expression of *CDH5*, *CLDN5*, *PLVAP*, and *EMCN*.

To assess the tissue identity of day 21 human organoid mesenchymal cells, we performed both a correlation analysis and a SingleR based tissue identity prediction described in the following. For the correlation analysis, we first created a pseudo-bulk gene expression profile for the mesenchymal cells in each of the fetal and organoid samples by averaging the expression of each gene in all the predicted mesenchymal cells of the given sample. For the fetal tissue data, mesenchymal cells were identified based on the original "Major cell type" annotation and samples of ages earlier than 80 post-conception days were used. For the organoid samples, mesenchymal cells included fibroblasts, proliferative fibroblasts, pericytes, and smooth muscle cells. Seurat's FindVariableFeatures

was used to find highly variable genes (HVGs) among the fetal tissue pseudo-bulk profiles, denote HVG1, and the HVGs among the human organoid pseudo-bulk profiles, denote HVG2. We took the intersection of HVG1 and HVG2 and kept the genes that are present in both fetal tissue and organoid data. We performed zscore scaling of the expression of HVGs among the fetal tissue and organoid pseudo-bulk profiles, separately. Pearson's correlations among all the pseudo-bulk profiles were calculated using the scaled expression of HVGs. Hierarchical clustering analysis and heatmap visualization were performed using R package pheatmap (v1.0.12) using the correlation matrix as input.

For the SingleR based prediction of fetal tissue identity in the mesenchymal cells of day 21 organoids, we constructed a reference data object using gene expression in the predicted mesenchymal cells from ileum, jejunum, and distal lung tissues from samples at the age of 80 post-conception days. Data from different samples were integrated using Harmony for a UMAP visualization. The prediction of fetal SI or lung tissue identities for the day 21 organoid mesenchymal cells was performed using SingleR v1.6.1.[91] Using the same SingleR based approach, we also performed the prediction of fetal SI or lung tissue identities for the ECs in the day 21 human organoid samples.

Ligand-receptor based cell-cell communication analysis was performed using CellChat v1.4.0[90] on data from the following tissues: Colon, Lung-distal, Lung-airway, Jejunum, Ileum, Duodenum. Data from the age of 80 post-conception days were used as all the above tissues have >1000 cells from the samples of this age. Original cell type annotation was used except that ECs were classified to vascular EC, lymphatic EC, and contaminant based on the analysis as described above. Mesenchyme subtypes (n=5) were merged as "Mesenchyme". Similarly, sub-types of "Macrophage/monocyte" and "T cell/NK cell" were merged, respectively. Cells annotated with "Contaminated" or "Undefined" were not included in the analysis. Significant interactions were inferred using data from individual tissues. Interactions for a sample involving cell types with less than 5 cells in the sample were excluded. For lung tissues, interactions involving "Enteroendocrine", "Gastrointestinal epithelium", and "Intestinal epithelium" were excluded. Interactions from individual tissues were merged for comparison and heatmap visualization based on the inferred interaction probabilities.

Tabula Sapiens scRNA-seq atlas

Tabula Sapiens scRNA-seq data with cell metadata from 25 organs of eight normal human subjects in Tabula Sapiens were downloaded as h5ad files from figshare.com listed in the key resources table. EC cells within each tissue were determined based on the "compartment" annotation (i.e., compartment = endothelial) from the original publication.[2] We integrated ECs from all tissues using Harmony and identified cell clusters using Leiden algorithm. Cell clusters with co-expression of lymphatic markers (*CCL21*, *PROX1*, *LYVE1*, and *PDPN*) were annotated as lymphatic ECs, and the remaining cells were annotated as vascular ECs. Lung vascular EC specific markers were identified using the following approach. First, we identified genes differentially expressed in vascular EC cells within each data sample (determined based on the original "organ" annotations) using Seurat FindMarkers with two-tailed Wilcoxon rank sum test comparing gene expression in ECs with gene expression in all other cells in the tissue. Log normalized data were used for the DE test and the following DE criteria were used: p value <0.05, fold change >=1.2 in EC, and expression percentage >=20% in EC. We took the union of EC DEGs from all tested tissues and identified lung vascular EC specific genes using the following criteria: (i) differentially expressed (Bonferroni-adjusted p value <0.1 and fold change >=1.5) in lung vascular ECs when compared to vascular ECs in all other tissues; (ii) expression percentage >=20% in lung vascular ECs; and (iii) average expression in the lung vascular EC is at least 1.25 fold higher than its average expression in vascular ECs of any of other tissues.

QUANTIFICATION AND STATISTICAL ANALYSIS

For all image quantification, ImageJ and Imaris software were used. To quantify vascular integration in both organoids and tissues, the vascular network surfaces were first created using the 'Surface' module with the Imaris software. Afterward, the shortest distance from each epithelial cell to the vascular surface was measured, based on which the number of cells that fell within each 5um shortest distance unit was calculated and converted to the frequency by normalization to the total epithelial cell number. The frequency distribution for each imaging object was plotted in GraphPad Prism 8.0 and the Gaussian curve was created by nonlinear regression of the frequency distribution. The vascular network parameters were calculated with Imaris software with the 'Neurofilament' module.

Normal distribution from each group was confirmed using c2 test before any comparison between groups. All data represent mean ± SEM. Statistical significance was determined by parametric tests (all data possesses equal variance p>0.05): unpaired 2-tailed t-test, ANOVA (>2 groups) with Bonferroni test as indicated; or non-parametric test: Mann-Whitney (2 groups). A p value of <0.05 was considered significant. *p<0.05, **p<0.01, ***p<0.001. Statistical details can be found in the figure legends. n represents different specimens from different cell lines, biological repeats, or patients or control subjects. The exact information for the n was specified in the figure legends. All violin plot data were tested by Bonferroni correction test and FDR<0.05 was regarded as significant. Analyses were carried out using GraphPad Prism 8.0. As for all the experiments, at least three independent experiments were performed to reach the minimal requirement for statistical significance, unless otherwise specified. Blinding or randomization was not performed unless otherwise specified. Exclusion is not applied in this study.

Supplemental figures

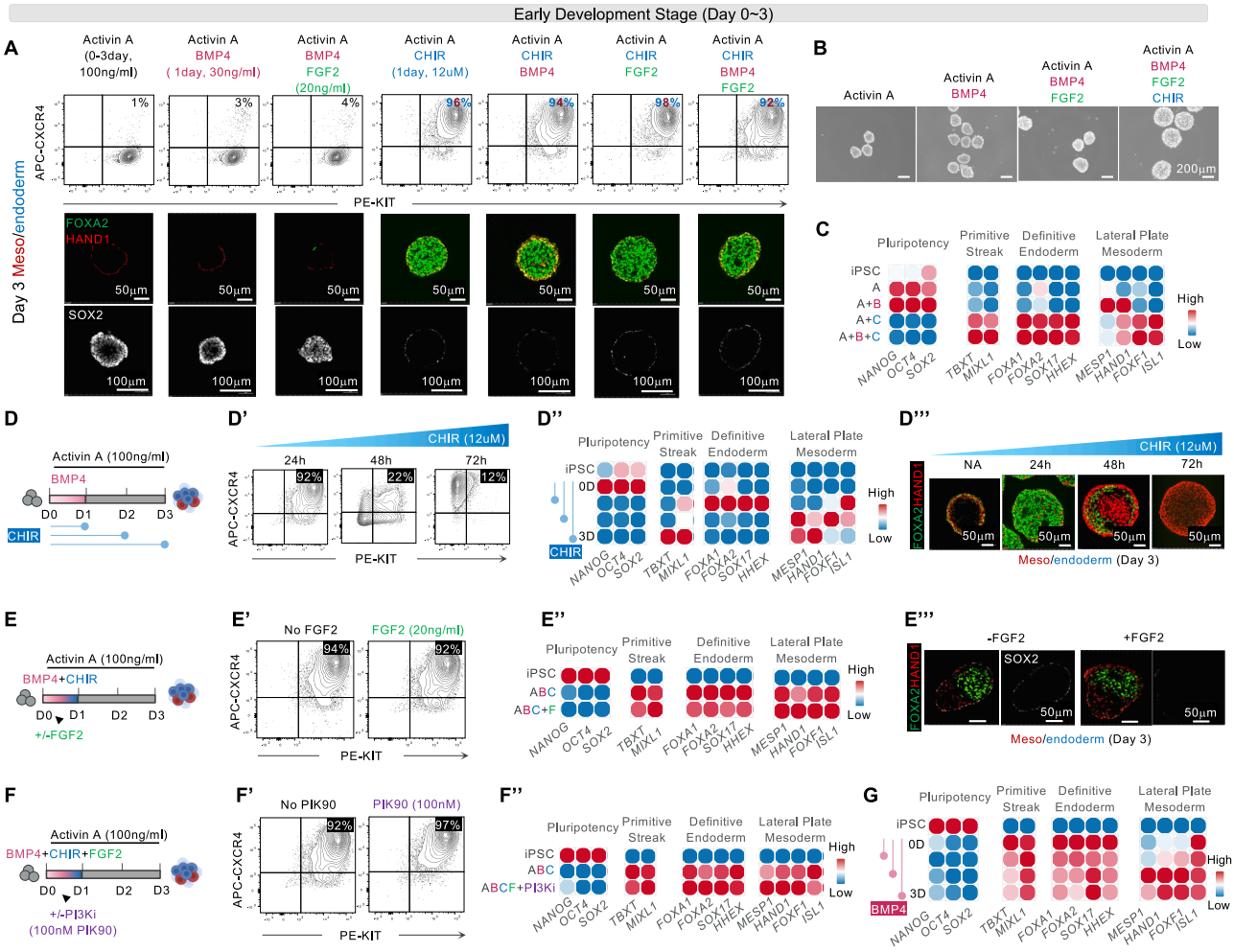

Figure S1. Devising the protocol for differentiating day 3 meso endoderm spheroid, related to Figure 1

(A) Fluorescence activated cell sorting (FACS) analysis and whole mount staining for the day 3 spheroids subjected to various treatments. Treatment duration: activin A (100 ng/mL), days 0 3; BMP4 (30 ng/mL), day 0 1; CHIR (12 μM), day 0 1; FGF2 (20 ng/mL), days 0 1. SOX2, pluripotent stem cell; FOXA2, DE; HAND1: lateral plate mesoderm; $CXCR4^+/KIT^+$: DE.

(B G) (B) Bright field phase contrast images of day 3 spheroids from (A). FACS (D′/E′/F′), qPCR heatmap (C/D″/E″/F″/G), and whole mount staining (D‴/E‴) to characterize the effect of Wnt activation by CHIR (12 μM) (D), FGF2 (20 ng/mL) (E), PI3K inhibition (100 nM PIK90) (F), BMP4 (30 ng/mL) (G), or combination (C) on patterning mesoderm and endoderm in day 3 spheroids. *n* = 3 biological repeats in each treatment group in heatmap qCPR data.

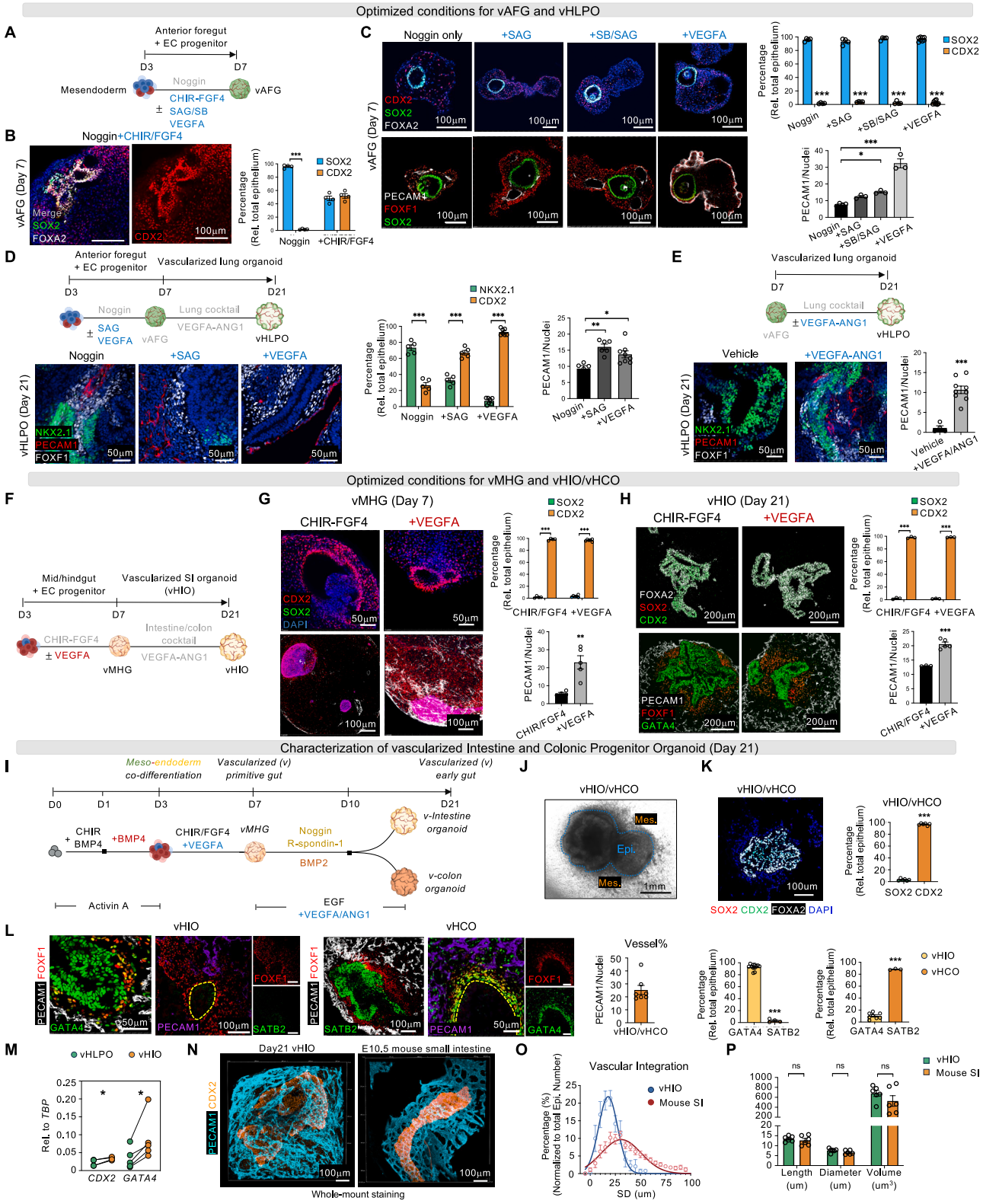

(legend on next page)

Figure S2. Optimization and characterization of day 7 vascularized primitive gut organoid and day 21 vascularized lung and intestine organoid, related to Figure 1

(A) Schematic illustration of conditions for proper vAFG generation.

(B) Spheroids were treated with CHIR (2 μM)+FGF4 (500 ng/mL) from days 3 to 7, followed by immunostaining on day 7 for anterior gut (SOX2/FOXA2) and posterior gut (CDX2/FOXA2) markers.

(C) Spheroids were treated with SAG (1 μM), SB431542 (10 μM), or VEGFA (100 ng/mL) from days 3 to 7, followed by immunostaining on day 7 for anterior gut (SOX2/FOXA2), posterior gut (CDX2/FOXA2), endothelial (PECAM1), and mesenchymal (FOXF1) markers.

(D) Spheroids were treated with SAG (1 μM) or VEGFA (100 ng/mL) from days 3 to 7, followed by immunostaining on day 21 for lung epithelial (NKX2.1), endothelial (PECAM1), and mesenchymal (FOXF1) markers.

(E) Spheroids were exposed to VEGFA (100 ng/mL) and ANG1 (100 ng/mL) from days 7 to 21, followed by immunostaining on day 21 for lineage specific makers.

(F–H) (F) Schematic illustration of conditions for proper vMHG generation. Spheroids from days 3 to 7 were tested for VEGFA (100 ng/mL), and vessels were further maintained via supplementing VEGFA (100 ng/mL) and ANG1 (100 ng/mL) from days 7 to 21. Immunostaining on day 7 vMHG (G) and day 21 vHIO (H) for epithelial (CDX2, FOXA2, GATA4), endothelial (PECAM1), and mesenchymal (FOXF1) markers.

(I) Schematic illustration of conditions for proper vHIO and vHCO generation at day 21.

(J) Bright field image of day 21 vHIO/vHCO. Blue dashed line outlined the epithelium border in vHIO/vHCO, which showed similar structure.

(K) Immunostaining of foregut and mid/hindgut epithelial markers in day 21 vHIO/vHCO.

(L) Confirmation of epithelial lineage purity and vascular percentage in vHIO and vHCO by using SI (GATA4) and colon (SATB2) markers. The dashed yellow circles highlighted the epithelial layer. FOXF1: mesenchyme.

(M) qPCR detection of intestine marker expressions in day 21 vHLPO and vHIOs.

(N) Whole mount staining of vasculature (PECAM1) and intestine epithelium (CDX2) in day 21 vHIO and E10.5 mouse intestine tissue.

(O) Vascular integration index for (N).

(P) Vascular structure parameters from (N). In (M), *n* = stem cell line. Dots connected by the same line represented the same stem cell line. Otherwise, *n* = biological repeat. t test: (E, K, L, and M). ANOVA test: (B–D, G, H, and P). Data are represented as mean ± SEM.

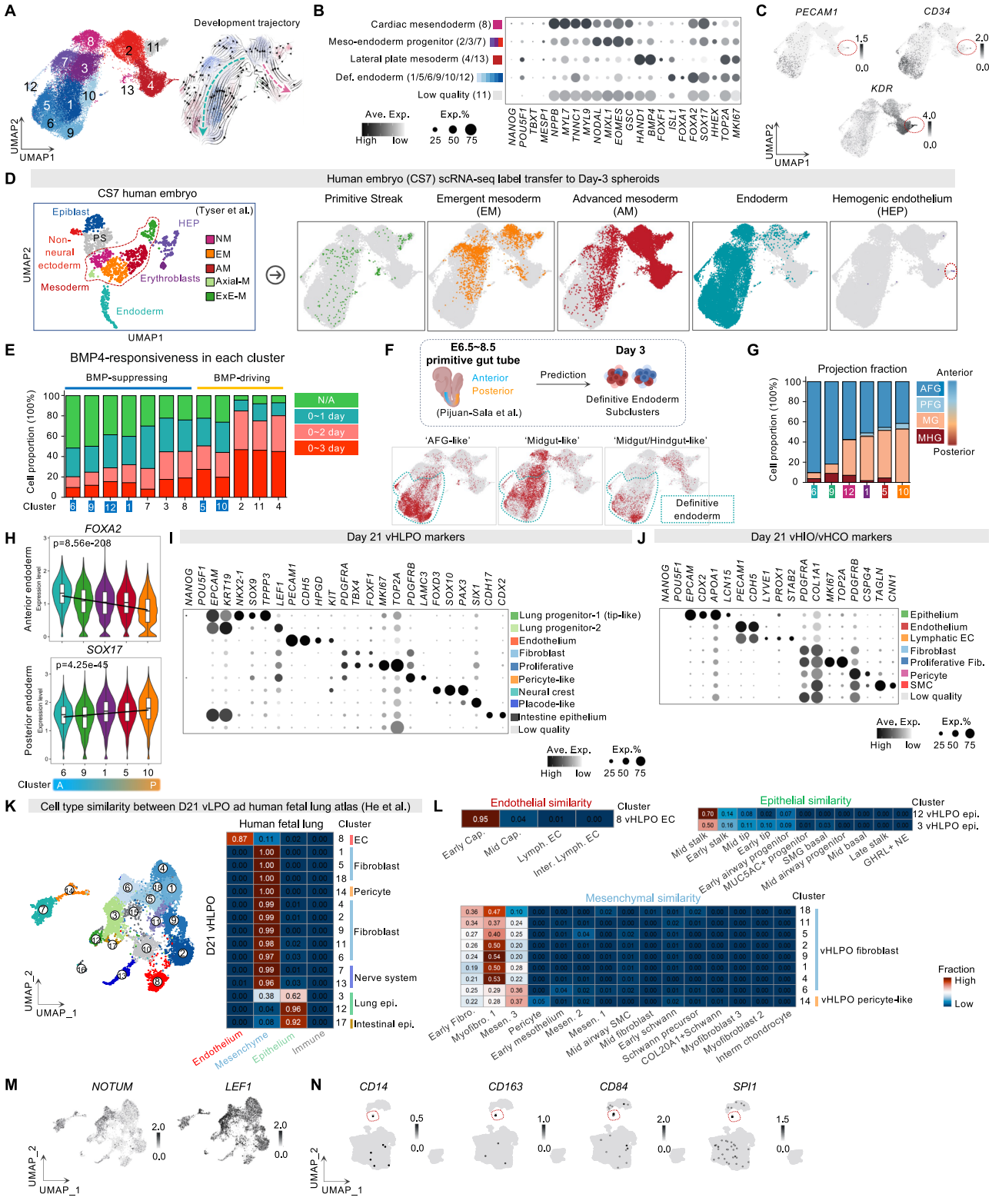

Figure S3. scRNA seq characterization of day 3 meso endoderm spheroids and day 21 vHLPO, vHIO, and vHCO, related to Figures 1 and 2

(A) scRNA seq UMAP projection and RNA velocity analysis of day 3 meso endoderm spheroids. Arrows indicated the developmental trajectory directions determined by velocyto algorithm.

(B) Dot plot of representative genes for each cluster from Figure 1P.

(legend continued on next page)

(C) Feature plots for endothelial progenitor markers.
(D) Automated cell type annotation of day 3 meso endoderm spheroids using SingleR and the scRNA seq of human embryo at CS7 stage (Tyser et al.[28]) as the reference. Left: UMAP of scRNA seq of human embryo at CS7. Right: UMAP of the integrated day 3 spheroids with cells colored by the predicted CS7 human embryo cell types. NM, nascent mesoderm; ExE M, extra embryonic mesoderm.
(E) The distribution of day 3 spheroid samples subjected to different BMP4 treatment durations in each cell cluster.
(F) Prediction of day 3 DE subtypes based on mouse E6.5 8.5 "gut" subtypes (Pijuan Sala et al.[82]). Mouse "gut" included the anterior foregut (AFG), posterior foregut (PFG), midgut, midgut/hindgut, and hindgut. Dashed lines circled DE clusters.
(G) Day 3 spheroid DE subcluster anterior posterior prediction fraction, based on (F).
(H) Violin plots showing the expression of known anterior and posterior endoderm genes across DE subclusters. *p* value represents the significance of the difference in gene expression between cluster C6 and cluster C10 cells using a two tailed Wilcoxon rank sum test.
(I) Day 21 vHLPO dot plot of marker genes for each cell type. Annotation of lung progenitor clusters is based on human fetal lung atlas (He et al.[29]).
(J) Dot plot of marker genes for each cell type in day 21 vHIO/vHCO.
(K) Day 21 vHLPO UMAP and generic cell type comparison between vHLPO and human fetal lung.
(L) Lung mesenchyme, endothelium, and epithelium subtypes similarity between day 21 vHLPO and human fetal lung.
(M) Feature plots of *NOTUM* and *LEF1* genes in day 21 vHLPO.
(N) Feature plots of immune/macrophage markers in day 21 vHIO/vHCO.

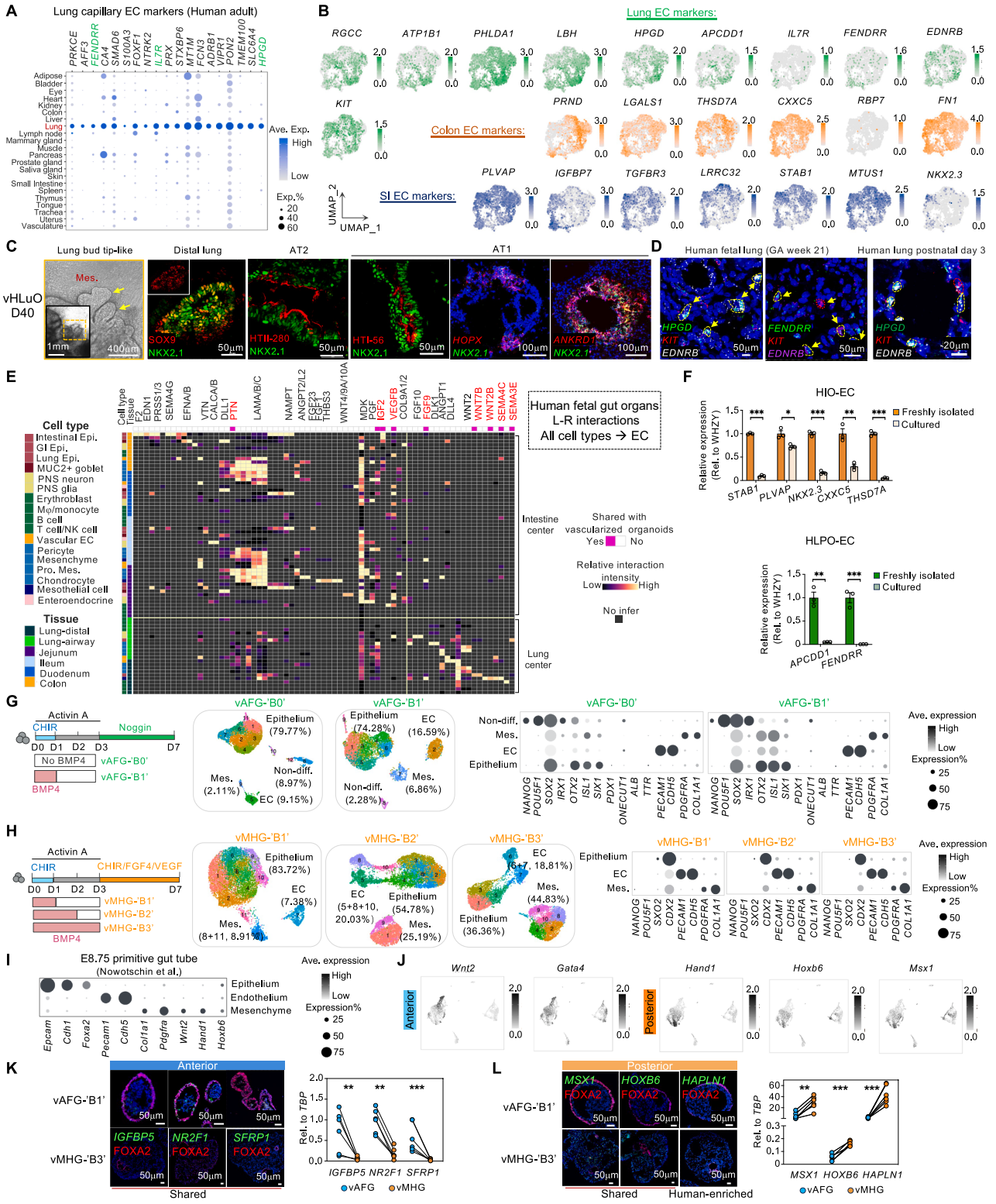

Figure S4. Characterization of context specific ECs and mesenchyme within vascularized organoids, related to Figures 2 and 3

(A) Dot plot of lung capillary EC specific genes in the human adult (Tabula Sapiens). Green labeled genes were verified in smFISH staining.

(B) Feature plots of lung, SI, and colon EC markers in vascularized organoid ECs.

(legend continued on next page)

(C) Maturation of vHLPO *in vitro*. Brightview image showing lung bud tip like morphology (yellow arrows) in day 40 vHLuOs. Immunostaining of day 40 vHLuOs showing distal lung epithelial marker (SOX9/NKX2.1), AT2 marker (HTII 280), and AT1 marker (HT1 56). Additional AT1 markers were determined by smFISH (*HOPX/ANKRD1*).

(D) smFISH staining of human lung EC markers *HPGD*, *KIT*, *FENDRR*, and *EDRNB* in human fetal and post natal lung tissues. Yellow dash: *HPGD*$^{+}$; red dash: *KIT*$^{+}$.

(E) L R pairs revealed by scRNA seq in human fetal gut organs (Yu et al.[32]) were selected for receptors expressed in the endothelium. The pink block "common" and red colored label indicated L R pairs shared by the organoids and human fetal tissues. CellChat was used for the L R analysis.

(F) qPCR of intestine and lung EC marker expressions in freshly isolated and culture ECs from vascularized organoids.

(G) UMAP and marker genes dot plots for samples vAFG "B0" and vAFG "B1." Non diff.: non differentiation; Mes., mesenchyme; EC, endothelial cell.

(H) UMAP and marker genes dot plots for samples vMHG "B1," vMHG "B2," and vMHG "B3." Numbers indicated the percentage of each cell type.

(I) Dot plot of marker genes for mouse E8.75 primitive gut tube cell types (Nowotschin et al.[48]).

(J) Feature plots of genes representing anterior and posterior mouse primitive gut tube mesenchyme.

(K and L) smFISH staining and qPCR for anterior and posterior mesenchymal markers in day 7 vAFG and vMHG. Markers were revealed in Figure 3F. In (K) and (L), *n* = stem cell line. Dots connected by the same line represented the same stem cell line. *n* = biological repeat. t test: (F, K, and L). Data are represented as mean ± SEM.

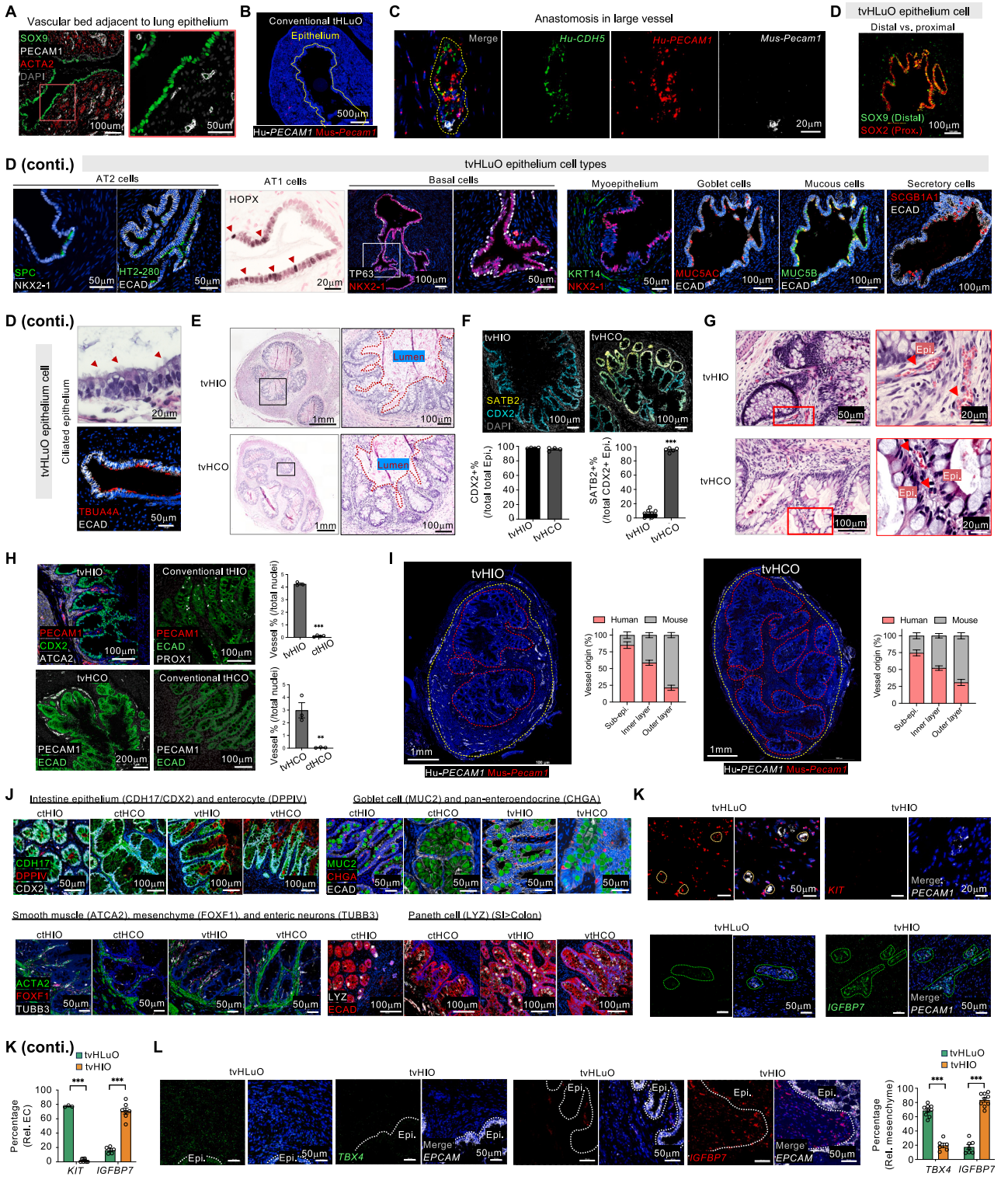

Figure S5. Characterization of transplanted vHLuO, vHIO, and vHCO related to Figure 4

(A) Immunostaining of sub epithelium vascular units. Red box: zoom in view of vessels (PECAM1^{+}) adjacent to distal lung epithelium (SOX9^{+}). ACTA2: vascular smooth muscle cells.

(B) Human and mouse vessels within the transplanted conventional lung organoid as revealed by smFISH. Dashed white line outlined the epithelial layer.

(legend continued on next page)

(C) Anastomosis structure connecting human and mouse vessels in tvHIOs as revealed by human and mouse endothelial smFISH probes. Yellow dashed line outlined the vessel structure.
(D) Characterization of lung epithelium within tvHLuO by immunofluorescent and immunohistochemistry staining. Red arrowhead: $HOPX^+$ AT1 cells or ciliated lung epithelium; NKX2 1 or ECAD: general lung epithelium.
(E) H&E staining showing the gross view of transplanted vascularized SI and colonic organoids. Dashed red line outlined the lumen.
(F) Immunostaining of colonic epithelium in tvHIO and tvHCO. SATB2: colon epithelium. CDX2: general intestine epithelium.
(G) H&E staining indicated perfused small vessels and capillary beds adjacent to the epithelial layer in tvHIO and tvHCO. Red arrowhead: vessels filled with red blood cells.
(H) Vessels within the transplanted vascularized and conventional SI and colonic organoids. Epithelium: ECAD or CDX2 positive. Mesenchyme: ACTA2. Endothelium: PECAM1.
(I) Human and mouse vessels within the transplanted SI and colon organoid as revealed by smFISH. Inside red dashed circle: sub epithelium layer; outside yellow dashed circle: outer layer; in between: inner layer. *n* = three organoids in each group for quantification.
(J) Characterization of intestinal epithelial cell types within conventional tHIO, tHCO, and vascularized tvHIO, tvHCO by immunofluorescent staining. CDX2 or ECAD: intestine epithelium.
(K) smFISH staining of lung (*KIT*) and intestine EC marker (*IGFBP7*) in tvHLuO and tvHIO.
(L) smFISH staining of lung (*TBX4*) and intestine mesenchymal marker (*IGFBP7*) in tvHLuO and tvHIO. *n* = biological repeat. t test: (F, H, K, and L). Data are represented as mean ± SEM.

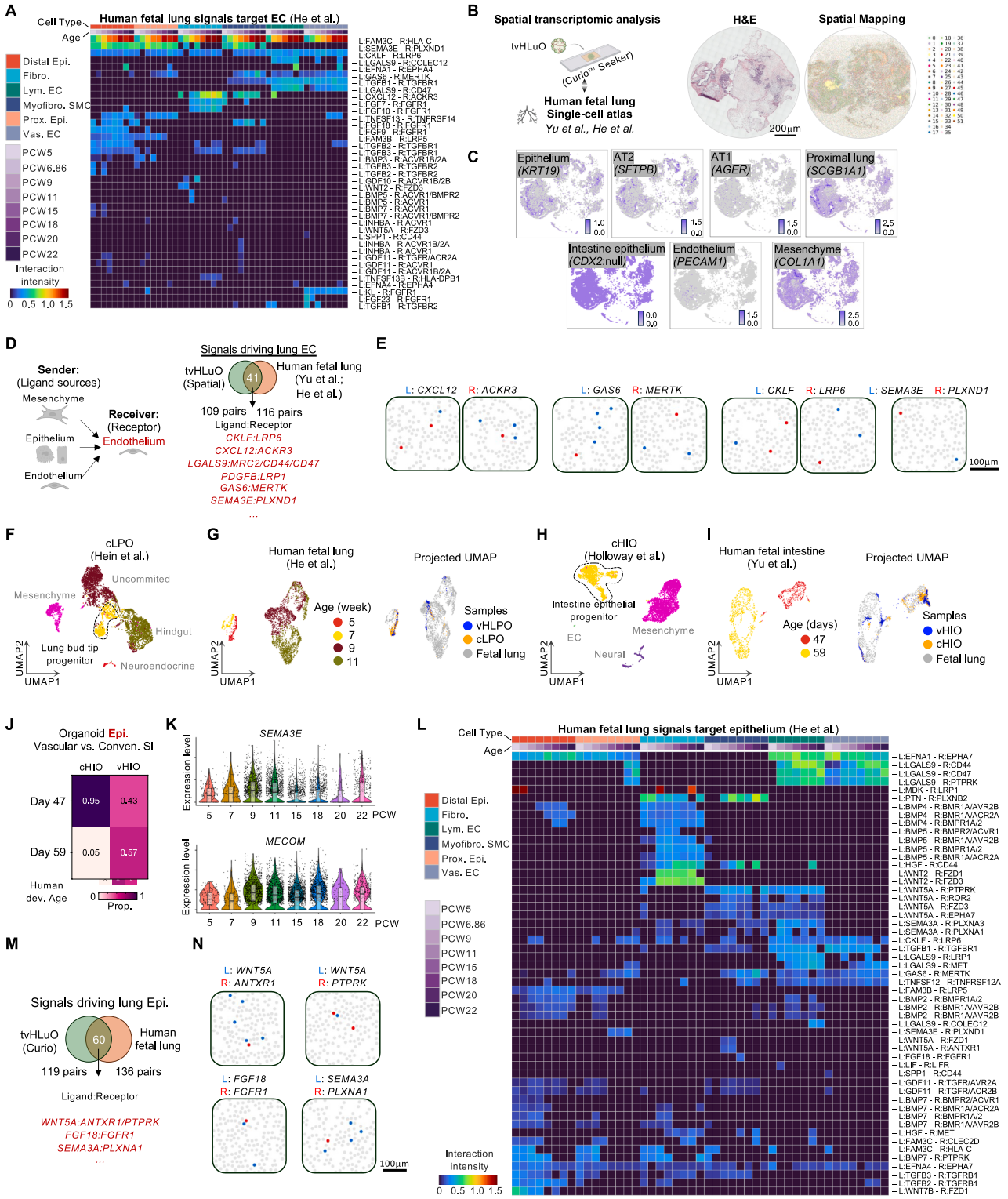

Figure S6. scRNA seq and spatial transcriptomic analysis of EC driving ligands and epithelial maturation on vHPO, vHIO, and tvHLuO, related to Figures 4 and 5

(A) Heatmap of L R gene expressions in human fetal lung scRNA seq database from He et al.[29] Receptors are expressed in lung endothelium. L, ligand; R, receptor.

(legend continued on next page)

(B) Top: illustration of spatial transcriptomic analysis on tvHLuO to reveal spatial coordination of L R pairs. Slide seq based Curio Seeker platform was applied. H&E staining (bottom left) and spatial mapping (bottom right) of tvHLuO on Curio slides.
(C) Spatial feature plots of representative cell markers in tvHLuO.
(D) Based on human fetal lung scRNA seq[29,32] and spatial transcriptome, L R pairs targeting lung endothelium cells were revealed. 33 L R pairs were shared by both human fetal lung and tvHLuO.
(E) Representative L R beads on tvHLuO Curio slide targeting endothelium (PECAM1$^+$). Receptor (R, red) is expressed in endothelium.
(F) UMAP projection showing the lung epithelial clusters[31] used for maturation analysis from day 21 cLPO.
(G) Human fetal lung epithelium UMAP[29] containing multiple development stages and the prediction of lung organoid epithelium to human fetal lung.
(H) UMAP projection showing the SI epithelial clusters[13] used for maturation analysis from day 21 cHIO.
(I) Human fetal SI epithelium[32] UMAP containing multiple development stages and the prediction of SI organoid epithelium to human fetal SI.
(J) Epithelial maturation comparison among day 21 vHIO, cHIO, and human fetal SI. Proportions of cells projected to each fetal lung development stage were shown as heatmap. Prop., proportions.
(K) Violin plots showing the expression of *SEMA3E* and *MECOM* across different development stages in the human fetal lung.
(L) Heatmap of L R gene expressions in human fetal lung scRNA seq database from He et al.[29] Receptors are expressed in lung epithelium. L, ligand; R, receptor.
(M. Based on human fetal lung scRNA seq and spatial transcriptome, L R pairs targeting lung epithelial cells were revealed. 60 L R pairs were shared by both human fetal lung and tvHLuO.
(N) Representative L R beads on tvHLuO Curio slide targeting epithelium (EPCAM$^+$). Receptor (R, red) is expressed in epithelium.
In (A) and (L), CellphoneDB was used for L R interaction analysis. Zero intensity represents an interaction that is not significant or the ligand and/or receptor was not expressed.

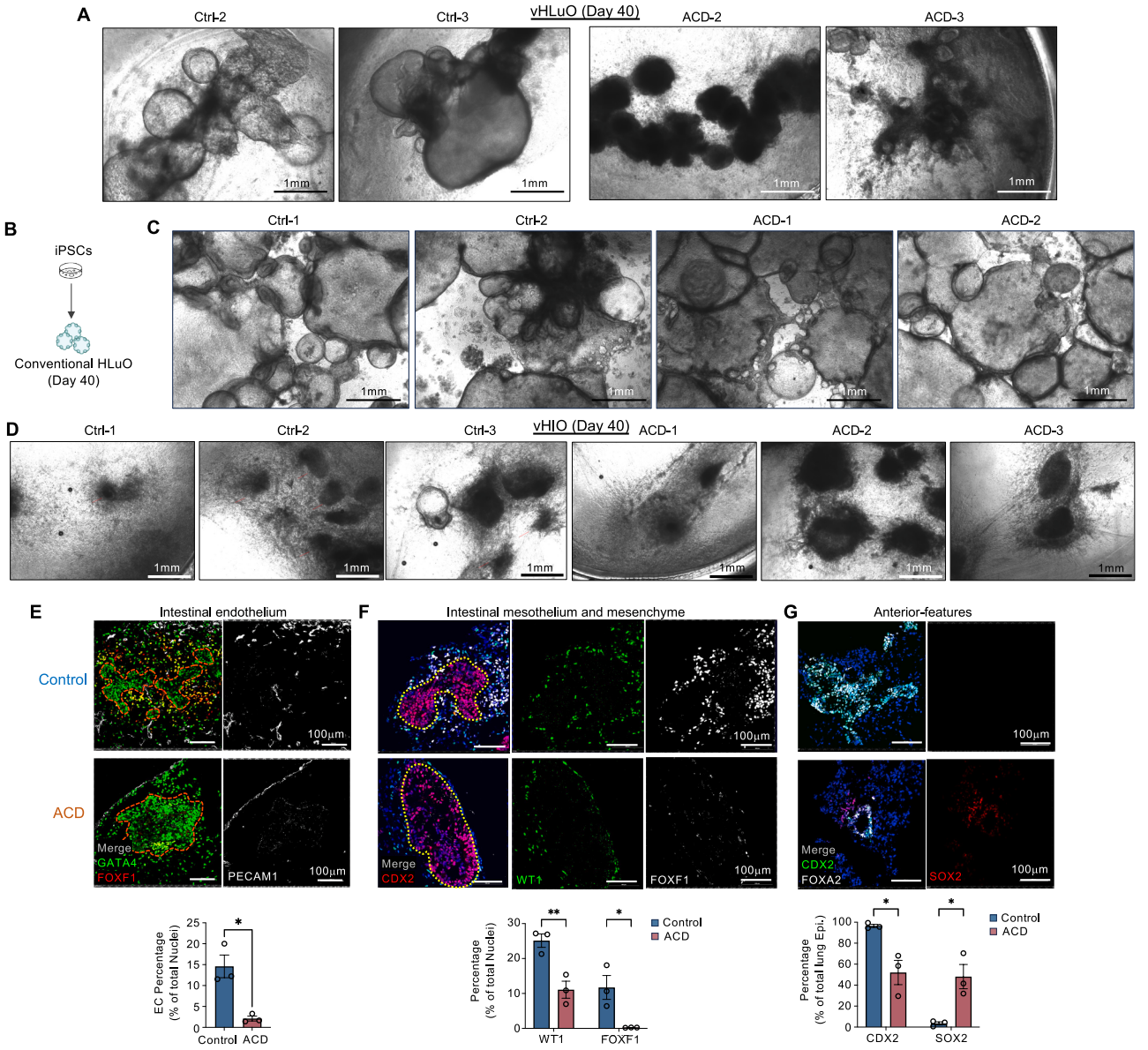

Figure S7. Morphological differences in vHLuO, vHIO, and conventional HLuO derived from control and ACD patient iPSCs, related to Figure 7

(A) Bright-field images of day 40 vHLuO organoids derived from two control and two ACD iPSC lines.

(B and C) Bright-field images of day 40 conventional HLuO organoids derived from two control and two ACD iPSC lines. The minimal mesenchymal population was growing in conventional HLuO organoids.

(D) Bright-field images of day 40 vHIO organoids derived from three control and ACD iPSC lines. Red arrowheads indicated differentiated vHIO.

(E) Immunostaining of endothelium (PECAM1^{+}) in vHIO.

(F) Immunostaining of mesothelium (WT1^{+}) and mesenchyme (FOXF1^{+}) in vHIO.

(G) Ectopic expression of anterior marker SOX2 in day 40 vHIO from ACD patient. *n* = different patient lines. t test: (E–G) Data are represented as mean ± SEM.